FACULDADE DE ENGENHARIA DA UNIVERSIDADE DO PORTO

Role of Surface Finishing and Running-in on the Coefficient of Friction of a Ball-on-Disc Contact

Martinha do Rosário Teixeira da Cunha



Master in Mechanical Engineering
Machine Design

Supervisor: Professor Carlos M. C. G. Fernandes

October 2, 2026

Role of Surface Finishing and Running-in on the Coefficient of Friction of a Ball-on-Disc Contact

Martinha do Rosário Teixeira da Cunha

Master in Mechanical Engineering
Machine Design

October 2, 2026

Abstract

Surface finishing and the running-in phase play a critical role in the tribological performance, friction behavior, and service life of mechanical power transmission components such as gears, rolling bearings, and others.

This dissertation investigates the influence of operating parameters and surface evolution on the coefficient of friction (COF) and surface morphology throughout the running-in phase. Using an EHD2 ball-on-disc tribometer under rolling-sliding contact conditions (SRR = 50%) at a constant temperature of 70 °C and normal load of 50 N, continuous and interrupted tests were performed across three distinct entrainment speeds (0.100 m/s, 0.150 m/s, and 0.300 m/s). Surface topography was extensively characterized using an optical profiler, extracting traditional amplitude parameters, such as arithmetical mean height (S_a) and root mean square height (S_q), as well as statistical summit parameters like standard deviation of summit heights (σ), mean summit radius of curvature (β), and asperity density (n).

Furthermore, experimental COF results were compared with a numerical model based on Johnson's load-sharing concept and Greenwood and Williamson's asperity contact model, incorporating a Gaussian surface topography distribution and elliptical contact mechanics. The findings demonstrate that higher entrainment speeds enhance elastohydrodynamic film formation, significantly reducing, though not entirely eliminating, plastic deformation and surface wear. At the micro-scale, a reduction in asperity heights was observed, particularly at the higher entrainment speed. Although the model exhibits limitations in capturing the evolution of summit parameters throughout the running-in phase, it still accurately predicts the coefficient of friction for the majority of the tests.

Finally, Stribeck curves and specific film thickness evaluations confirmed that the operational points predominantly operate within the mixed lubrication regime, validating the numerical model's capability to capture transient surface adaptation and friction evolution.

Keywords: Coefficient of Friction, Running-In, Stribeck Curve,Summit Parameters, Surface Roughness

Resumo

O acabamento superficial e a fase de running-in desempenham um papel crítico no desempenho tribológico, no comportamento do atrito e na vida útil de componentes de transmissão de potência mecânica, tais como engrenagens, rolamentos e outros.

Esta dissertação investiga a influência dos parâmetros operacionais e da evolução superficial no coeficiente de atrito (COF) e na morfologia da superfície ao longo da fase de running-in. Utilizando um tribómetro bola-disco EHD2 em condições de contacto de rolamento-deslizamento (SRR $= 50\%$) a uma temperatura constante de $70\,^{\circ}$C e com uma carga normal de 50 N, foram realizados ensaios contínuos e interrompidos em três velocidades de arrastamento distintas ($0,100$ m/s, $0,150$ m/s e $0,300$ m/s). A topografia das superfícies foi extensivamente caracterizada com recurso a um perfilómetro ótico, extraindo parâmetros de amplitude tradicionais, tais como a altura média aritmética (S_a) e a altura quadrática média (S_q), bem como parâmetros estatísticos das asperidades, tais como o desvio padrão das alturas das asperidades (σ), o raio médio de curvatura das asperidades (β) e a densidade de asperidades (n).

Adicionalmente, os resultados experimentais do COF foram comparados com um modelo numérico baseado no conceito de partilha de carga de Johnson e no modelo de contacto de asperidades de Greenwood e Williamson, incorporando uma distribuição Gaussiana da topografia superficial e mecânica de contacto elíptico. Os resultados demonstram que velocidades de arrastamento mais elevadas potenciam a formação de filme elastohidrodinâmico, reduzindo significativamente, embora sem as eliminar por completo, a deformação plástica e o desgaste superficial. À micro-escala, observou-se uma redução nas alturas das asperidades, particularmente à velocidade de arrastamento mais elevada. Embora o modelo apresente limitações na captura da evolução dos parâmetros das asperidades ao longo da fase de running-in, o mesmo continua a prever com precisão o coeficiente de atrito na maioria dos ensaios.

Por fim, as curvas de Stribeck e a evolução da espessura de filme específica confirmaram que os pontos de funcionamento operam predominantemente no regime de lubrificação mista, validando a capacidade do modelo numérico para capturar a adaptação superficial transitória e a evolução do atrito.

Keywords: Coeficiente de Atrito, Curva de Stribeck, Parâmetros de Asperidades, Running-In, Rugosidade Superficial

Acknowledgements

First and foremost, I would like to express my sincere gratitude to my supervisor, Professor Carlos Fernandes, for his invaluable guidance, continuous support, and expert advice throughout the development of this dissertation. His encouragement and availability were fundamental to the successful completion of this work. An additional thank you to all the members of CETRIB, especially to Luís Brito, for their help during this dissertation.

I would also like to thank the Faculty of Engineering of the University of Porto (FEUP) for providing the necessary facilities and experimental resources required for this research.

Special thanks go to my family, my mother, my father, and my sisters Tânia and Mariana, and to all my friends (they know who they are) for their unconditional support, patience, and constant motivation during this academic journey. Without them, it would not have been possible to be here today.

Also, a big thanks to my pets, Boneca, Bambi, Nana, Kiko, and Poupas, and to the pets from my petsitting, especially Bali and Lara. They were my support during continuous hours of work and moments when I didn't believe in myself, because animal love heals everything.

Finally, I am grateful to all the professors and colleagues, including the ones from my mobility in Munich, whom I encountered from my first school day to my last master's class. All these people shaped me not only as a student, but also as a person.

Martinha do Rosário Teixeira da Cunha

"Focusing on what you can't control makes you stressed.
Focusing on what you can control makes you powerful."

Mel Robbins,
The Let Them Theory

Contents

1 Introduction **1**
- 1.1 Context . . . 1
- 1.2 Goal . . . 2
- 1.3 Methodology . . . 2
- 1.4 Structure . . . 2

2 Literature Review and State of the Art **5**
- 2.1 Surface Topography . . . 5
  - 2.1.1 Surface roughness . . . 5
  - 2.1.2 Roughness parameters . . . 6
  - 2.1.3 Roughness measurement methods . . . 8
  - 2.1.4 Surface filtering method . . . 11
  - 2.1.5 Summits roughness parameters . . . 12
  - 2.1.6 Statistical distributions . . . 14
- 2.2 Running-in Phase . . . 15
- 2.3 Lubricant Regime . . . 17
- 2.4 Film Thickness . . . 19
- 2.5 Coefficient of Friction . . . 20
- 2.6 Plasticity Index . . . 21
- 2.7 Gear Surface Finishing . . . 22

3 Discussion of Experimental Results **23**
- 3.1 Experimental Setup and Ball-on-Disc Tests . . . 23
  - 3.1.1 Measurement method and setup considerations . . . 24
- 3.2 Parameters and Results . . . 25
  - 3.2.1 Continuous Reference Tests . . . 27
  - 3.2.2 Interrupted Progressive Tests . . . 32
- 3.3 Discussion . . . 37
- 3.4 Stribeck Curves . . . 45

4 Application of the Model **49**
- 4.1 Model Implementation and Summit Parameters . . . 49
- 4.2 Model Implementation and Adjustment . . . 55
- 4.3 Stribeck Curve . . . 59

5 Conclusions and Future Work **63**
- 5.1 Conclusion . . . 63
- 5.2 Further Work . . . 64

A Elliptical Contact **67**
A.1 Hertzian Contact 67

B Techniques for measuring surface topography **73**

C Summary of Tests Performed **75**
C.1 Total Sliding Distance 75
C.2 Number of Cycles 75

D 3D Surface Topography and Roughness Profiles **77**
D.1 Surface Topography at $V_e = 0.100$ m/s 78
D.2 Surface Topography at $V_e = 0.150$ m/s 79
D.3 Surface Topography at $V_e = 0.300$ m/s 80

Bibliografia **81**

List of Figures

2.1 Arithmetic average height. . . . 6
2.2 Ten-point height parameter definition in both systems. . . . 7
2.3 Example of a stylus profilometer instrument. . . . 8
2.4 Schematic diagram of a VSI system. . . . 9
2.5 Confocal microscopy principle. . . . 10
2.6 Confocal chromatic principle. . . . 10
2.7 Structured light projection measurement. . . . 11
2.8 Optical profiler. . . . 12
2.9 Schematic representation of a rough surface showing surface profiles and individual summit heights. . . . 13
2.10 Surface heights distribution before and after running-in, and comparison to Gaussian distribution. . . . 15
2.11 Asperity summits heights distribution before and after running-in, and comparison to Gaussian distribution. . . . 15
2.12 Schematic representation of wear and wear rate behavior. . . . 16
2.13 Schematic representation of a surface asperity: (a) before contact, and (b) after plastic deformation. . . . 16
2.14 Stribeck curve example - typical classification of different lubrication regimes. . . . 18
2.15 Lubricant regimes aspects. . . . 19
2.16 Schematic traction curve in boundary lubrication. . . . 19

3.1 The EHD2 ball-on-disc tribometer (PCS Instruments). . . . 23
3.2 Track with 3 supports for the EHD2 ball-on-disc tribometer. . . . 24
3.3 Lubricant level. . . . 25
3.4 Comparison between raw data and SMA filter for the evolution of the COF over time (continuous test at $V_e = 0.100$ m/s). . . . 28
3.5 Evaluation of COF over time for the three different velocities - continuous tests. . . . 28
3.6 Topography of each ball surface after 60 minutes in the continuous tests. . . . 30
3.7 Detail of surface topography of the ball after 60 minutes at the lowest velocity ($v = 0.100$ m/s) - continuous test. . . . 30
3.8 Detail of surface topography of the ball after 60 minutes at the medium velocity ($v = 0.150$ m/s) - continuous test. . . . 30
3.9 Detail of surface topography of the ball after 60 minutes at the highest velocity ($v = 0.300$ m/s) - continuous test. . . . 31
3.10 Surface roughness profile along the wear track after continuous test at a sliding speed of 0.100 m/s. . . . 31
3.11 Surface roughness profile along the wear track after continuous test at a sliding speed of 0.150 m/s. . . . 32

3.12 Surface roughness profile along the wear track after continuous test at a sliding speed of 0.300 m/s. . . . 32
3.13 Evolution of the coefficient of friction indicating the selected test interruption and evaluation times. . . . 33
3.14 Evaluation of COF over time for all tests - interrupted tests. . . . 34
3.15 Topography of each ball surface after 60 minutes in the interrupted tests. . . . 35
3.16 Balls surface at naked eye. . . . 35
3.17 Detail of surface topography of the ball after 60 minutes at the lowest velocity ($v = 0.100$ m/s) - interrupted test. . . . 36
3.18 Detail of surface topography of the ball after 60 minutes at the medium velocity ($v = 0.150$ m/s) - interrupted test. . . . 36
3.19 Detail of surface topography of the ball after 60 minutes at the highest velocity ($v = 0.300$ m/s) - interrupted test. . . . 36
3.20 Surface roughness profile along the wear track after interrupted test at a sliding speed of 0.100 m/s. . . . 37
3.21 Surface roughness profile along the wear track after interrupted test at a sliding speed of 0.150 m/s. . . . 37
3.22 Surface roughness profile along the wear track after interrupted test at a sliding speed of 0.300 m/s. . . . 38
3.23 Evaluation of COF over time for both $V_e = 0.100$ m/s tests. . . . 38
3.24 Evaluation of COF over time for both $V_e = 0.150$ m/s tests. . . . 39
3.25 Evaluation of COF over time for both $V_e = 0.300$ m/s tests. . . . 39
3.26 Evolution of lubricant temperature along the continuous tests. . . . 40
3.27 Evolution of lubricant temperature along the interrupted tests. . . . 41
3.28 Evolution of S_a of the balls as a function of time. . . . 41
3.29 Evolution of S_q of the balls as a function of time. . . . 41
3.30 Evolution of S_{pk} of the balls as a function of time. . . . 42
3.31 Evolution of S_{vk} of the balls as a function of time. . . . 42
3.32 Evolution of the arithmetic mean surface roughness of the ball and the coefficient of friction as a function of time at a velocity of 0.100 m/s. . . . 42
3.33 Evolution of the arithmetic mean surface roughness of the ball and the coefficient of friction as a function of time at a velocity of 0.150 m/s. . . . 43
3.34 Evolution of the arithmetic mean surface roughness of the ball and the coefficient of friction as a function of time at a velocity of 0.300 m/s. . . . 43
3.35 Comparison of Stribeck curves obtained as a function of entrainment speed for the three interrupted tests. . . . 46

4.1 Profile showing the summit selection with matrix size of 3x3 - $V_e = 0.300$ m/s interrupted test at t = 60 min. . . . 50
4.2 Profile showing the summit selection with matrix size of 5x5 - $V_e = 0.300$ m/s interrupted test at t = 60 min. . . . 50
4.3 Profile showing the summit selection with matrix size of 7x7 - $V_e = 0.300$ m/s interrupted test at t = 60 min. . . . 51
4.4 Profile showing the summit selection with matrix size of 3x3 - $V_e = 0.100$ m/s interrupted test at t = 60 min. . . . 51
4.5 Profile showing the summit selection with matrix size of 7x7 - $V_e = 0.100$ m/s interrupted test at t = 60 min. . . . 52

4.6 Evolution of roughness and asperity parameters as a function of time for the three sliding speeds during interrupted tests: (a) RMS roughness (σ), (b) asperity radius (β), and (c) asperity density (n). 54
4.7 Evolution of the roughness standard deviation to asperity curvature ratio (σ/β) of the balls over time for the three test velocities. 55
4.8 Evaluation of COF over time comparing theoretical and experimental results for the continuous test at $V_e = 0.100$ m/s. 56
4.9 Evaluation of COF over time comparing theoretical and experimental results for the continuous test at $V_e = 0.150$ m/s. 56
4.10 Evaluation of COF over time comparing theoretical and experimental results for the continuous test at $V_e = 0.300$ m/s. 57
4.11 Evaluation of COF over time comparing theoretical and experimental results for the interrupted test at $V_e = 0.100$ m/s. 57
4.12 Evaluation of COF over time comparing theoretical and experimental results for the interrupted test at $V_e = 0.150$ m/s. 58
4.13 Evaluation of COF over time comparing theoretical and experimental results for the interrupted test at $V_e = 0.300$ m/s. 58
4.14 Comparison of Stribeck curves - $V_e = 0.100$ m/s. 59
4.15 Comparison of Stribeck curves - $V_e = 0.150$ m/s. 60
4.16 Comparison of Stribeck curves - $V_e = 0.300$ m/s. 60
4.17 Evaluation of specific film thickness over time for all velocities. 61
4.18 Coefficient of Friction versus specific film thickness for all velocities. 62

D.1 3D surface topography and roughness profile obtained via optical profilometry for 0.100 m/s. 78
D.2 3D surface topography and roughness profile obtained via optical profilometry for 0.150 m/s. 79
D.3 3D surface topography and roughness profile obtained via optical profilometry for 0.300 m/s. 80

List of Tables

2.1 Cut-off length values from DIN 4768. 12

3.1 Ball and disc properties for the EHD2 test machine. 25
3.2 Steel properties. 25
3.3 Lubricant parameters. 26
3.4 Experimental test parameters. 27
3.5 Ball surface roughness evolution (S_a and S_q) for different velocities. 29
3.6 Ball functional parameters evolution (S_{pk} and S_{vk}) for different velocities. 29
3.7 Ball surface roughness evolution (S_a and S_q) over time for different velocities. . . 33
3.8 Ball functional parameters evolution (S_{pk} and S_{vk}) over time for different velocities. 34
3.9 Evolution of the calculated wear track width and respective area for the three sliding speeds during interrupted tests. 45
3.10 Experimental Stribeck curves test parameters. 45
3.11 Relative differences of the coefficient of friction for 0.100 m/s and 0.150 m/s relative to the 0.300 m/s reference curve. 47

4.1 Roughness and summit parameters for each continuous test (1-Ball and 2-Disc). . 51
4.2 Roughness and summit parameters for each time (1-Ball and 2-Disc) - $V_e = 0.100$ m/s. 52
4.3 Roughness and summit parameters for each time (1-Ball and 2-Disc) - $V_e = 0.150$ m/s. 52
4.4 Roughness and summit parameters for each time (1-Ball and 2-Disc) - $V_e = 0.300$ m/s. 53
4.5 Evolution of the σ/β ratio of the balls over time for different test velocities. . . . 53
4.6 Relative differences of the specific film thickness for 0.100 m/s and 0.150 m/s relative to the 0.300 m/s reference curve. 61

B.1 Bandwidth limitations of various techniques for measuring surface topography. . 73

C.1 Summary of tests performed in the laboratory including roughness measurements. 76

Abbreviations

COF	Coefficient of Friction
DIN	Deutsches Institut für Normung
EHL	Elastohydrodynamic Lubrication
ISO	International Organization for Standardization
PAO	Polyalphaolefin
PDF	Probability Density Function
RMS	Root Mean Square
SMA	Simple Moving Average
SRR	Slide-To-Roll Ratio
VSI	Vertical Scanning Interferometry
WLI	White Light Interferometry

Nomenclature

A	Real contact area	m^2
A_H	Hydrodynamic contact area	m^2
A_c	Nominal contact area	m^2
A_r	Wear model parameter	–
$A_{surface}$	Area of the measured surface	m^2
B	Contact width	m
B_i	Transient thermal resistance of body i	$K \cdot W^{-1}$
C_α	Dimensionless coefficient for semi-axis a	–
C_β	Dimensionless coefficient for semi-axis b	–
D	Deborah's number	–
D_{ODF}	Sum of the square distance of all points in the ODF algorithm	m^2
E	Young's modulus	Pa
E'	Equivalent elastic modulus	Pa
$E(m)$	Complete elliptic integral of the second kind	–
F_N	Normal load	N
F_f	Total friction force	N
$F_{f,H}$	Hydrodynamic friction force component	N
$F_{f,C}$	Asperity contact friction force component	N
G	Dimensionless material parameter	–
H	Indentation hardness / Dimensionless film thickness	Pa / –
H_c	Central film thickness (Moes dimensionless)	–
H_{00}, s	Moes auxiliary film thickness constants	–
$H_{RI}, H_{EI}, H_{RP}, H_{EP}$	Moes asymptotic film thickness components	–
L	Dimensionless load parameter / Thermal load parameter	–
M	Dimensionless speed parameter	–
N	Number of asperities	–
n	Asperity density	m^{-2}
R	Equivalent radius of curvature	m
R_x, R_y	Effective curvature radii in x and y directions	m
R_{cf}	Film thermal constriction resistance	$K \cdot W^{-1}$

R_{fi}	Transient thermal resistance of body i	$\mathrm{K}\cdot\mathrm{W}^{-1}$
R_a	Arithmetic average roughness profile parameter	μm
R_q	Root mean square roughness profile parameter	μm
R_z	Ten-point height roughness parameter	μm
$\dot{Q}$	Rate of frictional heat generation	W
S_a	Areal arithmetic mean height	μm
S_q	Areal root mean square height	μm
S_{pk}	Reduced peak height	μm
S_{vk}	Reduced valley depth	μm
SRR	Slide-to-Roll Ratio	–
T_0	Inlet/Initial oil temperature	°C
$\Delta\bar{T}_{Fl}$	Frictional flash temperature rise	K
$\Delta\bar{T}_{oil}$	Lubricant temperature increase	K
$\Delta\bar{T}_f$	Final contact flash temperature	K
U	Dimensionless speed parameter	–
U_Σ	Dimensionless speed parameter (EHL)	–
U_1, U_2	Surface linear velocities of bodies 1 and 2	$\mathrm{m}\cdot\mathrm{s}^{-1}$
W	Dimensionless load parameter	–
a, b	Semi-axes of the Hertzian elliptical contact	m
h	Lubricant film thickness	m
h_c	Central film thickness	m
h_{min}	Minimum film thickness	m
$\bar{h}$	Dimensionless film thickness	–
p_h	Hertzian contact pressure	Pa
u_s	Entrainment velocity	$\mathrm{m}\cdot\mathrm{s}^{-1}$
v_{dif}	Sliding velocity	$\mathrm{m}\cdot\mathrm{s}^{-1}$
η	Dynamic viscosity	$\mathrm{Pa}\cdot\mathrm{s}$
α	Pressure-viscosity coefficient of the lubricant	Pa^{-1}
β	Asperity summit radius of curvature	μm
β_1, β_2	Asperity summit radius of curvature for bodies 1 and 2	μm
γ	Load-sharing parameter	–
γ_1	Load-sharing parameter in Moes formulation	–
ε	Thermal partition factor	–
θ	Ellipticity parameter (R_x/R_y)	–
Λ	Specific film thickness (λ ratio)	–
λ	Radius ratio (R_x/R_y) in Hertzian contact	–
μ	Coefficient of friction	–
μ_c	Asperity contact coefficient of friction	–
$\mu_{c,\max}$	Maximum asperity contact coefficient of friction	–
ν_1, ν_2	Poisson's ratios of bodies 1 and 2	–
σ_1, σ_2	Standard deviation of summit heights for bodies 1 and 2	μm

σ_s	Standard deviation of combined summit heights	μm
ϕ_T	Thermal reduction factor	–
χ_i	Thermal diffusivity of body i	$\mathrm{m}^2 \cdot \mathrm{s}^{-1}$
S_{ep}	Plastic-elastic transition parameter for boundary friction	–
Ψ	Plasticity index	–
κ	Ellipticity parameter	–
m	Auxiliary modulus for elliptic integrals	–
τ	Shear stress	Pa
$\bar{\tau}$	Mean shear stress in lubricant film	Pa

Chapter 1

Introduction

1.1 Context

For decades, tribological systems and mechanical components subjected to relative motion have played a critical role in engineering applications [1]. Throughout the operation of these systems, sliding and rolling contacts are invariably accompanied by friction, wear, and energy dissipation [2]. Consequently, understanding the surface degradation is a primary objective in engineering design to ensure structural reliability and efficiency [3].

Finishing processes, or ultra-precision machining, are manufacturing technologies to improve the surface quality of components and enhance surface integrity. They effectively reduce initial surface roughness, optimize lubricant performance, and minimize the risk of scuffing failure [4]. Because every finishing process yields distinct topographical characteristics that dictate long-term operational performance [5], designing these interfaces effectively requires a thorough understanding of how surface topography influences friction and wear [2]. Furthermore, advancements in manufacturing technologies over recent decades have enabled a wide variety of surface topographies, directly impacting friction levels under dry and lubricated regimes, lubricant film formation, and load-carrying capacity [3].

However, traditional surface roughness parameters are often insufficient to fully describe functional contact surfaces [2,3]. Addressing current energy and environmental demands also requires a comprehensive analysis across a product's entire lifecycle, from manufacturing to operation and maintenance [6].

In the manufacturing industry, gear transmissions are widely used in various mechanical applications, offering advantages such as compact structure, constant transmission ratio, high transmission efficiency, and long service life [7, 8]. Nevertheless, gear finishing remains challenging because gears feature complex curved surfaces where profile accuracy must be preserved, and conventional finishing methods often struggle to meet large-scale industrial production requirements [4].

1.2 Goal

The primary objective of the present dissertation is to experimentally investigate the influence of surface finishing and operating parameters on the coefficient of friction and its transient evolution throughout the running-in phase, using an EHD2 ball-on-disc tribometer.

Accordingly, the following specific objectives are established:

- Evaluate and compare continuous and interrupted tests to monitor surface morphology changes and friction behavior under sliding-rolling contact conditions;
- Analyze the influence of entrainment speed on the duration of the running-in period, steady-state friction, and asperity flattening;
- Extract and apply statistical summit parameters (σ, β, n) from optical profilometry measurements to characterize micro-geometry evolution;
- Compare experimental friction results with numerical predictions derived from a Python-based contact model to validate its capability to capture transient surface adaptation;
- Construct and analyze Stribeck curves to identify and map the prevailing lubrication regimes.

The results of the present work may help to better understand the influence of operational parameters and surface evolution during the running-in phase on the final surface characteristics and tribological performance.

1.3 Methodology

The simulations and experimental evaluations presented in this dissertation were developed using an EHD2 ball-on-disc tribometer, encompassing both continuous and interrupted tests under controlled sliding-rolling conditions. To characterize the surface topography and measure the surface roughness of the bodies, an optical profiler was employed, performing multiple measurements across various locations on the balls and disc to ensure representative data acquisition, such as statistical summit parameters. The experimental results were subsequently compared with an existing computational model based on EHL theory and asperity contact mechanics, which was modified and implemented using Python. The development and structuring of the Python code were supported by AI-based collaboration tools, such as Gemini and ChatGPT.

1.4 Structure

The dissertation follows the structure outlined below, comprising three main chapters in addition to the introduction. Each chapter is important to reach the goals of this dissertation.

Chapter 2 provides a comprehensive literature review and state of the art overview regarding surface topography, roughness parameters, and measurement techniques (such as stylus profilometry and optical methods). Furthermore, it addresses the fundamental mechanisms of the running-in phase, lubrication regimes, Stribeck curve, film thickness formulations, plasticity index and gear surface finishing processes. This chapter was developed through an extensive review conducted via academic databases, including Google Scholar, Scopus, and Elsevier.

Chapter 3 presents and discusses all the results obtained from the ball-on-disc tests and optical profiler measurements. It details the influence of entrainment speed, surface roughness evolution, the comparison between continuous and interrupted tests, and the experimental Stribeck curves.

Chapter 4 presents and discusses all the results obtained from the numerical simulations. It details the summit parameters, and Stribeck curves. Additionally, the experimental findings are critically analyzed and compared with the numerical results derived from the model.

Chapter 5 draws the main conclusions of the dissertation, summarizing the key findings regarding the impact of surface finishing and running-in on the coefficient of friction, and discusses potential next steps and recommendations for future work.

Chapter 2

Literature Review and State of the Art

This chapter provides a comprehensive literature review and state-of-the-art overview regarding surface topography, roughness parameters, and advanced measurement techniques. Furthermore, it addresses the fundamental mechanisms governing the running-in phase, lubrication regimes, Stribeck curves, film thickness equations, and gear surface finishing processes.

2.1 Surface Topography

In surface metrology, topography refers to the structural features of a surface defined over a continuous range of spatial wavelengths. These characteristics are hierarchically decomposed into the primary form, representing the nominal geometry, and the superimposed texture components of waviness and roughness [9]. Many standards exist to describe measurement techniques and desired characteristics, such as ASME B46, ISO 4287, ISO 25178 and SEMI MF1811 [10].

A significant limitation in current literature is the assumption of a fixed initial surface topography, which overlooks the transient morphological changes that develop under operational loading [11]. Surface topography, as defined by the specific finishing process employed, serves as a critical determinant of initial contact conditions and exerts a significant influence on the overall performance of the system [5].

The lubrication performance at the friction interface is affected by surface topography. This happens because the surface topography influences the local contact of surface asperities and the flow of the surrounding fluid [4].

2.1.1 Surface roughness

There is a difference between roughness and waviness: the roughness refers to fine-scale surface texture features (short-wavelength), while waviness pertains to larger-scale deviations (long-wavelength) [9].

The surface roughness height is normally the same or higher than average film thickness of the contact. Thus, when the film thickness reaches a limit value, direct rough contact occurs due to the presence of surface topography. To understand friction and running-in phenomena, a surface

evolution in time is one method of analysis. Most of the studies are conducted in dry contacts, and there are not many studies in lubricated contacts, especially in mixed lubrication conditions [12].

As surface roughness increases, there is a decrease in the real contact area, indicating that fewer asperities are involved in the contact and they undergo deformation. In a dry sliding ball-on-disc configuration [13], it was observed that for surfaces with higher initial roughness (such as the turning sample), the initial value of the friction coefficient is smaller compared to ground and milled samples. This occurs because an increase in roughness reduces the actual contact area, engaging fewer asperities. Furthermore, it was verified that as the surface becomes smoother, the surface roughness decreases [13]. From the study of Akbarzadeh and Khonsari [14], it was concluded that smoother surfaces reach steady state earlier in comparison with rougher surfaces. Additionally, the drop in arithmetic average of asperity heights is smaller in the smoother surfaces. They stated also that as the surfaces undergo running-in, the asperity heights decrease, meaning the contribution of hydrodynamic film higher and a smaller film thickness is required to completely separate the surfaces.

2.1.2 Roughness parameters

Amplitude parameters are used to measure the vertical characteristics of the surface deviations [15]. The following Subsections (2.1.2.1-2.1.2.3) give a brief description of each parameter used to characterise surface topography.

2.1.2.1 Arithmetic average height

The arithmetic average height parameter, R_a, is defined as the average absolute deviation of the roughness irregularities from the mean line over a single sampling length, calculated as shows Equation (2.1) [15].

$$R_a = \frac{1}{l}\int_0^l |z(x)|\,dx \tag{2.1}$$

where l is the profile length and $z(x)$ is the profile height at the position x.

This parameter can also be known as centre line average (CLA), being easy to measure and define. It gives a strong description of height variations, although does not differentiate between peaks and valleys [16]. Thus, it is not sensitive to small changes in profile (Figure 2.1).

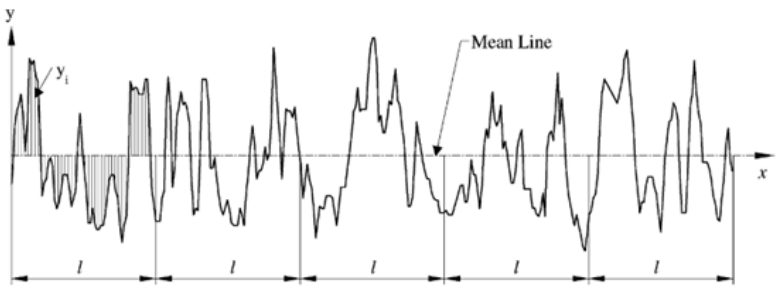


Figure 2.1: Arithmetic average height.

2.1.2.2 Root mean square roughness

The root mean square (RMS) roughness parameter, R_q, represents the standard deviation of the surface height distribution [15]. In comparison to R_a, it is more sensitive to large deviations from the mean line, making it particularly relevant for statistical analysis. It is applied in contact mechanics and lubrication, although it is less widespread due to the reliance on parameters that measure extreme values [16]. Equation (2.2) describes the mathematical definition of this parameter.

$$R_q = \sqrt{\frac{1}{l}\int_0^l z^2(x)dx} \tag{2.2}$$

2.1.2.3 Ten-point height

The ten-point height parameter, R_z, often referred to as the maximum peak-to-valley height, is more sensitive to high peaks or deep valleys than R_a. This parameter is defined by two methods, according to the definition system. The International ISO system defines as the average height difference between the five highest peaks and the five lowest valleys within the assessment length of the profile, Equation (2.3). On the other hand, the German DIN standard defines this parameter as the average of the summation of the five highest peaks and the five lowest valleys along the assessment length of the profile, Equation (2.4). Figure 2.2 shows the definitions described [15].

$$R_{z(\mathrm{ISO})} = \frac{1}{n}\left(\sum_{i=1}^{n} p_i + \sum_{i=1}^{n} v_i\right) \tag{2.3}$$

$$R_{z(\mathrm{DIN})} = \frac{1}{2n}\left(\sum_{i=1}^{n} p_i + \sum_{i=1}^{n} v_i\right) \tag{2.4}$$

where n is the number of samples along the assessment length.

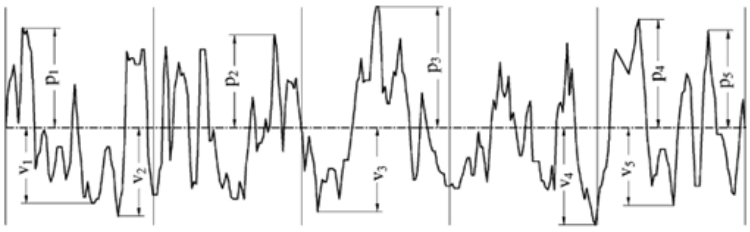


Figure 2.2: Ten-point height parameter definition in both systems.

Other parameters, such as the maximum height of peaks and valleys (R_p and R_v), the mean height of peaks and valleys (R_{pm} and R_{vm}), and the maximum height of the profile (R_t or R_{max}), are more suitable for specific scenarios. Detailed definitions of these parameters can be found in [15].

2.1.3 Roughness measurement methods

Surface topography measurement techniques are primarily categorized by their measuring principle, generally employing either physical scanning probes, such as stylus profilometry and atomic force microscopy (AFM), or electromagnetic radiation, including optical profilometry and angle-resolved scattering [10]. Non-contact optical instruments offer distinct advantages over stylus-based systems, most notably the ability to perform measurements rapidly without risking surface damage. However, data interpretation requires careful consideration for both techniques, as they are each susceptible to unique measurement artifacts and modeling assumptions. Whereas a stylus instrument can be relatively simply modeled as a ball of finite radius moving across the surface, modeling the interaction of an electromagnetic field in optical systems is highly complex. Consequently, optical measurements often require an a priori understanding of the surface characteristics before measurement is attempted [17].

2.1.3.1 Stylus profilometry

Stylus profilometry is an extremely robust and versatile contact technique that uses a stylus to measure the surface [10, 18]. There is a series of international standards [19] that standardize information about this technique. Basically, a static measuring force is applied to the probe, which is in contact with the surface, causing elastic and plastic deformation in softer materials and tip wear that influences the results. Depending on the tip radius and the shape, the results are influenced. A smaller tip allows for a better description of the surface, giving better precision of the profile. Normally, a cone with a spherical tip is used [18]. Figure 2.3 shows an example of the measurement loop of a stylus instrument [18].

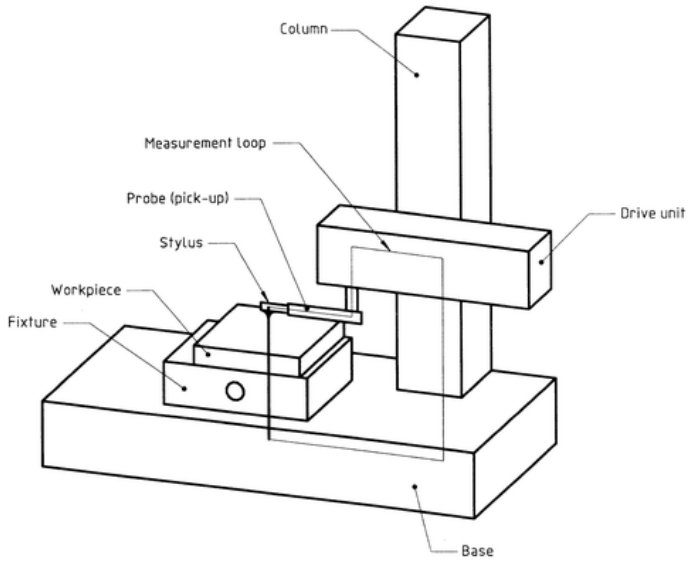


Figure 2.3: Example of a stylus profilometer instrument.

2.1.3.2 White light interferometry

White light interferometry (WLI), which is also known as vertical scanning interferometry (VSI) or coherence scanning interferometry [20], is a fast nanoscale surface measurement method possible to be used to measure micro-nano surfaces in the full frequency band. It has the advantages of surface measurement, nanometer axial resolution for smooth optical surface, significant data collection, and good measurement traceability [21]. Can measure the surface of a sample in only one measurement, since it is capable of measuring a large area. In this instrument, the light beam from the light source is split into two: one to the reference surface and the other to the measurement surface, then these light beams are reflected and interfere with each other [22]. Figure 2.4 presents a schematic diagram of a representative VSI system.

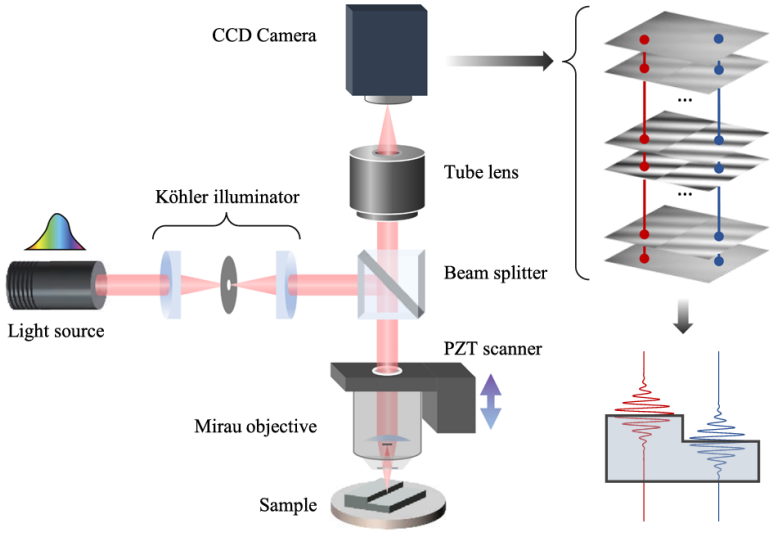


Figure 2.4: Schematic diagram of a VSI system.

2.1.3.3 Confocal microscopy

According to ISO 25178-6, confocal microscopy is an optical measurement method of surface topography in which light reflected from the sample surface is filtered by a pinhole that discriminates what is in the focal plane from what is not [23]. The technique maps the surface by capturing information exclusively from the focal plane, even it was originally developed to decrease image blurring and improve sharpness (even when analyzing thick specimens) [16]. It is a non-contact surface imaging technique capable of capturing precise three-dimensional topography, which is particularly advantageous for non-flat or translucent specimens [9, 24]. Consequently, a vertical scan of the sample is required to reconstruct the complete three-dimensional surface topography. The measurement principle is presented in Figure 2.5 [16].

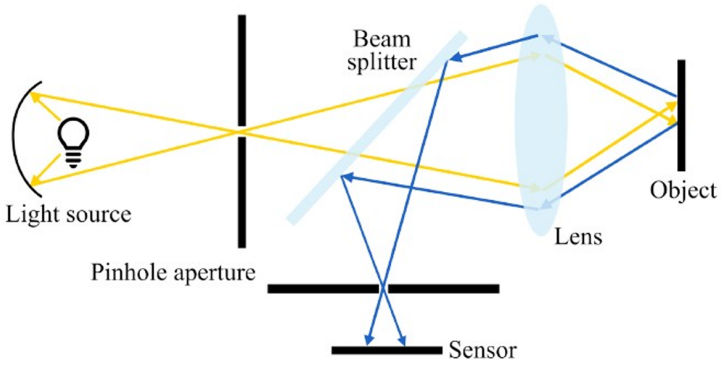


Figure 2.5: Confocal microscopy principle.

2.1.3.4 Confocal chromatic

Confocal chromatic utilizes a chromatic objective lens within the probe that decomposes the incident light into distinct wavelengths. The surface reflects the beam at a specific wavelength, which is directly related to the distance between the surface and the probe. Consequently, the profile height is a function of the returned wavelength, as illustrated in Figure 2.6 [25]. Because this method only measures the height of the focal point, the probe must be moved along the object's surface to map the entire area. Furthermore, measurements can be influenced by surface roughness due to light scattering effects [16]. While this technique is effective for various material types and offers high repeatability, further research is required to determine the optimal surface roughness range that avoids signal noise, specifically considering the impact of scanning speed. This technique provides the unique capability of generating detailed surface topographies by tracking signal intensity as the sensor scans across an object [26].

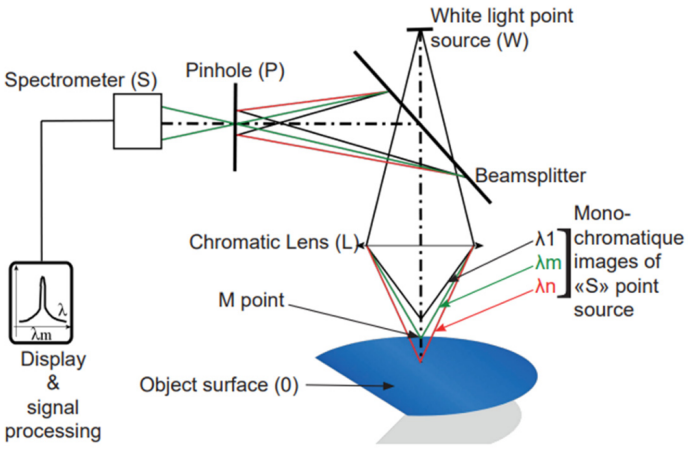


Figure 2.6: Confocal chromatic principle.

2.1.3.5 Structural light projection

Structured light projection is extensively utilized due to its broad measurement range and high resolution, accommodating objects from a few micrometers to several meters in size [27]. This technique measures the surface topography by triangulating the light beams of a light reflected by the surface (Figure 2.7). The height of the surface is calculated in function of the lateral displacement of the light beams [16].

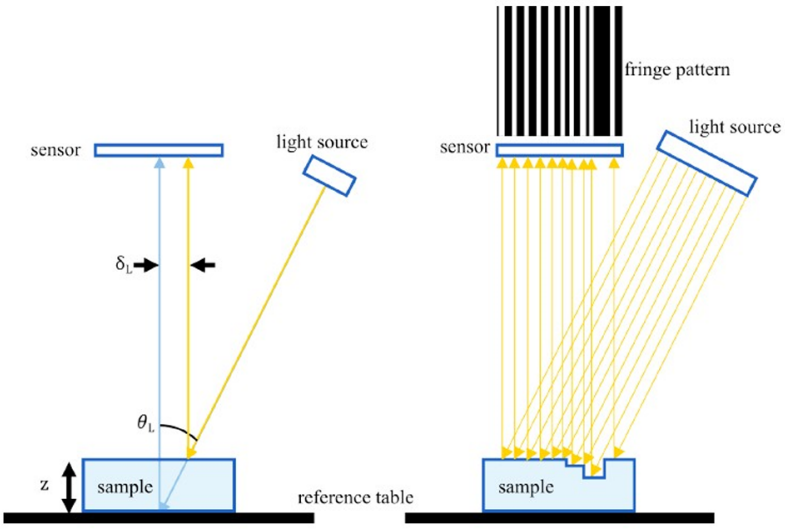


Figure 2.7: Structured light projection measurement.

The metrological capabilities and limitations of the techniques described in Sections 2.1.3.1 through 2.1.3.5 are contextualized by the comparative bandwidth analysis presented in Table B.1 in Appendix B. This Table illustrates the fundamental trade-offs between lateral resolution and the measurement field of view for both contact and optical measurement principles [10].

2.1.4 Surface filtering method

In order to remove the form and filter out the waviness of the samples, the Vision64 software can be used, filtering the waviness by applying a Gaussian filter with a normalized cut-off length (λ_c).

The optical profiler from Bruker (Figure 2.8) is capable of using multiple light sources for surface analysis [16]. However, white light interferometry was the chosen technique for evaluating the surfaces in this work.

Using the Vision64 software, the form of the measured surface was removed via a 4th-order polynomial for the disk, and a spherical fit for the ball specimens. A Gaussian filter was then applied to separate the waviness from the roughness profile. An alternative method to remove waviness is functional filtering. This approach assumes that surface features with a wavelength exceeding the contact zone length should be filtered out. Consequently, this yields a cut-off wavelength (λ_c) comparable to the Hertzian contact width. In practice, the closest standard value specified by DIN 4768 is typically selected for this parameter [16, 28]. It is recommended that λ_c be



Figure 2.8: Optical profiler.

at least 2.5 times the peak-to-peak spacing of the profile roughness. If the peak-to-peak spacing is not easily identifiable, the values of DIN 4768 from Table 2.1 can be utilized, adapted from [16].

Table 2.1: Cut-off length values from DIN 4768.

λ_c / mm	Peak spacing / mm	Measured Roughness (R_a) / μm	Roughness (R_z) / μm
0.08	< 0.032	–	–
0.25	$0.032 - 0.1$	< 0.1	< 0.5
0.8	$0.1 - 0.32$	$0.1 - 2$	$0.5 - 10$
2.5	$0.32 - 1$	$2 - 10$	$10 - 30$
8	> 1	> 10	> 30

The roughness profile is obtained by removing form and waviness. Only this profile is used to compute roughness parameters, since larger wavelength components and form deviations play no role in micro-scale contact interactions.

In conventional surface measurement methods, the roughness properties evaluated within a specific zone are assumed to be representative of the entire surface. This assumption arises from the practical difficulties of either measuring the whole surface or accurately tracking the exact contact region to evaluate its local roughness properties.

2.1.5 Summits roughness parameters

Many interfacial phenomena occur between surfaces, such as friction, wear, electrical, and thermal contact resistance. To study these phenomena, it is essential to characterize engineering surfaces, which are microscopically rough [29].

In the contact between two surfaces, only the summits of each will be in contact. A summit is defined as the highest point of a segmented surface feature, commonly referred to as an asperity

[30]. Figure 2.9 describes the differences and similarities between surfaces and summits, where the surface is depicted using a dotted line and the summits are indicated using circles. Also the distribution of surface heights and summits heights are presented in the left-hand [29].

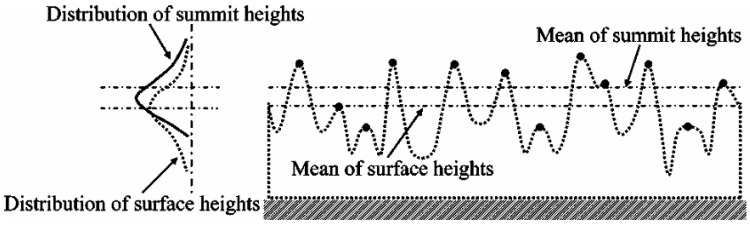


Figure 2.9: Schematic representation of a rough surface showing surface profiles and individual summit heights.

2.1.5.1 Summits Parameters

In Chapter 4, several summit parameters are employed to characterize the surface topography.

According to the ISO 25178-2:2022 standard, the arithmetic mean height, S_a, is defined as the average absolute deviation of the surface from the mean plane. It is the areal analogue of the profile parameter R_a, representing the global roughness level that influences contact mechanics and running-in processes. However, S_a is often insufficient to fully characterize the functional behavior of a surface.

In contrast, the root mean square height, S_q, which represents the standard deviation of the height distribution, is more sensitive to extreme peaks and valleys due to the squaring of deviations. This sensitivity makes S_q a more robust metric for evaluating surfaces that contain occasional severe defects or significant outliers [29–31].

In the statistical model developed in [16], the roughness parameters used are the standard deviation of the summit heights (σ_s), summit density (n), and asperity radius (β). A statistical method was employed instead of the deterministic model, as the latter - which uses the unique radius of each asperity to capture individual characteristics in a more detailed manner - is significantly more computationally demanding.

The procedure of selection of the summits and the calculation of the standard deviation of the height of those summits is described in [16]. Therefore, to account for the roughness of both surfaces, the σ_s is given by Equation (2.5).

$$\sigma_s = \sqrt{\sigma_{s1}^2 + \sigma_{s2}^2} \tag{2.5}$$

The asperity density of each surface is given by Equation (2.6).

$$n_i = \frac{N_{s,i}}{A_{surface,i}} \tag{2.6}$$

where $N_{s,i}$ is the number of summits and $A_{surface,i}$ is the measured area. Thus, for the combined surface, the asperity density is obtained by taking the average of the value obtained for each surface using Equation (2.6), as described by Equation (2.7).

$$n = \frac{n_1 + n_2}{2} \tag{2.7}$$

To obtain the radius of the summit j in both directions, the Equations 2.8 and 2.9 are used, where Δx and Δy are the measurement step in the respective directions. Then, an equivalent radius of each summit is calculated, Equation (2.10), and the asperity radius of each surface is achieved by doing the averaged of the equivalent radius of each summit. This is shown in Equation (2.11). Finally, the radius of the asperities of the combined surface is calculated by applying the Equation (2.12). If a roughness profile is utilized, the labeled y parameters are disregarded.

$$\beta_{xj}^{-1} = \frac{z(x-\Delta x, y) - 2z(x,y) + z(x+\Delta x, y)}{\Delta x^2} \tag{2.8}$$

$$\beta_{yj}^{-1} = \frac{z(x, y-\Delta y) - 2z(x,y) + z(x, y+\Delta y)}{\Delta y^2} \tag{2.9}$$

$$\beta_j = \sqrt{\beta_{xj} \cdot \beta_{yj}} \tag{2.10}$$

$$\beta_i = \frac{1}{N_s} \sum_{j=1}^{N_s} \beta_j \tag{2.11}$$

$$\frac{1}{\beta} = \frac{1}{\beta_1} + \frac{1}{\beta_2} \tag{2.12}$$

2.1.6 Statistical distributions

The surface heights distribution before and after running-in can be represented by Figure 2.10 [16]. With this distribution, it can be concluded that the higher points away from the surface are the main parts that wear out during the running-in process. Additionally, Gaussian distribution has a higher accuracy to model the surface before running-in than after.

The summits evolution can be shown in Figure 2.11 [16]. Before running-in, the surface obtained by processes like grinding and polishing can be approximated by a Gaussian distribution [32]. This is assumed by Greenwood and Williamson in [33]. However, this distribution is not the most accurate one when considering surface after the running-in process, not given the precision of the summit heights.

After the running-in, a concentration around the mean height of the summits can be seen, presenting a lower height value compared to the before of this process.

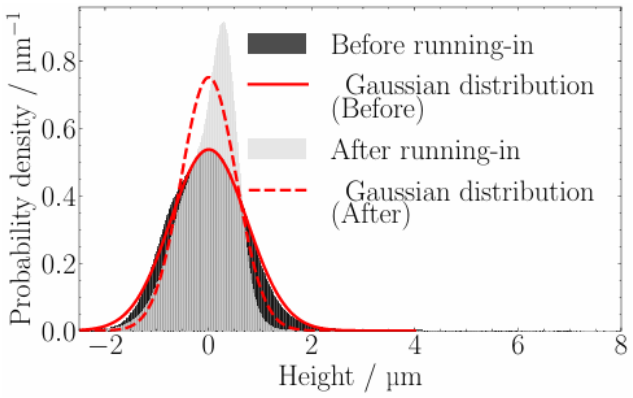


Figure 2.10: Surface heights distribution before and after running-in, and comparison to Gaussian distribution.

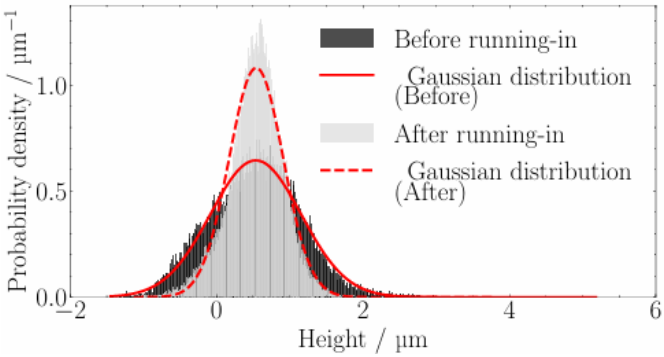


Figure 2.11: Asperity summits heights distribution before and after running-in, and comparison to Gaussian distribution.

2.2 Running-in Phase

Three different wear stages may occur during the service life of the friction components: running-in, steady-state wear and wear out. In the running-in period, or breaking-in, there are significant plastic deformation and a high wear rate, the two fresh surfaces in relative sliding motion begin to experience intimate contact at the asperities level. In the second stage, the rate of change of wear becomes constant, and then the tribo-component begins to experience wearing out, often displaying rapid, transient shifts accompanied by erratic behavior, leading to early failure shortly thereafter [34]. This is shown in Figure 2.12.

The running-in is a rapid process where the most prominent asperity tips undergo plastic deformation during the initial loading cycles [35]. The wear rate, surface roughness or friction reaches equilibrium by smoothing and deforming the asperities after this process. The running-in is characterized by the period of the Stribeck curve where the coefficient of friction decreases [13]. The micro-geometry of the surfaces conforms with each other, changing the relative position of the run-in surfaces. Thus, the hydrodynamic performance can be reduced [36].

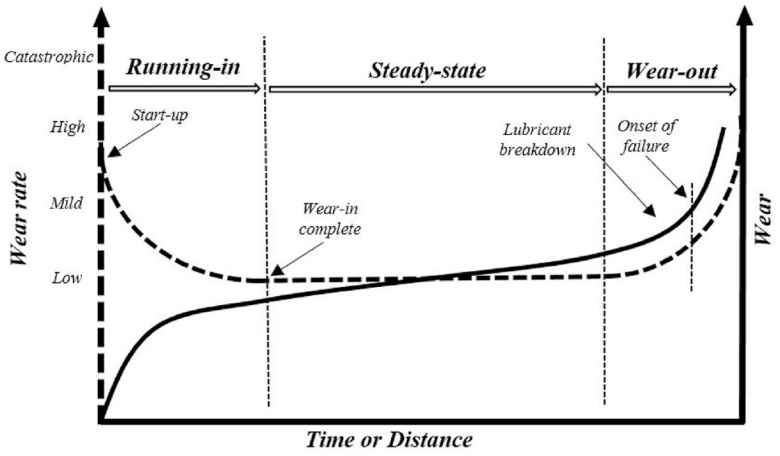


Figure 2.12: Schematic representation of wear and wear rate behavior.

The running-in phase happens when two new surfaces only contact at the highest summits, creating a smaller contact area than the apparent contact area. That can be observed in Figure 2.13, where h_c is the central film thickness, w is the displacement and y_s is the difference between the mean surface height and mean asperity height [37]. Therefore, a higher contact pressure in the asperities is obtained, and because of wear and plastic deformation, the summits are smoothed. This leads to a reduction of the roughness and an increases of the specific film thickness. This process is influenced by the surface chemistry, residual stresses and microstructure near the surface [38]. The running-in process is predominantly influenced by operating conditions such as duration, load and speed, lubricant properties, film thickness, initial surface roughness, and their orientation [5, 14].

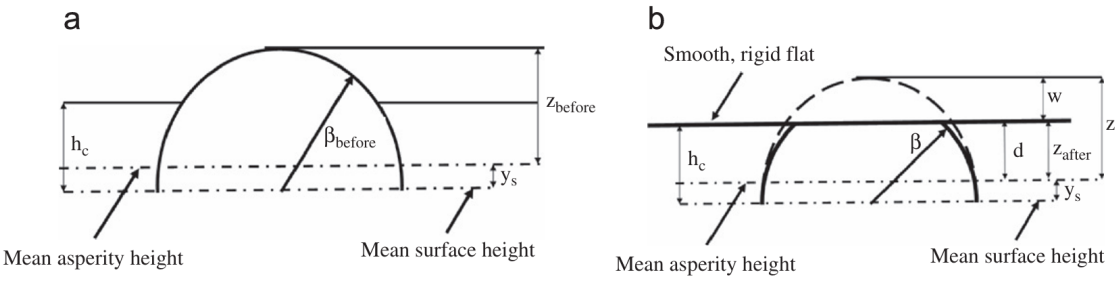


Figure 2.13: Schematic representation of a surface asperity: (a) before contact, and (b) after plastic deformation.

According to [13], the critical time marking the transition of the coefficient of friction from rising to stable is defined based on a threshold corresponding to 1.12 times the maximum value of the friction coefficient recorded throughout the experiment. In surface roughness simulations, the coefficient of friction was inversely proportional to surface roughness. It was concluded that the surface of the smoother disc samples had a shorter running-in period.

The running-in period can be seen by when the variation of the portion of load carried by the fluid film reaches a steady-state value. Akbarzadeh and Khonsari [14] measured the wear rate each

20 minutes of the experience, until a period of 100 minutes and reach-out the steady-state. It is expected that as the rolling speed increases, the duration of running-in time reduces.

Friction and wear during running-in process are influenced by the surface roughness alterations and operational parameters, such as temperature, rotation speed and applied load. The steady friction and wear can be affected by the running-in, being this stage capable of extending the service life of the friction components and ensure a stable working operation, if proper stipulated [35].

In the study of Lohner et al., they concluded that there is notable influence, even not clear, of the Hertzian pressure in the surface roughness. Additionally, the influence of the oil inlet temperature in the reduction of the roughness parameters is secondary. They also concluded that the roughness tips are more affected by the running-in than the roughness valleys [39].

About load influence, in running-in studies it was observed that surface asperities are smoothed through plastic deformation, for higher load. If the load is excessive, the existence of a plastic flattening during the final running-in stage is inevitable. In consequence, for small loads, the highest asperities are the only ones plastically deformed and polished by wear [35]. In [14], Akbarzadeh and Khonsari affirmed that the variation in surface roughness during running-in is not a function of dry wear coefficient, depending only from the operating conditions.

The running-in process further evolves surface morphology and chemistry, preconditioning the interface for service. Therefore, characterizing the variations in surface properties resulting from distinct hard finishing processes, as well as their adaptation during running-in, is essential for optimizing the efficiency and economy of gear drives [5].

2.3 Lubricant Regime

The Stribeck curve permits identification of boundary, mixed, elastohydrodynamic and hydrodynamic lubrication regimes [40]. It illustrates the friction variations over the entire lubrication range [41]. Figure 2.14 shows an example of these types of curves, demonstrating a clear relationship between friction and speed [42]. The minimum point of the curve effectively delineates the transition boundary between the mixed and full-film lubrication regimes.

The identification of the lubrication regimes permits the classification of the mechanisms of film formation in lubricated contacts. The definition of each lubrication regime is presented below:

- **Hydrostatic lubrication:** occurs when the liquid pressure is generated externally and supplied through passages between two surfaces. Even at low speeds, the friction is low, and there is precise control of the film thickness [43, 44].

- **Hydrodynamic lubrication:** occurs when the motion of the surface, the viscous properties of the liquid, and the geometry of the conjunctions together generate the load [43, 44].

- **Boundary lubrication:** occurs when molecular thin films developed from the oil or additives separates the surfaces, and the load is primarily carried by asperity interactions. The

surface chemistry plays a dominant role. In the Stribeck curve, this represents the initial regime, characterized by a relatively high and nearly constant coefficient of friction [43,44].

- **Mixed lubrication:** occurs when the lubricant film thickness is comparable to the surface roughness. The normal load is supported by a combination of hydrodynamic pressure and direct asperity contact. It is called mixed because it combines both hydrodynamic and boundary lubrication. In the Stribeck curve, is the curve where an abrupt change in the coefficient of friction happens.

- **Elastohydrodynamic lubrication:** occurs in contraformal contacts where the elastic deformation of the surfaces significantly influences the resulting lubricant film thickness. These deformation happens due to high pressure, which also causes an increase of viscosity [45]. The operating condition dictate whether the contact maintains a full-film lubrication regime or operates within the mixed lubrication range [44]. In the Stribeck curve, is the curve after the mixed lubrication curve.

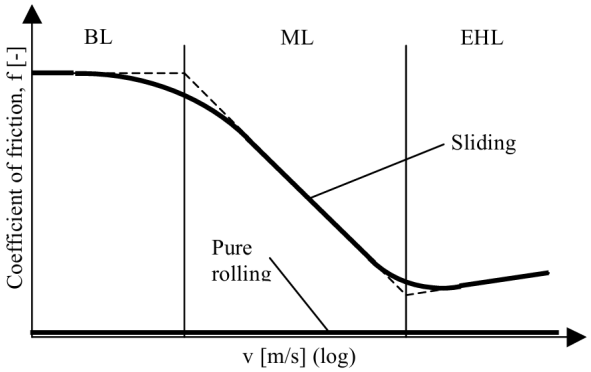


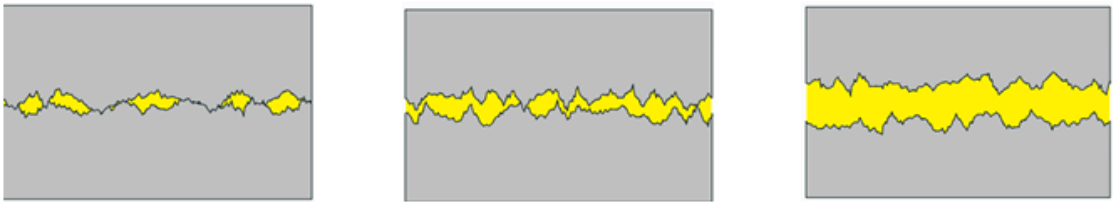
Figure 2.14: Stribeck curve example - typical classification of different lubrication regimes.

The lubricant regimes can be determined using the specific film thickness concept, Λ. It relates the relation between the film thickness, h, and the roughness of the surface, R_q, as described by Equation (2.13) [46].

$$\Lambda = \frac{h}{R_q} \tag{2.13}$$

Depending on the value of Λ, the contact operates in one of the following regimes (Figure 2.15) [16]:

- **Boundary Lubrication** ($\Lambda < 0.7$)**:** The surfaces are in direct contact at the asperities, resulting in high friction and significant wear.
- **Mixed Lubrication** ($0.7 \leq \Lambda \leq 2.0$)**:** The load is shared between the hydrodynamic pressure and asperity contact. The surfaces are partially separated.
- **Elastohydrodynamic Lubrication** ($\Lambda > 2.0$)**:** A full lubricant film is established, completely separating the surfaces and leading to significantly lower friction.



(a) Boundary lubrication regime (b) Mixed lubrication regime (c) Elastohydrodynamic regime

Figure 2.15: Lubricant regimes aspects.

.

In boundary lubrication, the lubricant film thickness is extremely thin, resulting in continuous contact between surface asperities. Consequently, this regime leads to severe wear and high friction, making it crucial to ensure that a contact does not operate under boundary lubrication conditions. Literature shows that the friction coefficient of the asperities (μ_c) varies with velocity, temperature, and environment, while also being dependent on the slide-to-roll ratio (SRR). Therefore, the asperity friction coefficient is given by Equation (2.14) [42].

$$\mu_c = \mu_{c,\max} \frac{2}{\pi} \arctan\left(\frac{\pi}{2} \frac{\mathrm{SRR}}{S_{ep}}\right) \tag{2.14}$$

where $\mu_{c,\max}$ is the maximum value of μ_c, and S_{ep} is related to the transition from the elastic to plastic behavior of the boundary layer.

This relation is represented in Figure 2.16 [42]. In standard engineering practice for steel-on-steel contacts lubricated with mineral oil, the value of μ_c typically varies within a narrow interval of 0.07 to 0.15 [47].

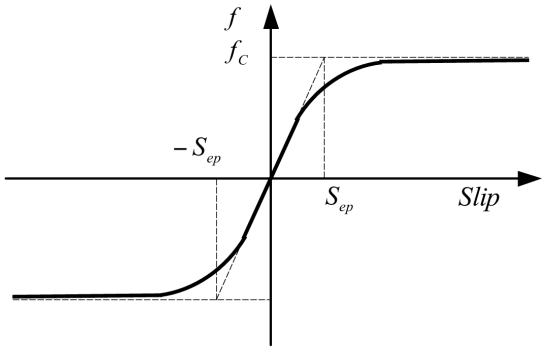


Figure 2.16: Schematic traction curve in boundary lubrication.

.

2.4 Film Thickness

The Hertzian contact pressure can be calculated according to the following Equation (2.15):

$$p_h = \sqrt{\frac{F_N E'}{2\pi b R^*}} \tag{2.15}$$

where E' is the elasticity modulus, calculated according to Equation (2.17), F_N is the normal load, b is the width and R^* is the contact radii (calculated according to Equation (2.16)) [44].

$$R^* = \left(\frac{1}{R_{x1}} + \frac{1}{R_{x2}}\right)^{-1} \tag{2.16}$$

$$E' = \left[\frac{1}{2}\left(\frac{1-\nu_1^2}{E_1} + \frac{1-\nu_2^2}{E_2}\right)\right]^{-1} \tag{2.17}$$

The specific film thickness can be expressed as the ratio between the minimum film thickness and the composite roughness, as shown by Equation (2.18) [48]:

$$\lambda = \frac{h_{min}}{\sqrt{R_{q1}^2 + R_{q2}^2}} \tag{2.18}$$

where R_{q1} and R_{q2} represent the root mean square roughness parameters of the pinion/ball and gear/disc and h_{min} is the minimum film thickness as detailed in [33].

The minimum film thickness equation used in this study is Dowson and Higginson curve fitting formula to predict EHL minimum film thickness, from 1961 [33, 39]. Equation (2.19) presents formula to calculate this parameter.

$$H_m = h_m / R_x = 1.6 G^{0.6} U^{0.7} W^{-0.13} \tag{2.19}$$

The dimensionless numbers U, W and G are the dimensionless speed parameter, the dimensionless load parameter, and the dimensionless material parameter, respectively. Equations (2.20) through (2.22) are used to calculate these parameter values [16, 33].

$$U_\Sigma = \frac{\eta_0 (U_1 + U_2)}{E' R_x} \tag{2.20}$$

$$W = \frac{F_N}{b E' R} \tag{2.21}$$

$$G = \alpha E' \tag{2.22}$$

2.5 Coefficient of Friction

In a tribological system, the coefficient of friction is governed by the lubricating oil and the rolling elements with their properties and operating conditions [49]. Consequently, it is a crucial parameter when investigating mechanical components in relative movement.

Friction force, F_f, is divided in two components, as shows Equation (2.23). Thus, is the sum of the friction force due to the shearing of lubricant, $F_{f,H}$, and the friction force due to the contact of asperities, $F_{f,C}$ [14]. These contributions are given by Equations (2.24) and (2.25), respectively.

$$F_f = F_{f,H} + F_{f,C} \tag{2.23}$$

$$F_{f,H} = \iint_{A_H} \tau_H \, \mathrm{d}A_H \tag{2.24}$$

$$F_{f,C} = \sum_{i=1}^{N} \iint_{A_{C,i}} \tau_{C,i} \, \mathrm{d}A_{C,i} \tag{2.25}$$

From Equation (2.24), the hydrodynamic contact area (A_H) and the corresponding shear stress (τ_H) are the components that influence the hydrodynamic shear force. Regarding Equation (2.25), it can be seen that the number of asperities (N), their respective area of contact ($A_{C,i}$), and the shear stress within the contact ($\tau_{C,i}$) are the ones that determine the friction force due to the contact of asperities.

By definition, the friction coefficient is the ratio between the friction force, F_f, and the normal force, F_N. Thus, the Equation (2.26) represents these relation.

$$\mu = \frac{F_f}{F_N} = \frac{\sum_{i=1}^{N} \iint_{A_{C,i}} \tau_{C,i} \, \mathrm{d}A_{C,i} + \iint_{A_H} \tau_H \, \mathrm{d}A_H}{F_N} \tag{2.26}$$

The friction coefficient will change during the running-in phase due to deformation of the asperities, and the change of the lubricant film thickness and contribution of asperities in carrying the load [14]. During the running-in phase, a reduction in the coefficient of friction is typically observed, highlighting the importance of accurately estimating this parameter [16].

2.6 Plasticity Index

The evaluation of surface contact severity between rough metallic bodies relies fundamentally on the plasticity index (Ψ), originally introduced by Greenwood and Williamson. Defined to quantify the transition between elastic and plastic deformation regimes at the asperity level, the classical formulation is expressed as:

$$\Psi = \left(\frac{E'}{H}\right)\sqrt{\frac{\sigma}{\beta}} \tag{2.27}$$

where E' is the equivalent (composite) Young's modulus, H is the indentation hardness, σ is the standard deviation of the asperity height distribution, and β is the equivalent radius of curvature of the asperities. According to classical theory, asperity contact remains predominantly elastic when Ψ is below 0.6, whereas plastic deformation dominates when Ψ exceeds 1.0 [50, 51].

Nakajima and Mawatari investigated the evolution of the plasticity index in lubricated rolling-sliding contacts, demonstrating that surface topography evolves significantly during running-in. Their findings show that higher initial or sustained Ψ values accelerate surface damage and pitting, meaning that asperity tips undergo more severe plastic deformation rather than elastic contact. This intense micro-contact creates high frictional resistance and delays the build-up of a full elastohydrodynamic oil film, as direct metal-to-metal contact persists longer during the running-in phase [50].

2.7 Gear Surface Finishing

Gear manufacturing processes include forging the gear blank, heat treatment, grinding, and others. The heat treatment can provoke some deformation on the gear, and precision grinding can reduce tooth profile errors. For this manufacturing process, the tooth surface can exhibit multiple texture patterns parallel to the tooth width direction. It has already been demonstrated that gear meshing perpendicular to the texture direction causes dynamic vibration, restricts lubrication flow, and increases transmission noise [52].

In some applications, it is important to have an additional finishing process in order to improve the surface quality of the gears. Finishing not only eliminates defects such as grinding scratches and micro-cracks, but also reduces surface unevenness. Adverse vibrations or stress concentrations during gear meshing can be reduced. Additionally, the probability of pitting failure is lower and the contact fatigue strength of gears can be improved. Finishing processes helps to break up regular wave patterns and noise paths, reducing noise and vibrations levels [52]. It prevents various problems including abrasive wear, micro-pitting, and scratching, reducing also wear, and abrasion during operation, which increases their effectiveness and lifespan [53].

Chapter 3

Discussion of Experimental Results

This chapter presents the experimental setup, procedures, and a detailed discussion of the results obtained from both continuous and interrupted ball-on-disc tests, including the evolution of surface roughness and friction over time.

3.1 Experimental Setup and Ball-on-Disc Tests

A precise control over contact conditions permits ball-on-disc tribometer to simulate gear contacts at selected positions along the gear tooth profile. It allows obtain the coefficient of friction from the resulting contact [54].

To study the influence of the surface finishing on the coefficient of friction, and based on previous studies [16], ball-on-disc tests were performed using an EHD2 machine (Figure 3.1) [55]. In these tests, the contact between the surfaces is a special case of elliptical contact. The equations for this case are presented in Appendix A.



Figure 3.1: The EHD2 ball-on-disc tribometer (PCS Instruments).

3.1.1 Measurement method and setup considerations

The EHD2 method to perform COF measurements is described in the following steps [56]:

- Clean the test ball and disc using appropriate solvents (e.g., isopropyl alcohol or acetone) to eliminate any residual contamination.
- Introduce a small volume of the test lubricant in the test area.
- Define the operating parameters:
  - First, the part of the temperature stabilization.
  - Second, establish the parameters such as the applied load, entrainment speed, slide-to-roll ratio, and the test duration.
- A tangential force friction sensor records the friction force under the specific load. The COF is then calculated by dividing traction force by the ball load, after plotting traction curves.

During the tests, several details were taken into account:

- Calibrating the track;
- Adjustment of the track position according to the track radius used for each simulation;
- Use of a track with 3 supports, as shown in Figure 3.2, ensuring that the ball was correctly placed on top of the three bearings;
- Positioning of the thermometer near the ball to ensure an accurate reading of the lubricant temperature;
- Reuse of the lubricant for each measurement (as recommended by an expert), while its condition was consistently monitored;
- Careful cleaning of the housing and all instruments used between testing days;
- Maintenance of the lubricant level up to the center of the ball during measurements (covering half of the ball), which was always carefully monitored (Figure 3.3).

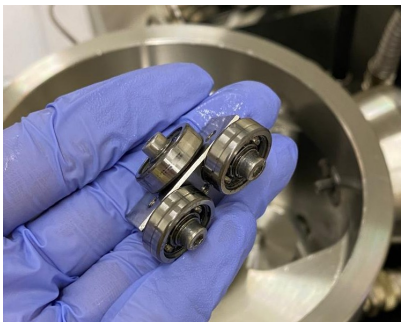


Figure 3.2: Track with 3 supports for the EHD2 ball-on-disc tribometer.

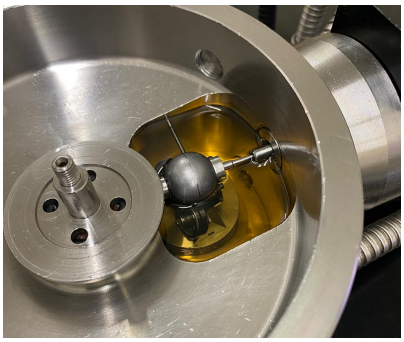


Figure 3.3: Lubricant level.

3.2 Parameters and Results

The parameters of the ball and the disc used on this study are presented in Table 3.1. An isotropic surface has all the physical properties uniform in all directions, improving the surface stress state [4]. Both bodies were made from chrome steel [55], and the properties are presented in Table 3.2. The lubricant used was the oil PAO ISO VG 150 with the properties described in Table 3.3.

Table 3.1: Ball and disc properties for the EHD2 test machine.

Property	**Ball**	**Disc**	**SI units**
R_x	9.525	∞	mm
R_y	9.525	∞	mm
E	210	210	GPa
ν	0.29	0.29	-

Table 3.2: Steel properties.

Property	**Value**
$k_{s,i}$ / (W m^{-1} K^{-1})	45
ρ_i / (kg/m^3)	7800
c_{p_i} / (J kg^{-1} K^{-1})	460

The changing parameter for each test is the entrainment speed. The entrainment speed is the average of the ball and disc linear velocity at the contacting surface [54].

To obtain the coefficient of friction versus time curves, a constant normal force of $F_N = 50$ N and a constant temperature of 70 °C were defined, as this temperature closely represents actual gear operating conditions [57] and there are previous experimental data for this temperature [16]. Regarding the entrainment speed, to determine the constant value for the study, the Stribeck curves from Miguel Dias's work [16] were analyzed, focusing on the temperatures of 70 °C. Since the objective is to study the surface evolution during the running-in phase, one must select a speed at which the lubricant film does not completely separate the ball from the disc. In other words, lower speeds are required, which correspond to a lower specific film thickness. Furthermore, the

Table 3.3: Lubricant parameters.

Parameter	**Value**	SI units
ρ	854	kg/m^3
K	0.02468	-
b	1667.31	-
c	151.09	-
s	7.382	-
t	0.1335	-
Z	0.467	-
S_0	1.09	-
k	0.18	W m^{-1} K^{-1}
c_p	2090	J kg^{-1} K^{-1}

transition between the boundary and mixed lubrication regimes is also of great interest. Therefore, a speed analysis was carried out. Based on a literature review, it was identified that similar studies typically employ entrainment speeds ranging from 0.100 m/s to 0.150 m/s, along with SRR of 20% and 50% [12,58]. Analysing the Stribeck curve obtained in Miguel Dias's work, these entrainment velocities also correspond to a beginning of the mixed lubrication regime. Upon analyzing the curves, the maximum gradient of the tangent line was observed at a velocity of approximately 0.300 m/s. Therefore, an analysis was also conducted for this specific velocity.

In the EHD2 machine, for each sliding speed, there are two scenarios: one where $U_{\text{ball}} > U_{\text{disc}}$, and the other where $U_{\text{ball}} < U_{\text{disc}}$. This difference will lead to variations associated with the thermal characteristics of the contact. Therefore, since the goal is to achieve a lower global COF and ensure its stability under sliding conditions, the disc must operate at a higher surface velocity relative to the ball ($U_{disc} > U_{ball}$). On the EHD2 machine, the previously mentioned scenario is already defined.

The slide-to-roll ratio is defined as the ratio of the sliding speed to the entrainment speed [59]. To replicate a sliding-rolling contact condition, a SRR of 50% was selected [48]. According to the Equation (3.1) [55], the governing SRR equation, this yields a disc speed of 0.125 m/s and a ball speed of 0.075 m/s for $V_e = 0.100$ m/s, a disc speed of 0.1875 m/s and a ball speed of 0.1125 m/s for $V_e = 0.150$ m/s, and a disc speed of 0.375 m/s and a ball speed of 0.225 m/s for $V_e = 0.300$ m/s. As concluded by Al-Jeboori et al. [48], a sliding-rolling contact ensures a controlled removal of asperities, which is essential for the running-in phase. Table 3.4 summarizes the constant parameters applied in this study, which were maintained across all the tests.

$$SRR = \frac{V_s}{V_e} = \frac{V_d - V_b}{\frac{V_b + V_d}{2}} \tag{3.1}$$

where V_b and V_d are the ball and disc speeds in contact, respectively.

The next Subsections will present the results for all the tests performed as registered in Table C.1 in Appendix C. The total laboratory work amounted to 46 hours and 30 minutes, including measuring the surfaces of balls and disc using the optical profiler (Figure 2.8). To have more ac-

Table 3.4: Experimental test parameters.

F_N (N)	T_0 (°C)	SRR (%)	u_s (m/s)	u_{disc} (m/s)	u_{ball} (m/s)
50	70	50	0.100	0.125	0.075
			0.150	0.1875	0.1125
			0.300	0.375	0.225

curate results, the experimental procedure should have been repeated three times. This replication could not be performed due to insufficient material availability. Care was taken to perform three measurements at each location on each ball and disc surface using the optical profiler, while ensuring that the percentage of valid data points in Vision64 was at least 80%. Furthermore, before utilizing the aforementioned software, a *Data Analyzer (F-Operator)* was first applied to remove the surface form ("sphere and tilt" for the balls, and "tilt only" for the disc). Additionally, a *Gaussian Regression Filter* with a short wavelength cutoff of 0.25 mm was applied.

3.2.1 Continuous Reference Tests

To establish the experimental timeline, an initial baseline test was performed without interruptions. The results were then analyzed to determine the precise intervals at which subsequent tests should be paused for surface characterization. The tests had a duration of 1 hour, as no significant variation was observed after this period. Accordingly, the total number of sliding cycles for each test was calculated using Equations C.1 and C.2 in Appendix C. Based on these parameters, the total number of accumulated cycles reached 1614 for the sliding velocity of 0.100 m/s, 2323 for 0.150 m/s, and 4677 for the velocity of 0.300 m/s. This can be consulted in Table C.1, at Appendix C.

Before plotting the evolution of the COF over time for all tests, the application of a simple moving average (SMA) filter using a window size of $N = 20$ was first analyzed to reduce signal noise and facilitate the analysis of the general trend [60]. Here, N represents the number of consecutive data points used to compute each average value. As shown in Figure 3.4, this approach simplifies the raw data, yielding a much clearer trend of the COF variation.

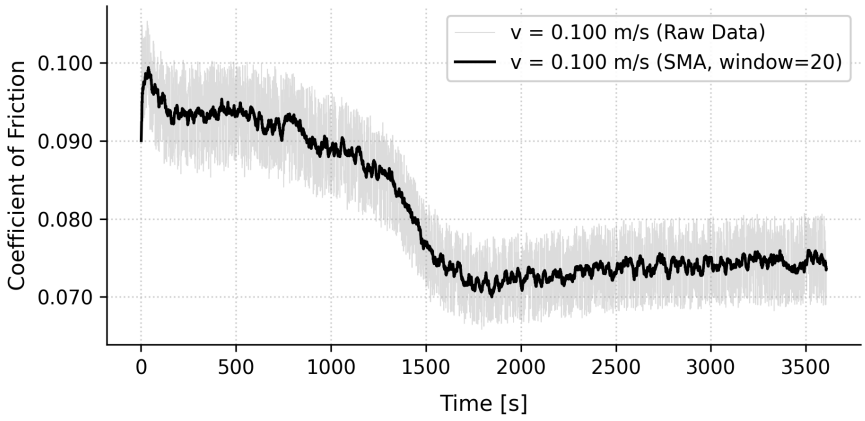


Figure 3.4: Comparison between raw data and SMA filter for the evolution of the COF over time (continuous test at $V_e = 0.100$ m/s).

Applying the same methodology, the evolution of the coefficient of friction over time was plotted to compare the different sliding speeds, Figure 3.5. The plots were generated using Python scripts, incorporating the aforementioned simple moving average filter.

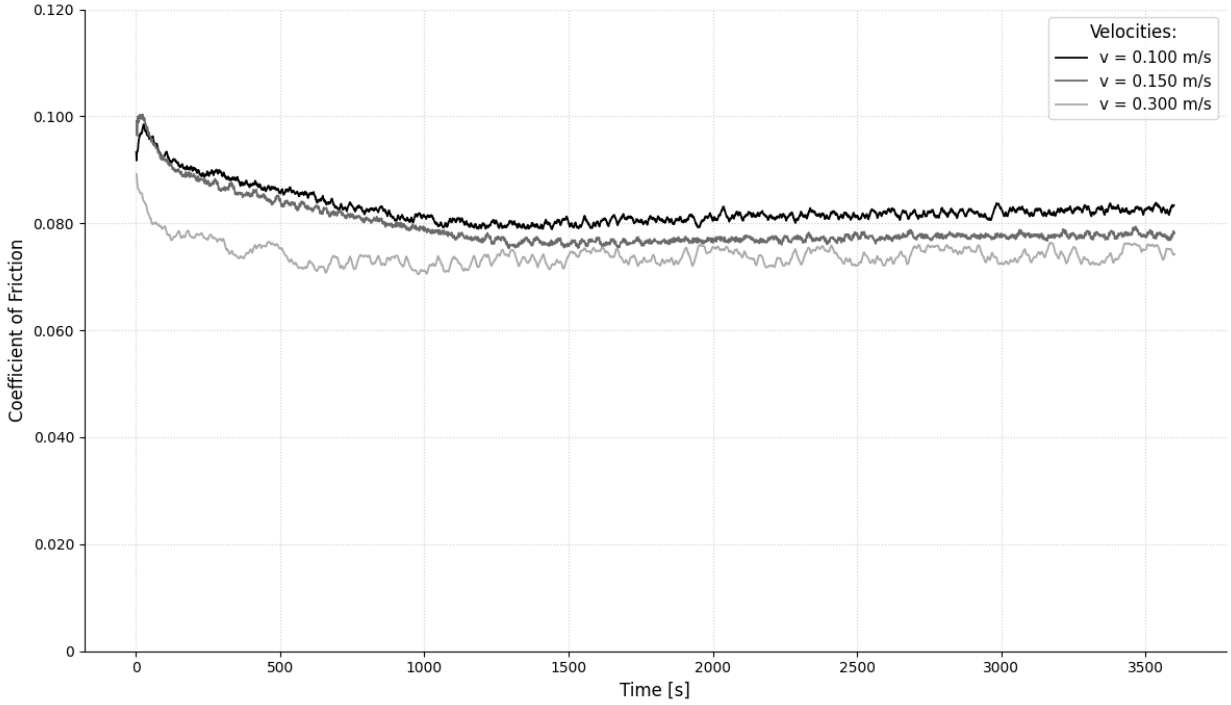


Figure 3.5: Evaluation of COF over time for the three different velocities - continuous tests.

It can be concluded that increasing the sliding speed effectively reduces the duration of running-in period, as expected. This is observed in the time required for the COF to start stabilising. For the highest velocity, the running-in phase had a duration of 600 s, for the medium velocity a duration of 1200 s, and for the lowest velocity, it was approximately the same as the medium velocity. Analyzing Figure 3.5, a decrease in the coefficient of friction is observed with increasing velocity.

This behavior is expected, as higher speeds lead to a greater film thickness, which better protects the interacting asperities and reduces asperity contact.

Tables 3.5 and 3.6 present the results of the surface roughness (S_a, S_q) and functional parameters (S_{pk}, S_{vk}) of the balls, and the percentage reductions, across the three tested velocities after the 1-hour duration.

A substantial decrease is observed in all parameters, confirming intensive asperity flattening and plastic deformation during the running-in phase. Notably, for $v = 0.150$ m/s there is the highest reduction percentages for both S_a (50.75%) and S_{pk} (51.61%), indicating aggressive mechanical interaction at the micro-scale. In contrast, the highest speed ($v = 0.300$ m/s) shows a slightly more moderate reduction in peak height parameters (e.g., 36.00% for S_{pk}), which can be attributed to an enhanced hydrodynamic film formation that partially shields the surfaces from severe direct asperity contact. Furthermore, S_{vk} parameters show much lower reductions (18% to 24%) across all speeds, demonstrating that valleys are largely preserved to maintain lubricant retention within the contact interface.

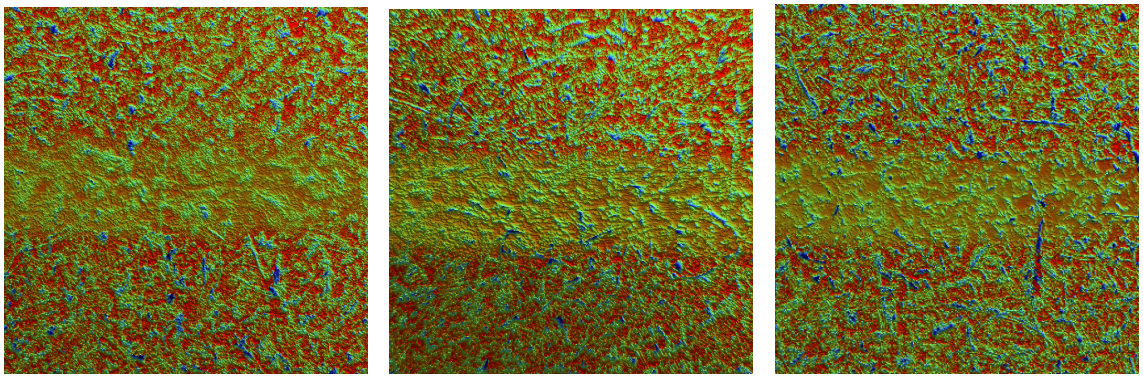
Table 3.5: Ball surface roughness evolution (S_a and S_q) for different velocities.

Velocity (m/s)	S_a **(µm)**			S_q **(µm)**		
	Initial	Final	Reduction (%)	Initial	Final	Reduction (%)
0.100	0.332	0.178	46.387	0.434	0.252	41.935
0.150	0.335	0.165	50.746	0.438	0.249	43.151
0.300	0.368	0.189	48.641	0.486	0.290	40.329

Table 3.6: Ball functional parameters evolution (S_{pk} and S_{vk}) for different velocities.

Velocity (m/s)	S_{pk} **(µm)**			S_{vk} **(µm)**		
	Initial	Final	Reduction (%)	Initial	Final	Reduction (%)
0.100	0.331	0.186	43.807	0.655	0.499	23.817
0.150	0.310	0.150	51.613	0.654	0.533	18.502
0.300	0.400	0.256	36.000	0.814	0.624	23.342

The topography of each ball surface after the 60 minutes is shown in Figure 3.6. A distinct central horizontal wear track is clearly observable, outlining the continuous mechanical interaction between the two bodies after 60 minutes of testing. At the lowest velocity (Figure 3.6 a), a more pronounced smoothing and plastic deformation of the surface asperities can be noted within the track, driven by a thinner lubricant film. For the medium velocity (Figure 3.6 b), the wear zone exhibits a more stable and balanced transition. Finally, at the highest velocity (Figure 3.6 c), the wear track appears less aggressive and less modified compared to the surrounding uncontacted area, confirming that the thicker lubricant film provided superior surface protection throughout the continuous test. Overall, these topographies corroborate that under continuous operation, increasing entrainment velocity significantly mitigates surface wear and deformation.



(a) Lowest velocity (0.100 m/s): S_a from 0.332 to 0.178 μm; S_q from 0.434 to 0.252 μm.

(b) Medium velocity (0.150 m/s): S_a from 0.335 to 0.165 μm; S_q from 0.438 to 0.249 μm.

(c) Highest velocity (0.300 m/s): S_a from 0.368 to 0.189 μm; S_q from 0.486 to 0.290 μm.

Figure 3.6: Topography of each ball surface after 60 minutes in the continuous tests.

Detailed magnifications of specific surface areas to better understand the surface condition of the balls following the continuous tests are presented in Figures 3.7 through 3.9. Further Figures are presented in Appendix D. A more pronounced plastic deformation is noticeable at the lowest velocity.

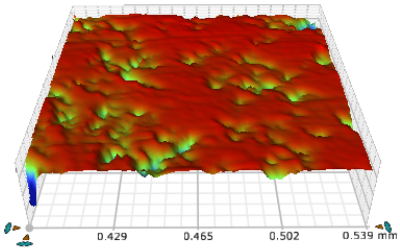


Figure 3.7: Detail of surface topography of the ball after 60 minutes at the lowest velocity ($v =$ 0.100 m/s) - continuous test.

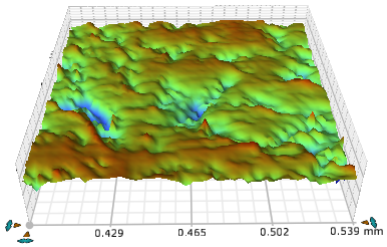


Figure 3.8: Detail of surface topography of the ball after 60 minutes at the medium velocity ($v = 0.150$ m/s) - continuous test.

To analyze the surface evolution, surface roughness profiles were obtained using Vision64 for all three tests from a middle line of the wear track. This represents the height and valley distribution along the evaluation distance (middle of the track along x-direction) and highlighting the

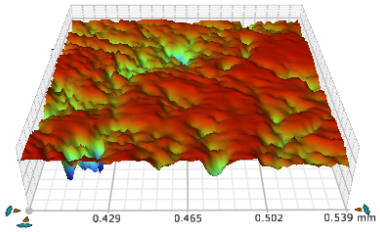


Figure 3.9: Detail of surface topography of the ball after 60 minutes at the highest velocity ($v = 0.300$ m/s) - continuous test.

micro-geometry and characteristic peaks and valleys of the finish. The results obtained are presented in Figures 3.10 through 3.12, where the cursors *R* and *M* denote the reference starting point and the maximum evaluation limit, respectively. In all graphs, the characteristic phenomenon of running-in is visually evident. There is a flattening and elimination of the most prominent peaks from the original height distribution, while maintaining the macroscopic geometry and adapting the micro-geometry to the contact. At the lower velocity, the profile frequently crosses the mean line with more pronounced and sharp valleys reaching significant depths, indicating greater asperity interaction. For the intermediate velocity, the dispersion around the mean line becomes more attenuated and symmetrical, with shallower valleys, reflecting a better separation of the surfaces by the lubricant film. Finally, for the highest velocity, although isolated deep valleys exist, the overall oscillation around the mean line exhibits a more stable and uniform behavior, validating the accelerated transition to steady-state conditions with reduced surface damage.

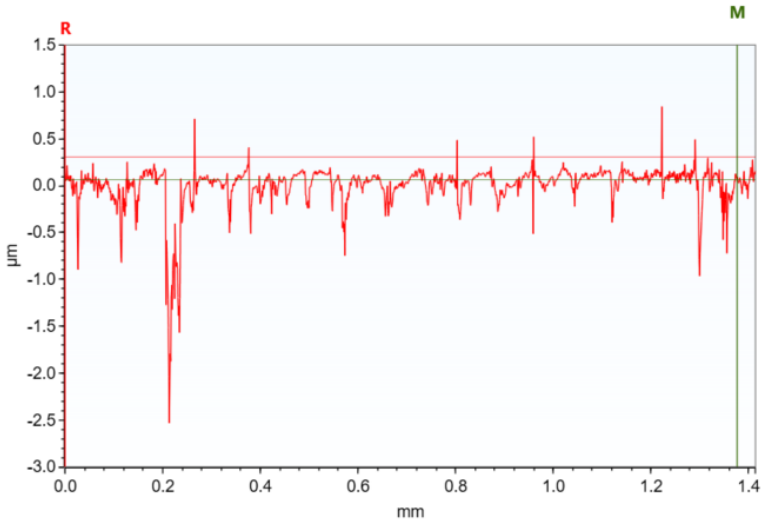


Figure 3.10: Surface roughness profile along the wear track after continuous test at a sliding speed of 0.100 m/s.

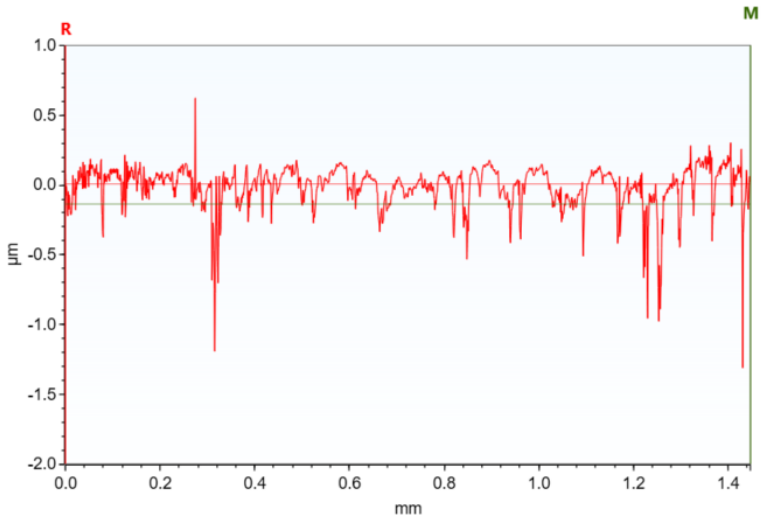


Figure 3.11: Surface roughness profile along the wear track after continuous test at a sliding speed of 0.150 m/s.

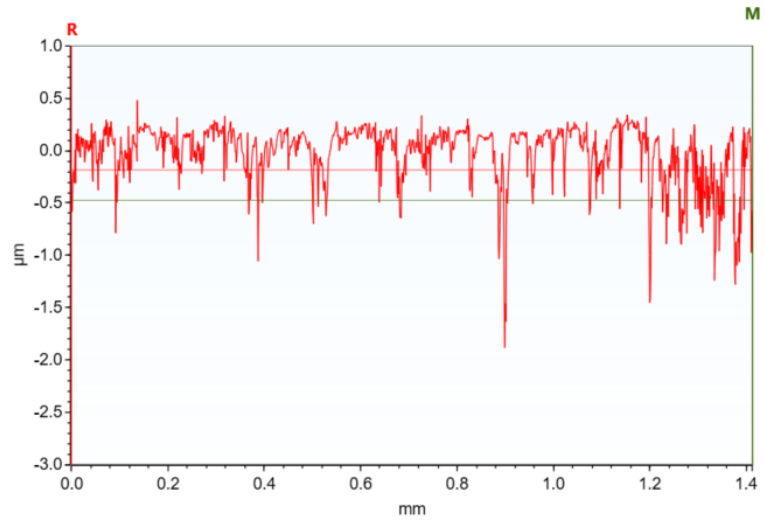


Figure 3.12: Surface roughness profile along the wear track after continuous test at a sliding speed of 0.300 m/s.

3.2.2 Interrupted Progressive Tests

Following the analysis of the results obtained in Figure 3.5, the stop times detailed in Table 3.7 were defined. At 60 s, an initial peak in the COF is observed across all curves, followed by a primary decrease at approximately 120 s. Subsequently, a minor stabilisation of the COF occurs at around 240 s for almost all curves. Regarding the stabilisation phase, the $V_e = 0.300$ m/s curve stabilises at 600 s, while the other velocities reach stability at roughly 1200 s. Furthermore, at 1620 s (27 min), a minor yet noticeable increase in the COF occurs for the highest velocity. Finally, the 2700 s (45 min) mark was specifically chosen to acquire additional data points prior to the conclusion of the tests. These specified events can be observed in Figure 3.13.

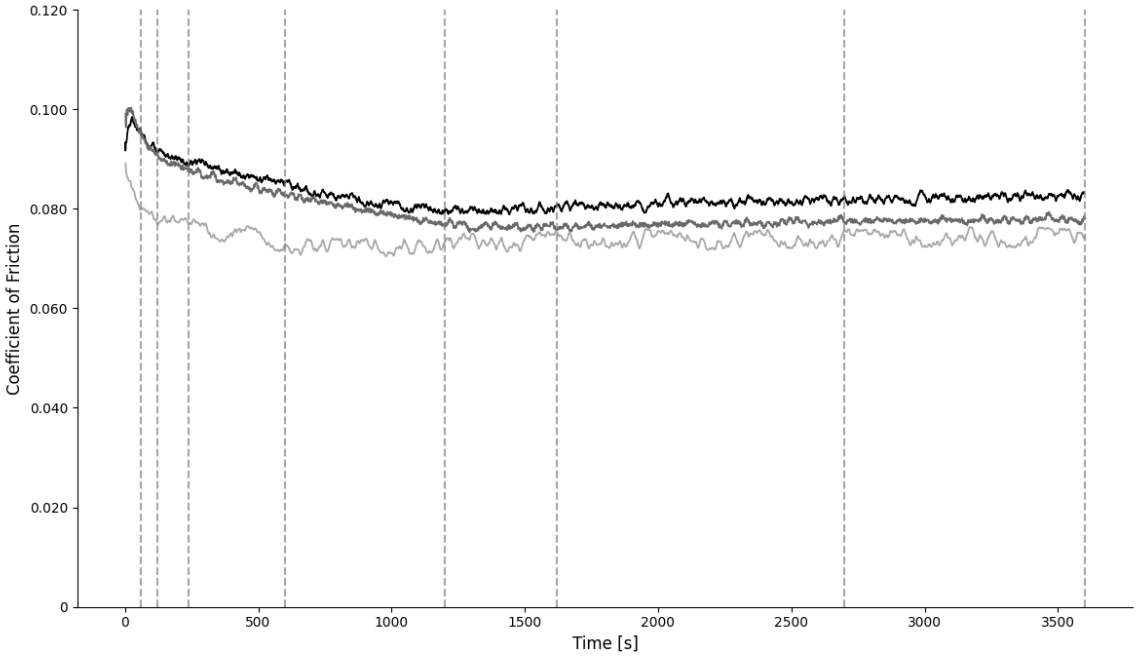


Figure 3.13: Evolution of the coefficient of friction indicating the selected test interruption and evaluation times.

Additionally, to monitor the stops, the summits parameters values were taking into account. The results are presented in Tables 3.7 and 3.8, they are consistent with the previous observations, confirming that higher sliding speeds lead to a greater lubricant film thickness. This enhanced film thickness provides superior separation between the interacting surfaces, effectively protecting the asperities and reducing direct asperity contact, which consequently limits severe wear and plastic deformation during the running-in phase.

Table 3.7: Ball surface roughness evolution (S_a and S_q) over time for different velocities.

Time (min)	$v = 0.100$ **m/s**		$v = 0.150$ **m/s**		$v = 0.300$ **m/s**	
	S_a (µm)	S_q (µm)	S_a (µm)	S_q (µm)	S_a (µm)	S_q (µm)
0	0.339	0.456	0.336	0.447	0.341	0.450
1	0.257	0.355	0.194	0.270	0.217	0.300
2	0.184	0.252	0.206	0.278	0.236	0.368
4	0.219	0.312	0.197	0.276	0.185	0.253
10	0.205	0.294	0.170	0.237	0.205	0.296
20	0.195	0.277	0.166	0.237	0.182	0.266
27	0.188	0.267	0.205	0.355	0.178	0.258
45	0.176	0.247	0.186	0.279	0.172	0.244
60	0.157	0.238	0.180	0.272	0.181	0.289

Table 3.8: Ball functional parameters evolution (S_{pk} and S_{vk}) over time for different velocities.

Time (min)	$v = 0.100$ **m/s**		$v = 0.150$ **m/s**		$v = 0.300$ **m/s**	
	S_{pk} (µm)	S_{vk} (µm)	S_{pk} (µm)	S_{vk} (µm)	S_{pk} (µm)	S_{vk} (µm)
0	0.307	0.710	0.340	0.708	0.339	0.725
1	0.174	0.682	0.244	0.504	0.210	0.577
2	0.215	0.449	0.175	0.533	0.296	0.722
4	0.276	0.600	0.155	0.525	0.257	0.432
10	0.180	0.605	0.197	0.432	0.164	0.645
20	0.178	0.552	0.168	0.433	0.204	0.532
27	0.147	0.532	0.182	0.627	0.163	0.537
45	0.231	0.470	0.182	0.554	0.152	0.480
60	0.178	0.475	0.235	0.535	0.267	0.554

Thus, for the interrupted tests, the resulting COF curves versus time for the three velocities, after applying the simple moving average, are presented in Figure 3.14. As observed in the continuous tests, a consistent trend is identified: an increase in sliding velocity leads to a decrease in the final coefficient of friction.

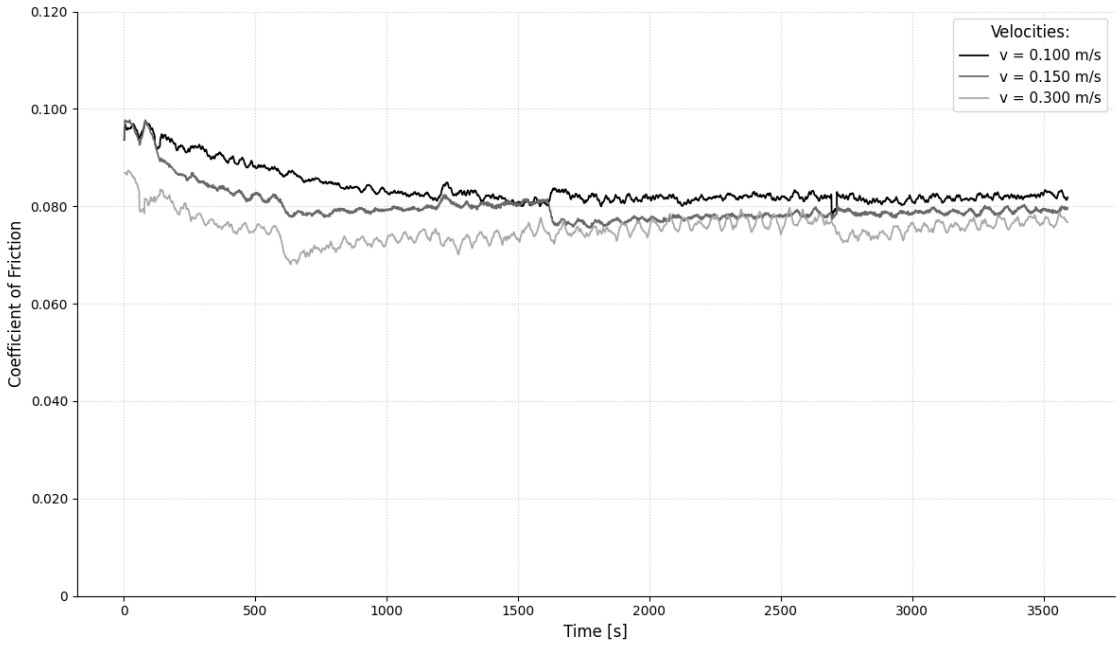
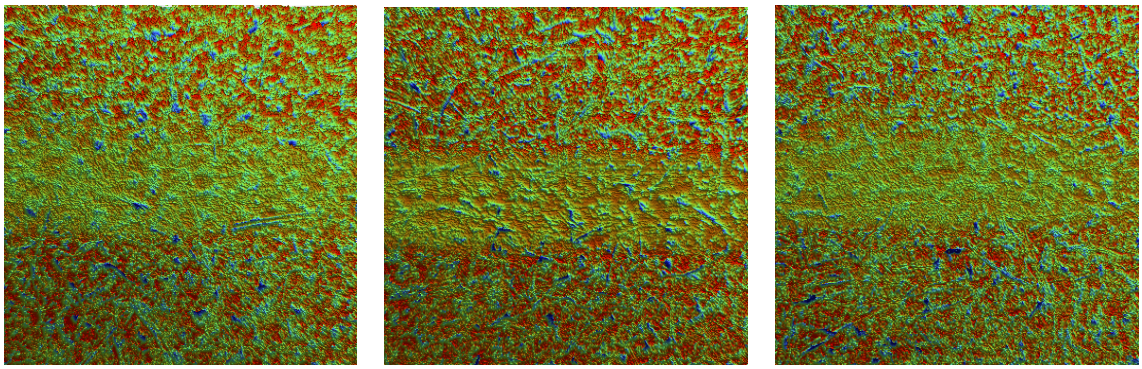


Figure 3.14: Evaluation of COF over time for all tests - interrupted tests.

It can be noted that the established stop times follow the same behavioral trends observed in the continuous tests. Specifically, the early pauses (60 s, 120 s, and 240 s) effectively capture the steep initial run-in period and primary friction peak. Furthermore, the intermediate stops (such as 600 s and 1200 s) correspond precisely to the transition between running-in and steady-state behavior across different sliding speeds, while the later intervals (1620 s and 2700 s) successfully monitor the long-term surface adaptation and lubricant behavior prior to test completion.

Figure 3.15 presents the topography of each surface for these tests. A distinct central horizontal wear track is again clearly observable, which is also discernible to the naked eye as evidenced by Figures 3.16. At the lowest velocity (Figure 3.15 a), a higher degree of plastic deformation is noted, which is justified by the thinner lubricant film thickness. For the medium velocity (Figure 3.15 b), an increased asymmetry within the wear zone becomes apparent. Finally, at the highest velocity (Figure 3.15 c), the wear track exhibits a less aggressive appearance in terms of surface material removal or deformation, which is consistent with the recorded COF values. Consequently, enhanced protection between the interacting surfaces is provided by the lubricant film thickness. Overall, it can be concluded that under identical conditions of load, temperature, SRR, and test duration, a higher entrainment speed results in reduced surface wear.

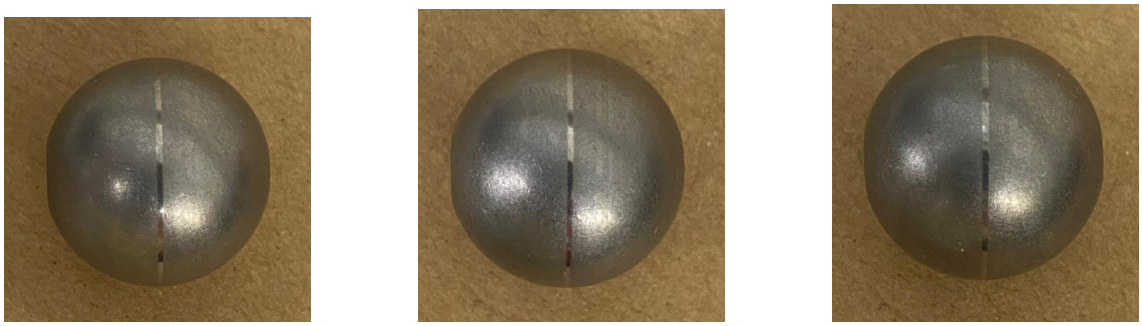


(a) Lowest velocity (0.100 m/s): S_a from 0.339 to 0.157 μm; S_q from 0.456 to 0.238 μm.

(b) Medium velocity (0.150 m/s): S_a from 0.336 to 0.180 μm; S_q from 0.447 to 0.272 μm.

(c) Highest velocity (0.300 m/s): S_a from 0.341 to 0.181 μm; S_q from 0.450 to 0.289 μm.

Figure 3.15: Topography of each ball surface after 60 minutes in the interrupted tests.



(a) Lowest velocity.

(b) Medium velocity.

(c) Highest velocity.

Figure 3.16: Balls surface at naked eye.

Detailed magnifications of specific surface areas to better understand the surface condition of the balls following the interrupted tests are presented in Figures 3.17 through 3.19. Further Figures are presented in Appendix D.

The same analysis was performed for the interrupted tests regarding the roughness profile along the wear track after 60 minutes (Figures 3.20 to 3.22). It is noticeable that the flattening of the summits is less evident than in the initial continuous profiles, with the height distribution

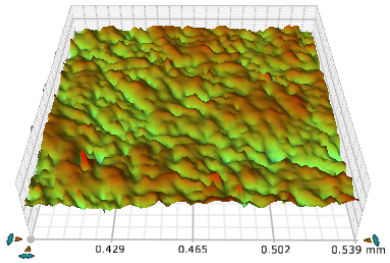


Figure 3.17: Detail of surface topography of the ball after 60 minutes at the lowest velocity ($v = 0.100$ m/s) - interrupted test.

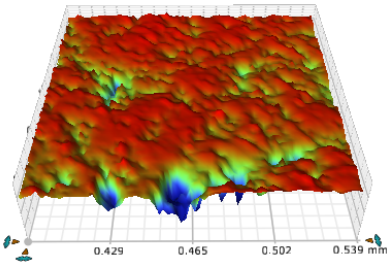


Figure 3.18: Detail of surface topography of the ball after 60 minutes at the medium velocity ($v = 0.150$ m/s) - interrupted test.

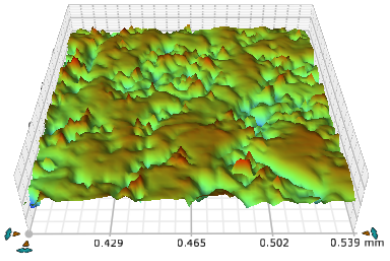


Figure 3.19: Detail of surface topography of the ball after 60 minutes at the highest velocity ($v = 0.300$ m/s) - interrupted test.

concentrating much more strictly around the upper mean line. The profiles from the interrupted tests exhibit sharper peaks. The topographical behavior visualized in these graphs directly explains the evolution of the COF curves over time, where continuous tests yield a lower COF, although the difference is minor.

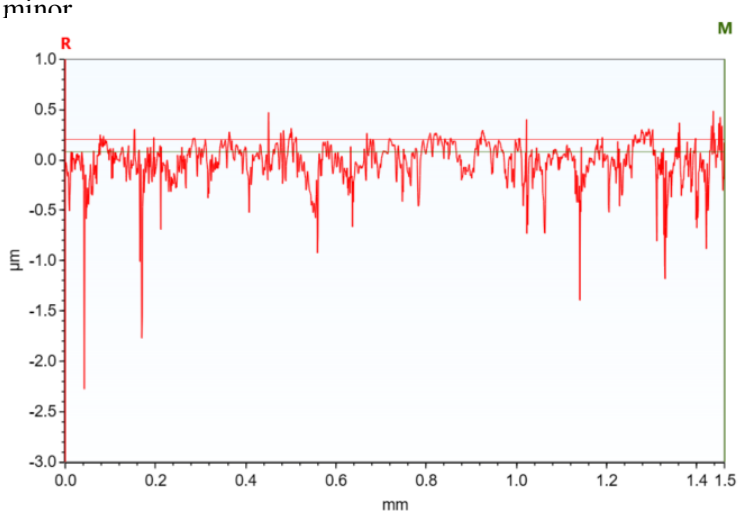


Figure 3.20: Surface roughness profile along the wear track after interrupted test at a sliding speed of 0.100 m/s.

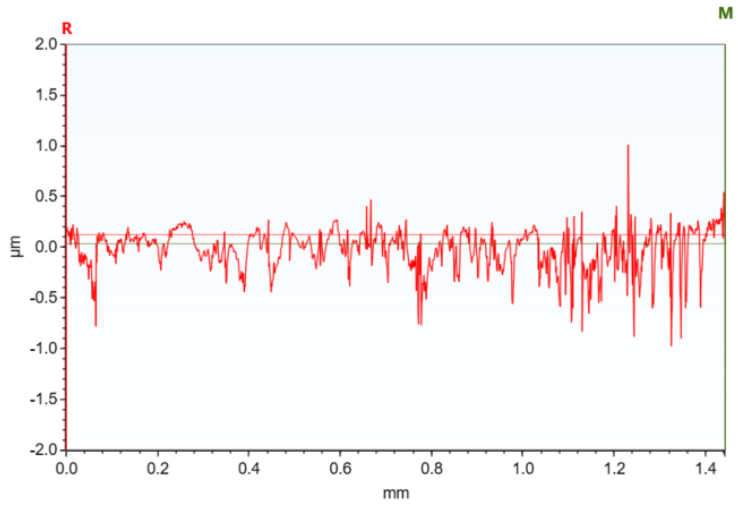


Figure 3.21: Surface roughness profile along the wear track after interrupted test at a sliding speed of 0.150 m/s.

3.3 Discussion

Due to a limitation in the EHD2 machine's data acquisition system, data recording omits the last second of each interval. Consequently, a slight difference of a few seconds appears at the end of the curves when comparing the interrupted and continuous tests. Future experimental procedures should take this technical detail into account to ensure complete data synchronization. Accordingly, the time versus coefficient of friction graphs, alongside the corresponding surface topography images comparing the continuous and interrupted tests, were plotted for each velocity. Figures 3.23 to 3.25 show the results obtained.

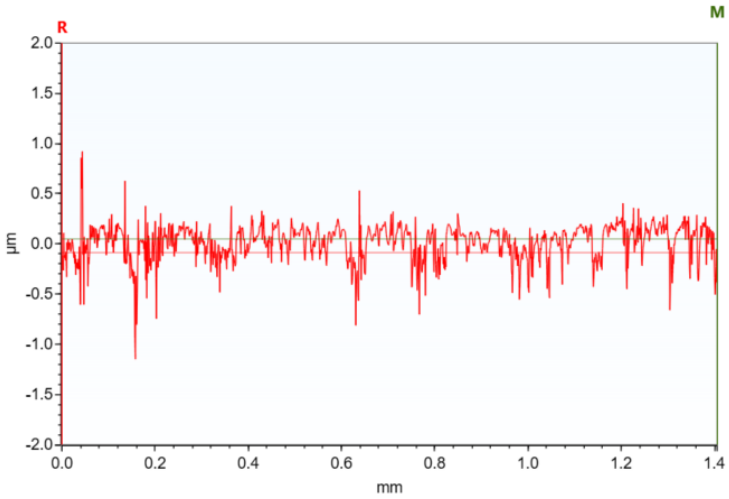


Figure 3.22: Surface roughness profile along the wear track after interrupted test at a sliding speed of 0.300 m/s.

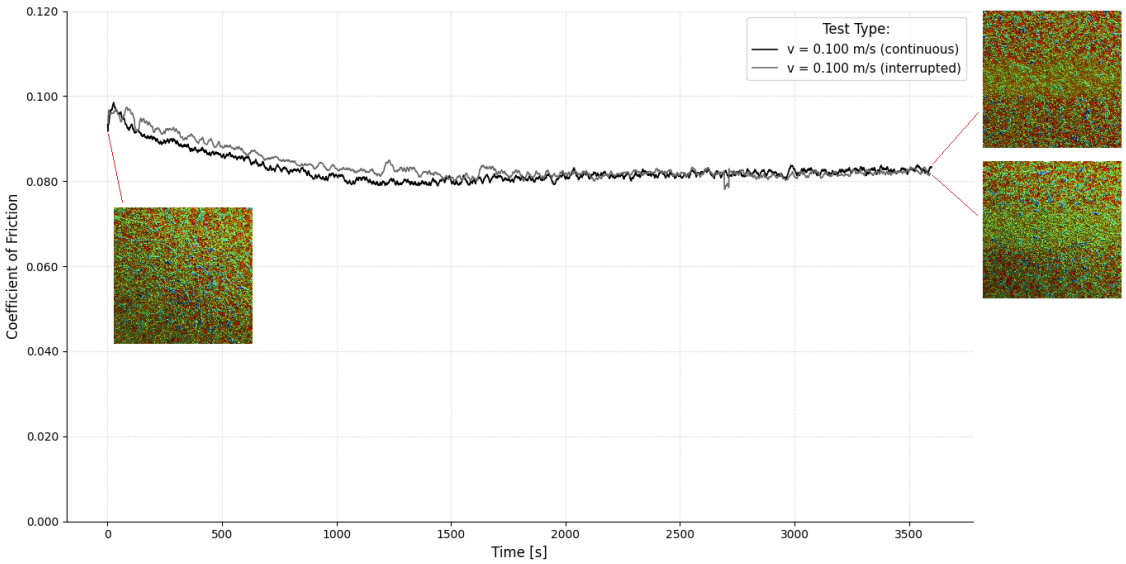


Figure 3.23: Evaluation of COF over time for both $V_e = 0.100$ m/s tests.

From Figure 3.23, a higher coefficient of friction was obtained for the interrupted test compared to the continuous test during the majority of the test duration. Towards the end, this velocity condition showed curves that were most closely overlapped following the running-in phase. Additionally, both curves stabilised at approximately the same time (around 1200 s), exhibiting a similar running-in duration. Analyzing Figures 3.10 and 3.20, it is evident that the surface asperities underwent a more uniform flattening during the continuous test, indicating a higher degree of surface wear. Furthermore, the number of residual micro-grooves observed in the continuous test was lower than that obtained in the interrupted test.

In the interrupted test of the medium velocity, it is already mentioned that at the 27 minute stop, a lubricant change occurred, which can explain the drop in the coefficient of friction value. As previously mentioned, the lubricant was reused across the various tests. A positive result was obtained after changing the lubricant, revealing curves with similar trends, as observed in Figure

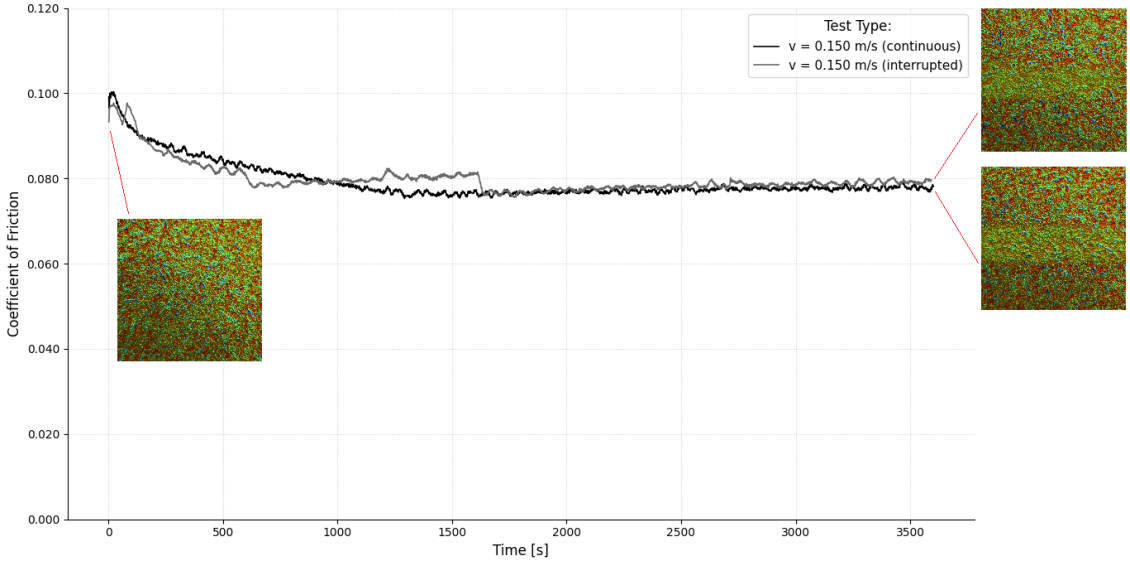


Figure 3.24: Evaluation of COF over time for both $V_e = 0.150$ m/s tests.

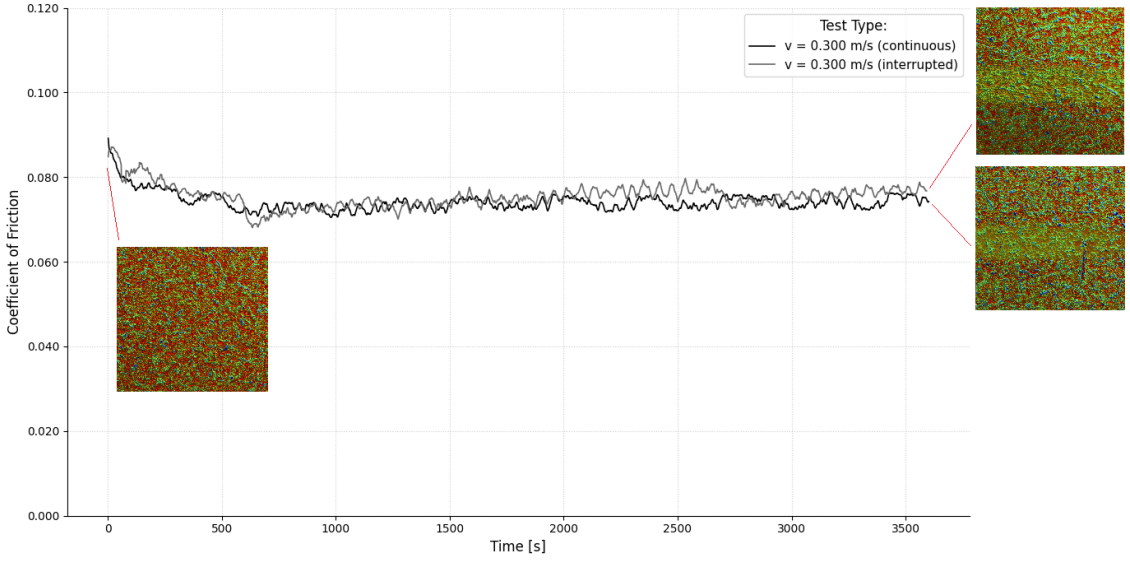


Figure 3.25: Evaluation of COF over time for both $V_e = 0.300$ m/s tests.

3.24. Regarding the surface after running-in, the same behavior is observed as for the lower speed, Figures 3.11 and 3.21. For the continuous test, the surface underwent greater plastic deformation compared to the interrupted test Figure 3.19.

The interrupted test for the highest velocity exhibited the most closely aligned curve evolution compared to the continuous test throughout the entire test duration, Figure 3.25. Nevertheless, this condition presented the lowest amount of observable plastic deformation, Figure 3.19, although it is somewhat difficult to distinguish from the micrographs.

While continuous tests exhibit a more stable COF evolution, the lubricant temperature was analyzed throughout the tests. The analysis of the lubricant temperature variation in interrupted tests reveals pronounced fluctuations at each stop point, in contrast to continuous tests, Figures 3.27 and 3.26, respectively. These local thermal variations can significantly influence the rheological conditions of the lubricant and, consequently, the contact established between the ball and the disc. As a perspective for future investigations, it is suggested to implement a prolonged lubricant pre-heating period, in order to ensure that the temperature remains strictly constant at 70 °C, mitigating the observed fluctuations. With reference to Tables 3.8 and 3.7, the results were plotted to analyze the evolution and temporal trend of the parameters. This evolution can be observed in Figures 3.28 through 3.31.

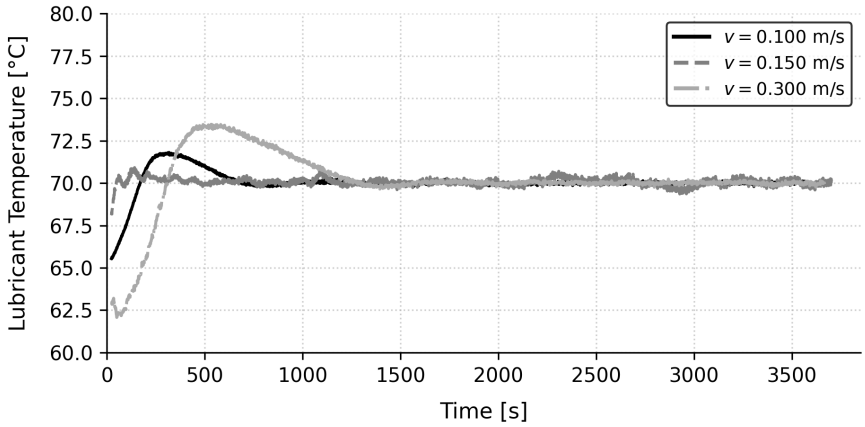


Figure 3.26: Evolution of lubricant temperature along the continuous tests.

A clear decreasing trend over time is evident. It is worth highlighting that for the lowest sliding speed ($v = 0.100$ m/s), all parameters exhibit the lowest values at the end of the tests. This behavior indicates that lower speeds promote a lesser protection of the asperities, as previously highlighted and concluded.

To experimentally analyze the surface behavior, combined plots of S_a and COF versus time were generated, enabling the simultaneous visualization of their evolution and the correlation of the respective tribological phenomena.

A prominent running-in phase is observed during the initial stages ($t < 300$ s) of the interrupted test for all the velocities. About the lowest velocity, Figure 3.32, the surface roughness experiences a sharp decrease from an initial value of approximately 0.339 µm down to a localized minimum

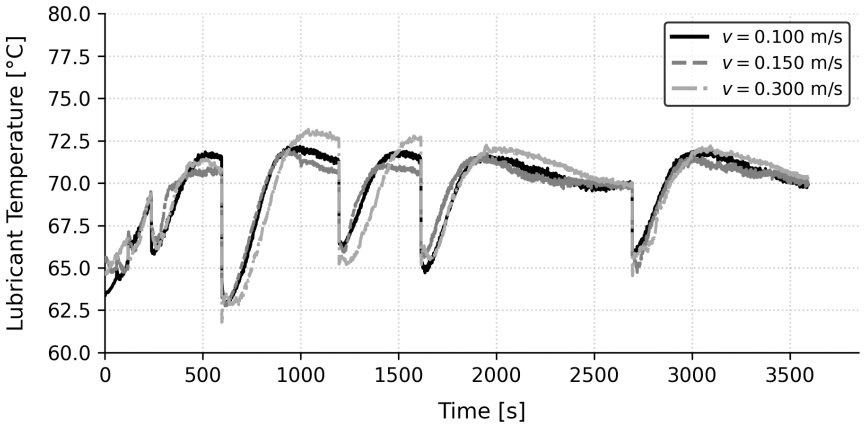


Figure 3.27: Evolution of lubricant temperature along the interrupted tests.

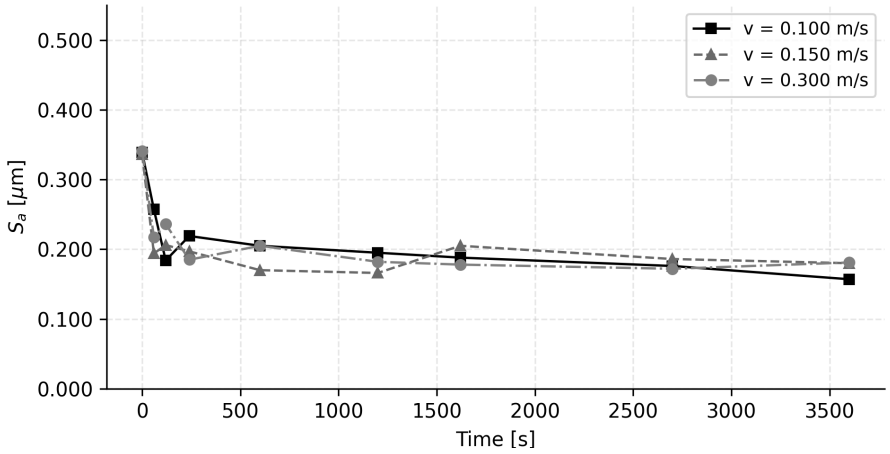


Figure 3.28: Evolution of S_a of the balls as a function of time.

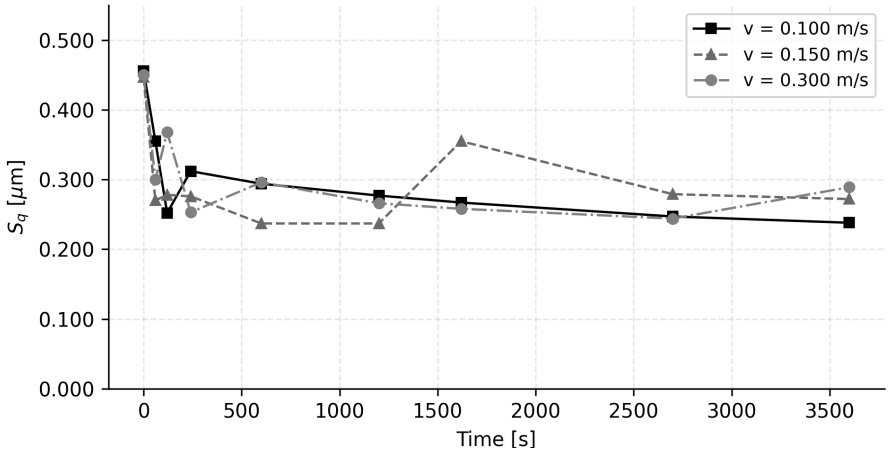


Figure 3.29: Evolution of S_q of the balls as a function of time.

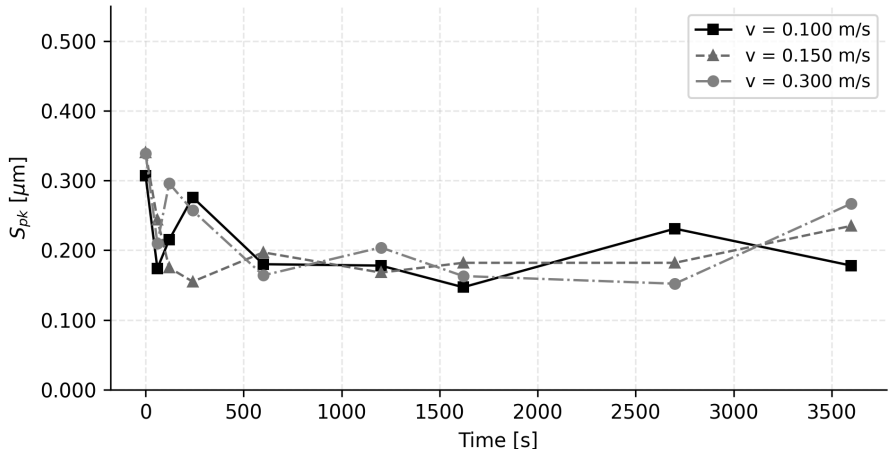


Figure 3.30: Evolution of S_{pk} of the balls as a function of time.

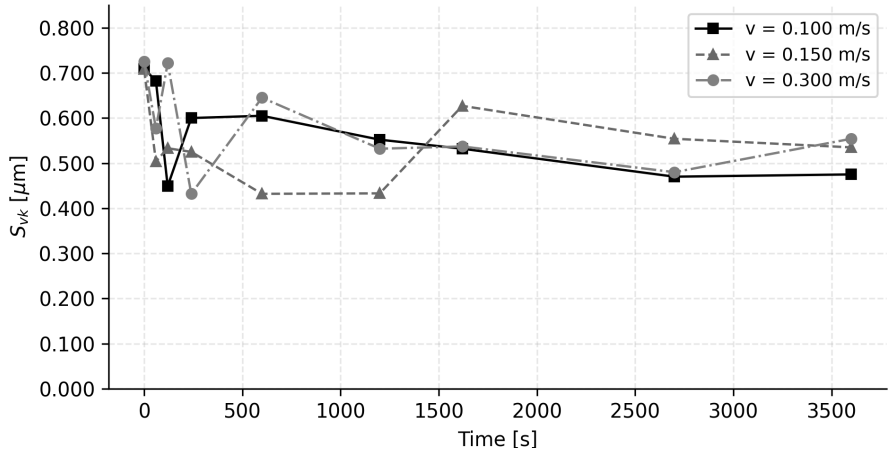


Figure 3.31: Evolution of S_{vk} of the balls as a function of time.

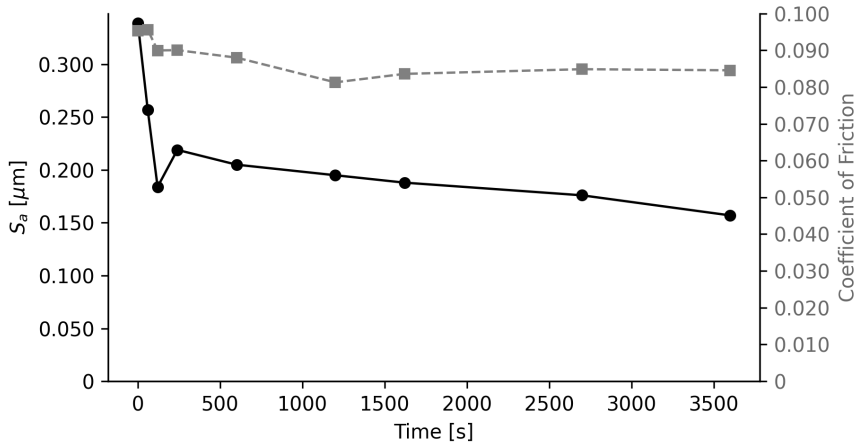


Figure 3.32: Evolution of the arithmetic mean surface roughness of the ball and the coefficient of friction as a function of time at a velocity of 0.100 m/s.

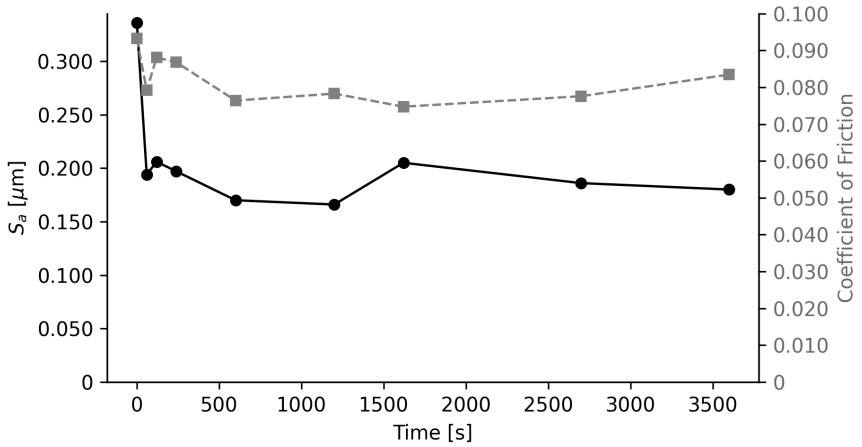


Figure 3.33: Evolution of the arithmetic mean surface roughness of the ball and the coefficient of friction as a function of time at a velocity of 0.150 m/s.

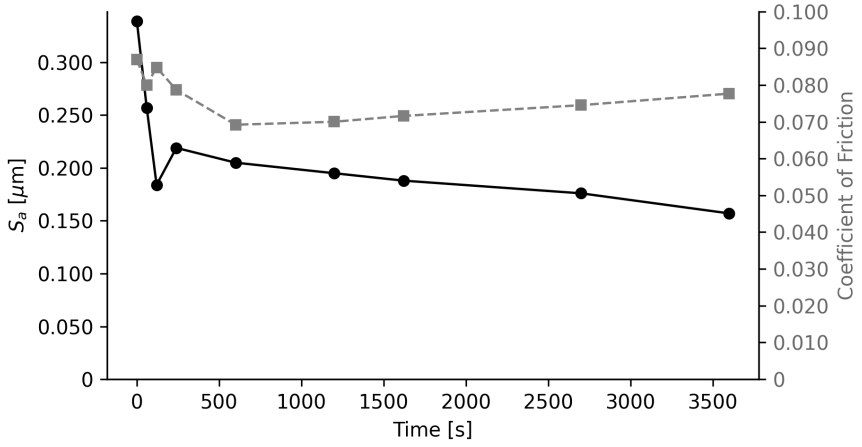


Figure 3.34: Evolution of the arithmetic mean surface roughness of the ball and the coefficient of friction as a function of time at a velocity of 0.300 m/s.

around 0.184 µm. As the test progresses into the steady-state regime ($t > 1200$ s), the surface roughness stabilizes with minor fluctuations around ≈ 0.150–0.190 µm.

Additionally, the surface roughness of the medium velocity also experiences a sharp decrease from an initial value of approximately 0.336 µm down to a localized minimum around 0.197 µm, Figure 3.33. Concurrently, the coefficient of friction rises rapidly from an initial low value of ≈ 0.010 to roughly 0.078 within the first minute. As the test progresses into the steady-state regime ($t > 1200$ s), the surface roughness stabilizes with minor fluctuations around ≈ 0.170–0.180 µm. A notable feature occurs around the 27-minute mark ($t \approx 1620$ s), where a designated lubricant change takes place, resulting in a distinct temporary decrease in the COF before returning to its stable trend around 0.070–0.075. This highlights the sensitivity of the contact to lubricant replenishment and reuse across test stages.

About the last graph, corresponding to the highest velocity, there is a sharp drop in S_a, decreasing from an initial value of 0.341 µm down to approximately 0.181 µm, Figure 3.34. Beyond this initial running-in period ($t > 600$ s), both parameters reach a steady-state regime. The surface roughness stabilizes with minor fluctuations around a mean value of ≈ 0.170–0.180 µm, while the COF remains largely constant at approximately 0.070–0.075 until the end of the 3600 s test. This behavior indicates that severe initial plastic deformation and asperity flattening occur rapidly at the highest sliding velocity, after which a stable tribological contact condition is established.

When comparing all sliding speeds, it is evident that they all exhibit classic tribological behavior, characterized by rapid initial asperity flattening and the subsequent stabilization of both S_a and the COF. However, the medium velocity condition displays a more pronounced sensitivity to operational interruptions, whereas the highest velocity maintains a smoother, more consistent curve evolution throughout the test. This indicates that higher sliding speeds promote a more rapid and stable equilibrium in the micro-geometry of the contact. Notably, the lowest velocity exhibited the most distinct and continuous decrease in S_a over time.

The evolution of the wear track width on each ball was also analyzed at each stage of the interrupted tests. As presented in Table 3.9, it is noticeable that at the final instance of the tests, increasing the sliding speed leads to a reduction in both the wear track width and, consequently, the worn area. This finding is consistent with the previously established conclusion that higher sliding speeds reduce wear and promote a more effective protection and preservation of the surface asperities.

The non-monotonic decrease in the presented results and the fluctuations observed during the interrupted tests are primarily influenced by the cropped area selected in Vision64 and the specific scanned zone chosen using the optical profiler. Furthermore, the methodology of interrupted tests introduces localized mechanical variations: at each stop, a different and potentially more severely worn zone occurs at the beginning of the test, varying according to the exact resting position of the ball. Additionally, the initial contact position on the disc for each stop differs, as it is experimentally unfeasible to ensure that precisely the same surface area is engaged upon restart. The combination of these topographical processing choices, scanning variances, and mechanical positioning differences significantly contributes to the discrepancies observed in the results. Finally,

Table 3.9: Evolution of the calculated wear track width and respective area for the three sliding speeds during interrupted tests.

Time (min)	$v = 0.100$ **m/s**		$v = 0.150$ **m/s**		$v = 0.300$ **m/s**	
	Width (mm)	Area (mm^2)	Width (mm)	Area (mm^2)	Width (mm)	Area (mm^2)
1	0.237	0.355	0.200	0.300	0.227	0.340
2	0.243	0.365	0.197	0.295	0.253	0.380
4	0.257	0.385	0.247	0.370	0.243	0.365
10	0.297	0.445	0.267	0.400	0.297	0.445
20	0.317	0.475	0.253	0.380	0.310	0.465
27	0.313	0.470	0.297	0.445	0.323	0.485
45	0.343	0.515	0.297	0.445	0.310	0.465
60	0.360	0.540	0.340	0.510	0.320	0.480

it is important to highlight that the interrupted test procedure presents certain operational risks, as the materials remain at an elevated temperature during each interruption.

3.4 Stribeck Curves

To evaluate the overall tribological performance and map the lubrication regimes across the operating window - specifically aiming to verify the effect of the entrainment speed on the Stribeck curve behavior - the Stribeck curves were plotted. To obtain the data presented in Figure 3.35, 5 steps were defined, as indicated in the instruction manual of the EHD2 machine. In these steps, the rolling speed varied within the interval of $[0.100, 3.000]$ m/s, while keeping the remaining parameters constant, described in Table 3.10.

Table 3.10: Experimental Stribeck curves test parameters.

F_N (N)	T_0 (°C)	SRR (%)	u_s (m/s)
50	70	50	$[0.100, 3.000]$

Figure 3.35 illustrates the comparison of the COF as a function of the entrainment speed for the three distinct test velocity conditions. Stribeck curves could only be obtained for these three spheres due to fatigue failure of the sphere support shaft, combined with the unavailability of replacement material.

As demonstrated by the curves, the friction coefficient exhibits a continuous decrease with increasing rolling speed, adhering to the classical Stribeck behavior. At lower speeds (approaching 0.100 m/s), the system operates predominantly within the mixed lubrication regime, where direct asperity interactions and local shear dominate the friction response. In this region, higher friction values and greater data dispersion are observed due to the thin lubricant film relative to the composite surface roughness. In opposition, as the entrainment speed increases towards higher values, the hydrodynamic lift forces become more prominent, leading to a progressive separation of the interacting surfaces and a consequent reduction in the friction coefficient towards elastohydrodynamic lubrication conditions.

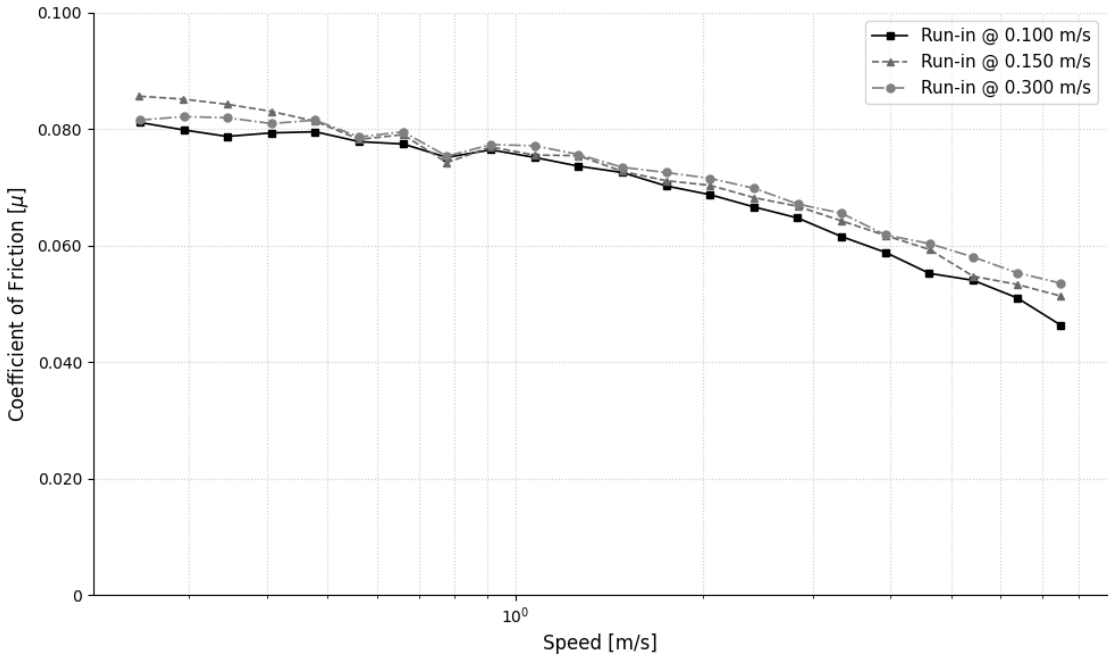


Figure 3.35: Comparison of Stribeck curves obtained as a function of entrainment speed for the three interrupted tests.

The results of the quantitative analysis of the Stribeck curves, obtained through point-by-point comparison with the reference condition of 0.300 m/s, are summarized in Table 3.11. As can be observed, the relative differences in the coefficient of friction for the velocities of 0.100 m/s and 0.150 m/s exhibit variations that progressively become more pronounced as the test velocity increases. For the velocity of 0.150 m/s, the deviations remain predominantly small and close to the reference, recording moderate fluctuations (with a maximum deviation of around -5.69% in the lower ranges). In contrast, for the lower velocity of 0.100 m/s, a more pronounced trend of negative friction deviation is observed, reaching a maximum difference of -13.46% at the highest linear velocity of the test. These data highlight the impact of the lubrication regime and sliding speed on the frictional behavior of the tests.

Additionally, since the higher velocity condition exhibits a larger COF throughout the velocity range, this behavior can be directly correlated with the higher S_{pk} values (Table 3.8) recorded for this velocity over the course of the test, in comparison to the lower velocities. A higher reduced peak height (S_{pk}) indicates a greater presence of prominent asperities on the surface, which increases localized contact pressures and mechanical interaction within the lubricated contact, thereby elevating the frictional resistance.

Based on Figure 3.35, it can be concluded that a lower sliding speed results in a lower COF. To conclusively determine which test velocity yields the lowest wear after a given running-in period, it would be beneficial for all test cases to cover the exact same sliding distance along the track. In future work, and assuming material availability, it is recommended to keep all operating conditions described throughout this dissertation strictly identical across tests.

Table 3.11: Relative differences of the coefficient of friction for 0.100 m/s and 0.150 m/s relative to the 0.300 m/s reference curve.

Speed [m/s]	**COF (Ref. 0.300 m/s)**	**Relative Difference [%]**	
		$v = 0.100$ **m/s**	$v = 0.150$ **m/s**
2999.455	0.0535	13.46	4.12
2550.921	0.0553	7.78	3.62
2169.605	0.0580	6.90	5.69
1845.779	0.0603	8.46	1.66
1568.899	0.0618	4.85	0.16
1334.899	0.0655	6.11	1.98
1135.316	0.0671	3.58	0.60
965.569	0.0698	4.58	2.29
821.232	0.0715	3.92	1.68
698.271	0.0725	3.17	1.93
594.120	0.0734	1.23	0.95
505.257	0.0756	2.65	0.26
429.542	0.0771	2.59	2.08
365.626	0.0773	1.16	0.52
310.805	0.0753	0.27	1.46
264.041	0.0795	2.64	0.63
224.669	0.0786	1.02	0.51
191.144	0.0815	2.45	0.25
162.521	0.0809	1.98	-2.60
138.158	0.0819	3.91	-2.81
117.500	0.0821	2.80	-3.65
99.928	0.0815	0.49	-5.03

Chapter 4

Application of the Model

This chapter focuses on the implementation of the numerical contact model, the extraction and application of statistical asperity summit parameters, and the comparison between theoretical predictions and experimental friction results, including Stribeck curve evaluations.

4.1 Model Implementation and Summit Parameters

The friction model implemented in this work is based on the numerical framework developed by Miguel Dias [16], which couples EHL theory with statistical asperity contact mechanics via Johnson's load-sharing concept. To accurately characterize surface topographies, it extends the Greenwood and Williamson framework by utilizing advanced non-Gaussian summit distributions (including Ex-Gaussian and Skew-Normal models) combined with a refined matrix-based summit selection criterion that scales with the principal asperity radii. While the broader framework can accommodate alternative topographical descriptions, this implementation adopts the Gaussian distribution to model the summit heights, providing a robust and established statistical foundation for the interacting surfaces. The model incorporates non-Newtonian lubricant rheology, such as the Bair-Winer limiting shear stress model, and thermal effects via an iterative flash temperature routine. Furthermore, when applied to gear transmissions, the formulation integrates gear kinematics, variable normal loads, and local radius variations along the path of contact.

To ensure consistency and accuracy, and following the methodological framework established by Miguel Dias [16], a preliminary matrix-size sensitivity study was conducted. The analysis demonstrated that employing a 3×3 matrix configuration yields topographical and friction predictions that align most closely with the experimental data. This can also be seen in Figures 4.1 to 4.3. Increasing the matrix size for the profile of the ball for the highest velocity in the interrupted tests, the selection of the summits (red points) is lower.

Additionally, it was also made for the lowest velocity for the profile of the interrupted tests (Figure 4.4 and 4.5). Similar outcomes were observed. Therefore, a 3×3 matrix configuration was adopted for all profiles. Although the best results in Miguel Dias's work were obtained with a 7×7 matrix configuration, this finding aligns with the recommendation cited in his dissertation:

"Yet, it is important to analyze the selected summits of each matrix to make sure that the summit definition is accurate and if the matrix size is correct when used in other test samples.".

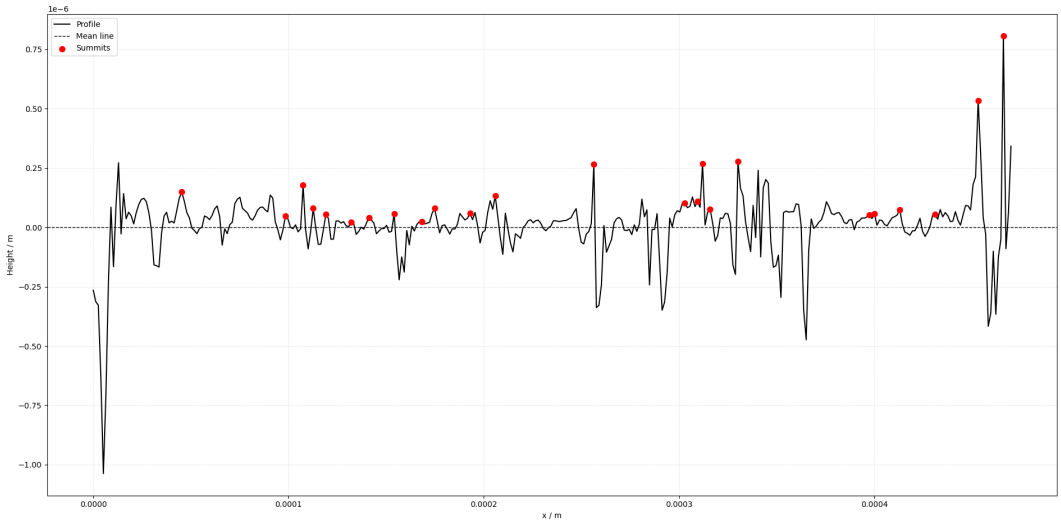


Figure 4.1: Profile showing the summit selection with matrix size of 3x3 - $V_e = 0.300$ m/s interrupted test at t = 60 min.

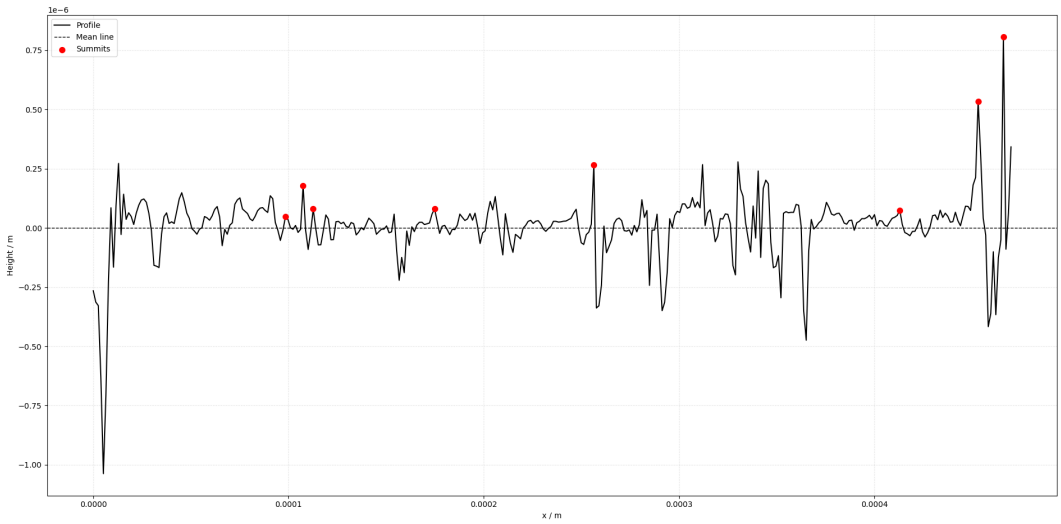


Figure 4.2: Profile showing the summit selection with matrix size of 5x5 - $V_e = 0.300$ m/s interrupted test at t = 60 min.

Table 4.1 presents the statistical summit parameters (the ones described in Section 2.1.5.1) values for each continuous test, extracted using an already existent Python code. The results of the theoretical COF for the continuous tests are presented in Figures 4.8 to 4.10.

To accurately model the real contact mechanics and account for discrete micro-scale interactions during the running-in phase, statistical summit parameters for the interrupted tests were extracted at each time. For these, on each measured surface, the average of the values presented in Tables 4.2 to 4.4 was calculated for each interrupted time.

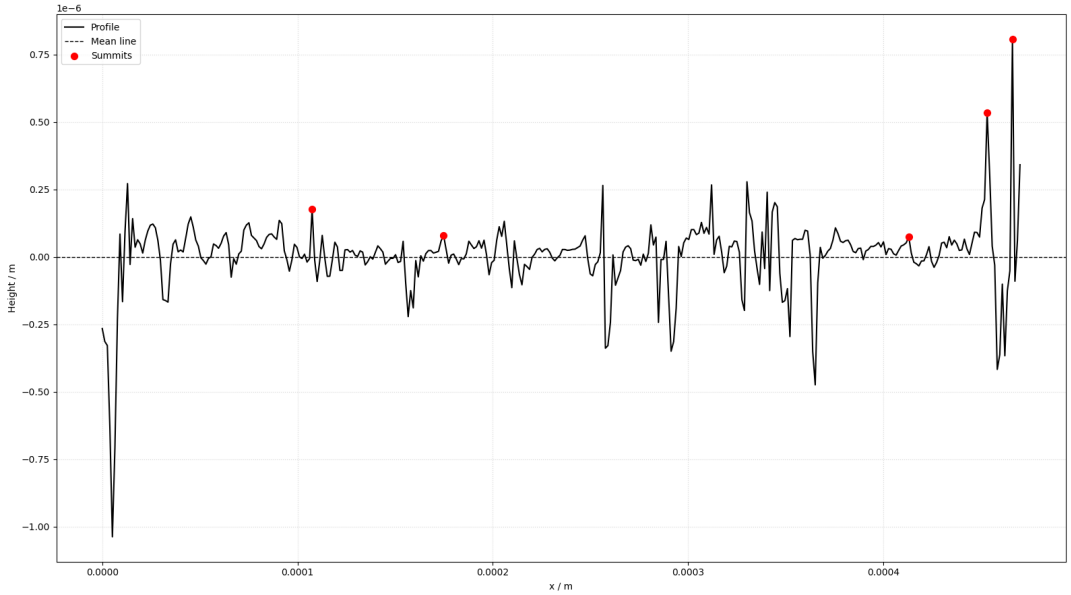


Figure 4.3: Profile showing the summit selection with matrix size of 7x7 - $V_e = 0.300$ m/s interrupted test at t = 60 min.

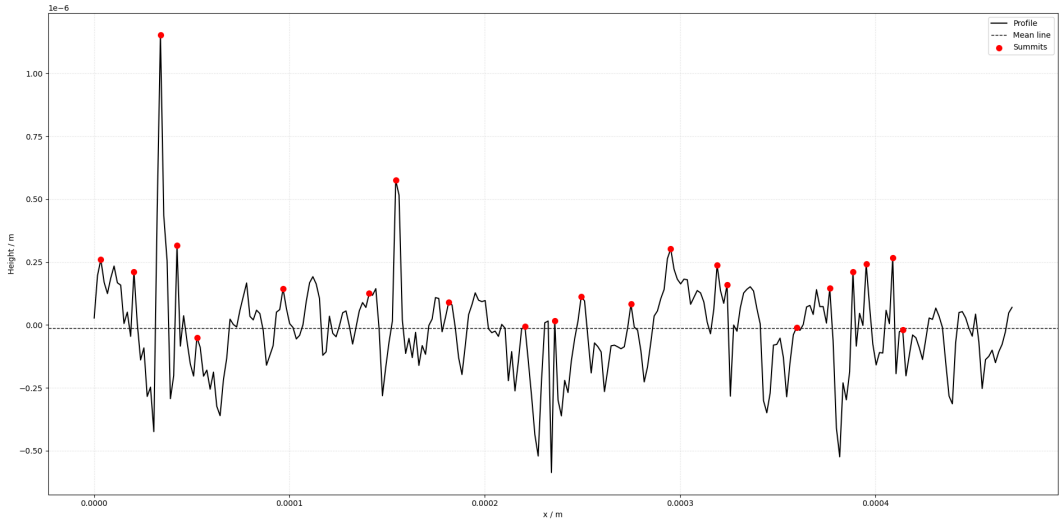


Figure 4.4: Profile showing the summit selection with matrix size of 3x3 - $V_e = 0.100$ m/s interrupted test at t = 60 min.

Table 4.1: Roughness and summit parameters for each continuous test (1-Ball and 2-Disc).

Parameter	$V_e = 0.100$ m/s	$V_e = 0.150$ m/s	$V_e = 0.300$ m/s
σ_1 (μm)	0.202	0.142	0.167
β_1 (μm)	15.676	14.819	20.595
n_1 ($\times 10^9\,\mathrm{m}^{-2}$)	37.253	47.721	39.197
σ_2 (μm)	0.184	0.152	0.180
β_2 (μm)	261.500	311.344	262.120
n_2 ($\times 10^9\,\mathrm{m}^{-2}$)	1.725	1.536	1.753

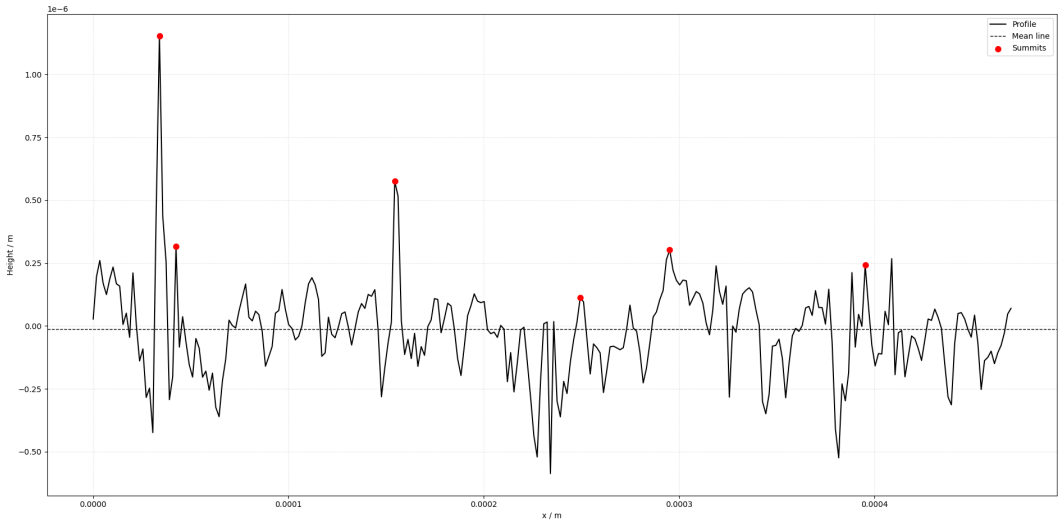


Figure 4.5: Profile showing the summit selection with matrix size of 7x7 - $V_e = 0.100$ m/s interrupted test at t = 60 min.

As observed in Tables 4.2, 4.3, and 4.4, these parameters exhibit localized fluctuations throughout the progressive stop intervals (from Stop 1 to Stop 8).

Table 4.2: Roughness and summit parameters for each time (1-Ball and 2-Disc) - $V_e = 0.100$ m/s.

Stop	σ_1 (μm)	β_1 (μm)	n_1 ($\times 10^9\,\mathrm{m}^{-2}$)	σ_2 (μm)	β_2 (μm)	n_2 ($\times 10^9\,\mathrm{m}^{-2}$)
1	0.2562	11.0090	33.1931	0.1572	231.6695	2.1801
2	0.2138	3.5037	112.6270	0.1592	207.1221	2.3553
3	0.2301	9.2845	38.8934	0.1558	194.3368	2.5139
4	0.1849	15.6008	35.5846	0.1891	304.3352	1.4603
5	0.1977	12.2910	34.0648	0.1830	290.4458	1.6101
6	0.1742	11.3269	45.3805	0.2045	271.0115	1.6740
7	0.1522	12.0377	38.3064	0.1733	311.7342	1.6182
8	0.1794	11.1975	36.4105	0.1812	285.4210	1.5842

Table 4.3: Roughness and summit parameters for each time (1-Ball and 2-Disc) - $V_e = 0.150$ m/s.

Stop	σ_1 (μm)	β_1 (μm)	n_1 ($\times 10^9\,\mathrm{m}^{-2}$)	σ_2 (μm)	β_2 (μm)	n_2 ($\times 10^9\,\mathrm{m}^{-2}$)
1	0.2240	6.9777	44.2725	0.1017	242.7748	2.2972
2	0.1664	7.1604	46.9490	0.1000	238.7504	2.4528
3	0.1586	11.5558	37.2235	0.0778	182.7392	3.3178
4	0.1421	10.8331	45.1388	0.0899	250.4971	2.4656
5	0.1698	11.8002	41.7052	0.0959	251.9350	2.4492
6	0.1573	12.9329	44.5426	0.0993	262.4192	2.2782
7	0.1721	11.0603	44.6467	0.0720	230.7458	2.8467
8	0.1207	7.4048	60.1974	0.1053	420.0111	2.2898

Rather than displaying a strictly monotonic decrease, the topographical parameters reflect the transient nature of the running-in process. During initial stages, the highest asperities undergo

Table 4.4: Roughness and summit parameters for each time (1-Ball and 2-Disc) - $V_e = 0.300$ m/s.

Stop	σ_1 (μm)	β_1 (μm)	n_1 ($\times 10^9\,\mathrm{m}^{-2}$)	σ_2 (μm)	β_2 (μm)	n_2 ($\times 10^9\,\mathrm{m}^{-2}$)
1	0.1641	11.0576	39.3842	0.0996	191.9610	3.0889
2	0.1496	14.9848	37.5067	0.1043	178.9780	2.6747
3	0.1655	11.6039	37.5969	0.1088	252.2996	2.2481
4	0.1487	15.2803	42.6518	0.0760	285.2949	2.5283
5	0.1324	16.8950	41.2010	0.1019	223.3123	2.5566
6	0.1339	15.0683	47.9276	0.0705	171.1964	3.4779
7	0.1364	13.1589	49.4985	0.0905	283.6056	2.4168
8	0.1362	15.4049	51.7385	0.1492	205.0143	2.6781

severe plastic deformation and mechanical smoothing, which temporarily alters local peak distributions and summit radii. Moreover, the mean value for each parameter decreases with the increase of the sliding velocity.

Overall, tracking the evolution of σ, β, and n provides crucial input data for the stochastic friction model, validating that surface micro-geometry dynamically adapts until a steady-state condition is achieved. Furthermore, the extracted summit parameters are inherently dependent on the specific measurement area selected via optical profiler along the wear track. Due to the spatial heterogeneity and micro-structural variations inherent to the wear track, the exact location and boundaries of the scanned region directly influence the statistical computation of asperity height dispersion, summit radius, and asperity density. This can be seen in Figure 4.6.

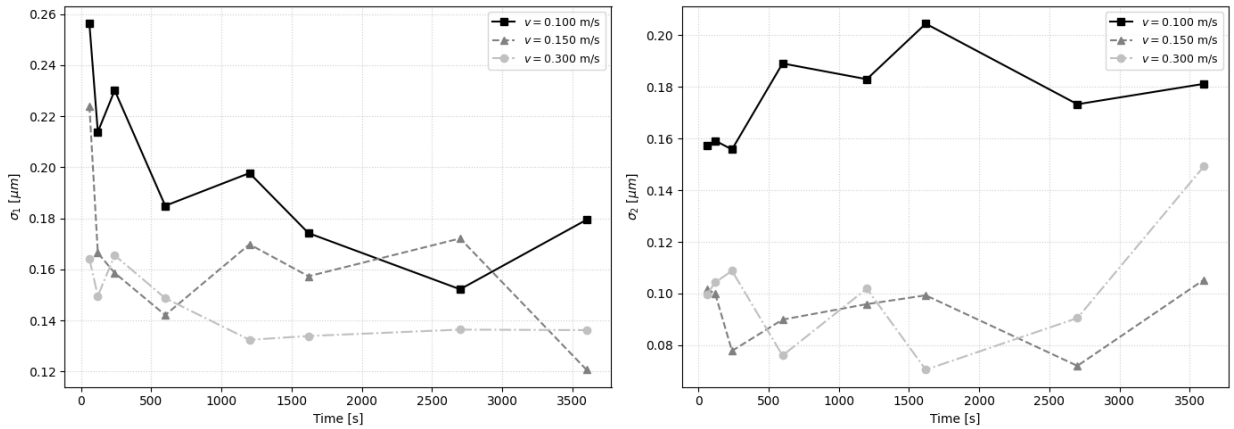
The plasticity index of the balls was calculated according to Equation 2.27. As can be observed from the equation, only the ratio between the roughness standard deviation and the asperity curvature (σ/β) varies over time. Therefore, the trend of this ratio is presented in Figure 4.7, alongside its respective values in Table 4.5.

In the previous Chapter, through the roughness parameters, it was concluded that the lowest speed condition experienced greater plastic wear. These new plasticity index data reinforce the conclusions drawn from the surface topography of the balls.

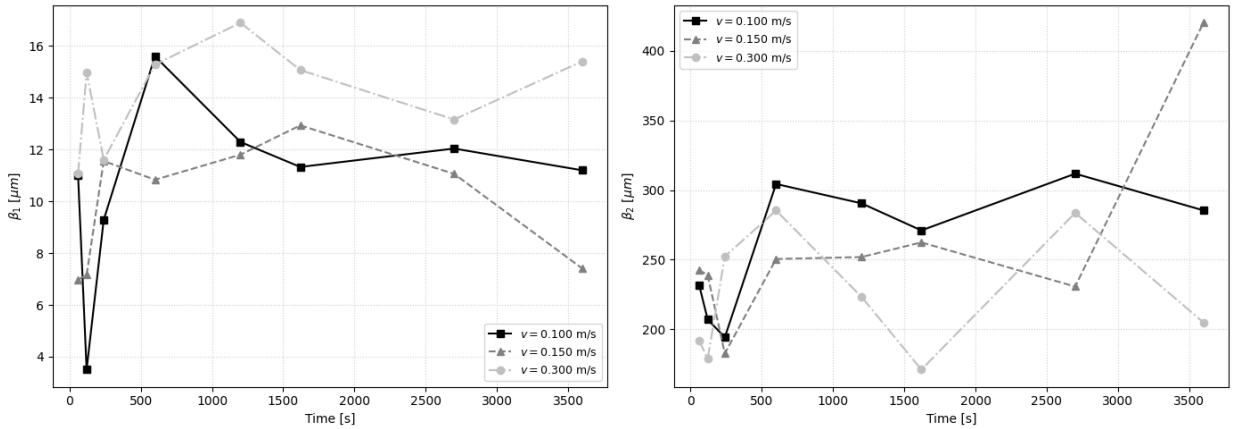
Table 4.5: Evolution of the σ/β ratio of the balls over time for different test velocities.

Time [s]	$v = 0.100$ **m/s**	$v = 0.150$ **m/s**	$v = 0.300$ **m/s**
60	0.023	0.032	0.015
120	0.061	0.023	0.010
240	0.025	0.014	0.014
600	0.012	0.013	0.010
1200	0.016	0.014	0.008
1620	0.015	0.012	0.009
2700	0.013	0.016	0.010
3600	0.016	0.016	0.009

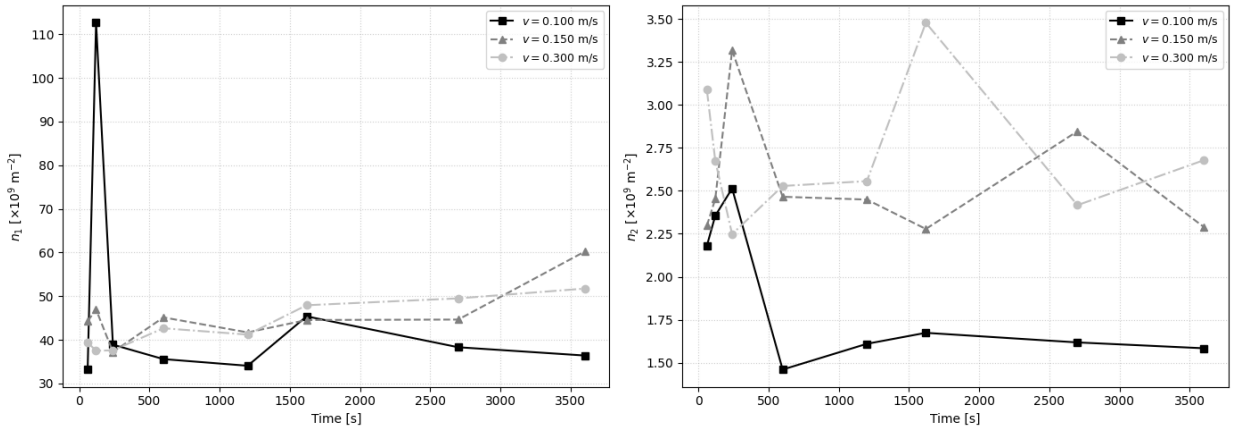
Following this trend, and multiplying it by the values of $E = 210$ GPa and hardness $H \approx 7.5$ GPa, Ψ values exceeding 1.0 are obtained for all time steps and test velocities. This indicates



(a) RMS roughness (σ_1 and σ_2).



(b) Asperity radius (β_1 and β_2).



(c) Asperity density (n_1 and n_2).

Figure 4.6: Evolution of roughness and asperity parameters as a function of time for the three sliding speeds during interrupted tests: (a) RMS roughness (σ), (b) asperity radius (β), and (c) asperity density (n).

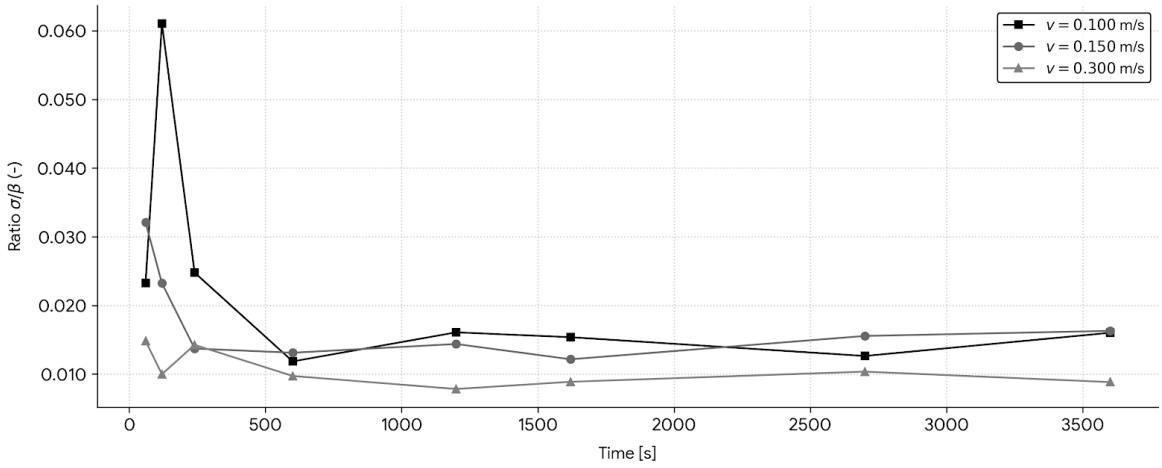


Figure 4.7: Evolution of the roughness standard deviation to asperity curvature ratio (σ/β) of the balls over time for the three test velocities.

that the system operates predominantly in the plastic regime throughout the tests, in accordance with the classical transition criterion.

For the continuous tests, the σ/β ratio was calculated for the ball surface. The values obtained were 0.013, 0.010, and 0.008 for $v = 0.100$ m/s, $v = 0.150$ m/s, and $v = 0.300$ m/s test velocities, respectively. Compared to the interrupted tests, these values were slightly lower. Overall, they do not vary significantly, which is expected since the operating conditions are identical for both continuous and interrupted tests.

4.2 Model Implementation and Adjustment

To compare the theoretical predictions with the experimental measurements, specific boundary friction parameters were defined within the numerical model. The maximum asperity contact coefficient of friction, $\mu_{c,\max}$, was set to 0.10, while the elastic-plastic transition parameter, S_{ep}, was maintained at 0.10. Although classical steel-on-steel contacts lubricated with mineral or PAO oils typically exhibit asperity friction coefficients ranging between 0.07 and 0.15 in standard engineering practice, the value of $\mu_{c,\max} = 0.10$ was selected. This fine-tuning accounts for local micro-scale adaptation and boundary film shearing characteristics established during the running-in phase under the tested operating conditions (70°C and 50 N). Additionally, the parameters from Tables 4.2 to 4.4 were implemented into the code for each corresponding test, taking into account the specific time intervals. Furthermore, since the existing model originally averaged the measured temperature and normal load from the experiments, the code was updated to read the actual instantaneous values at each time step, bringing the theoretical results closer to the experimental data. The results comparing the theoretical and experimental COF are presented in Figures 4.8 to 4.10 for the continuous tests, and in Figures 4.11 to 4.13 for the interrupted tests.

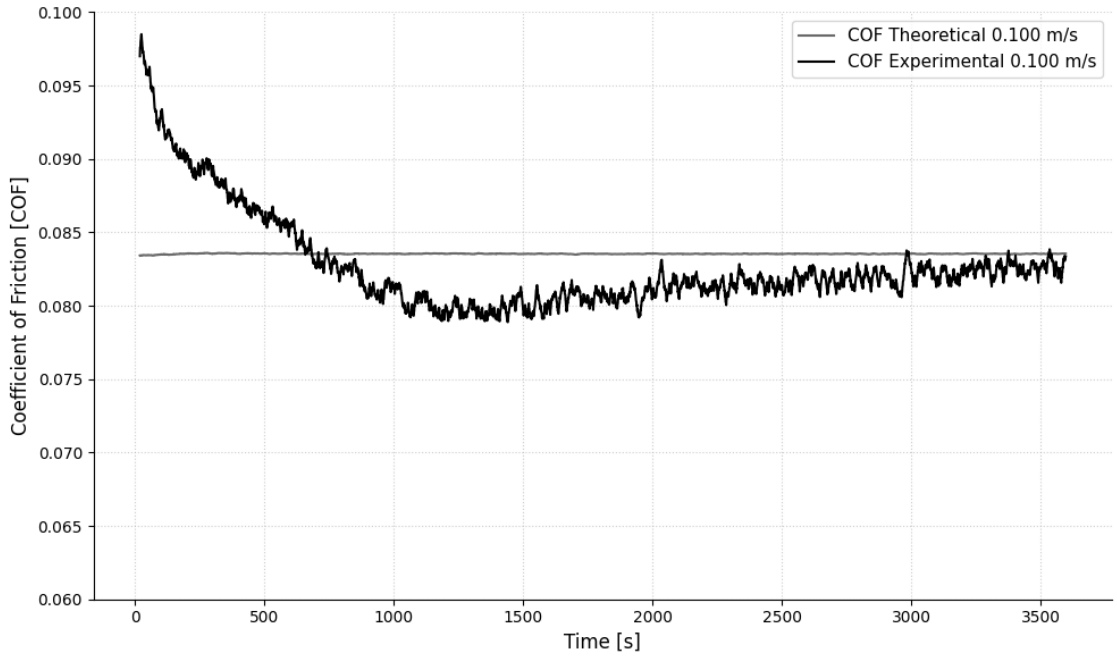


Figure 4.8: Evaluation of COF over time comparing theoretical and experimental results for the continuous test at $V_e = 0.100$ m/s.

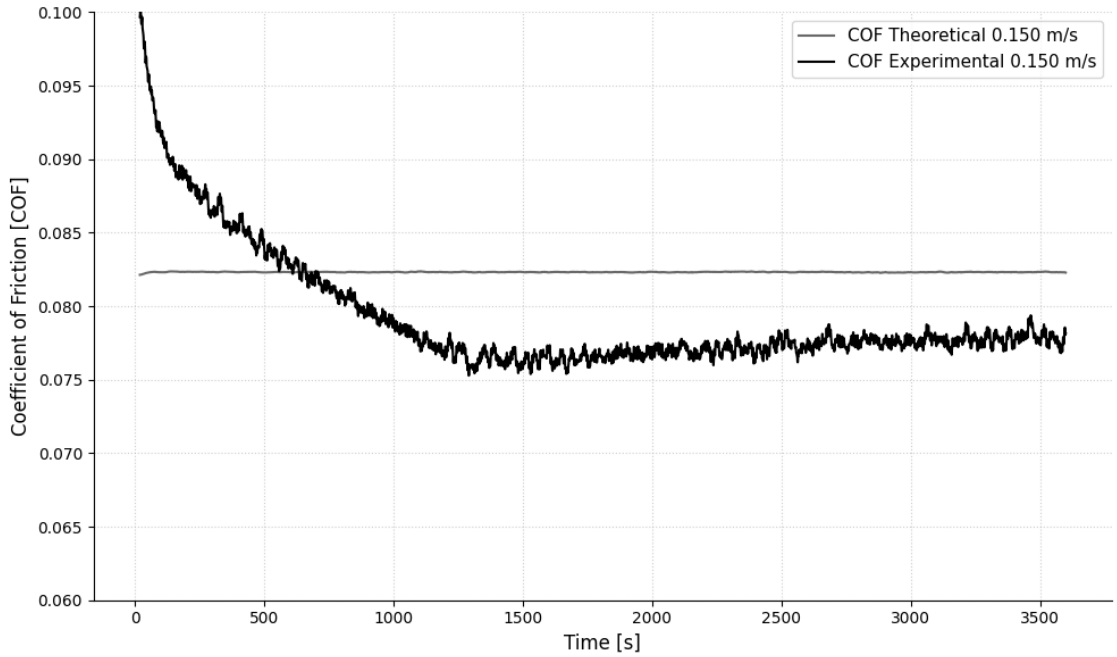


Figure 4.9: Evaluation of COF over time comparing theoretical and experimental results for the continuous test at $V_e = 0.150$ m/s.

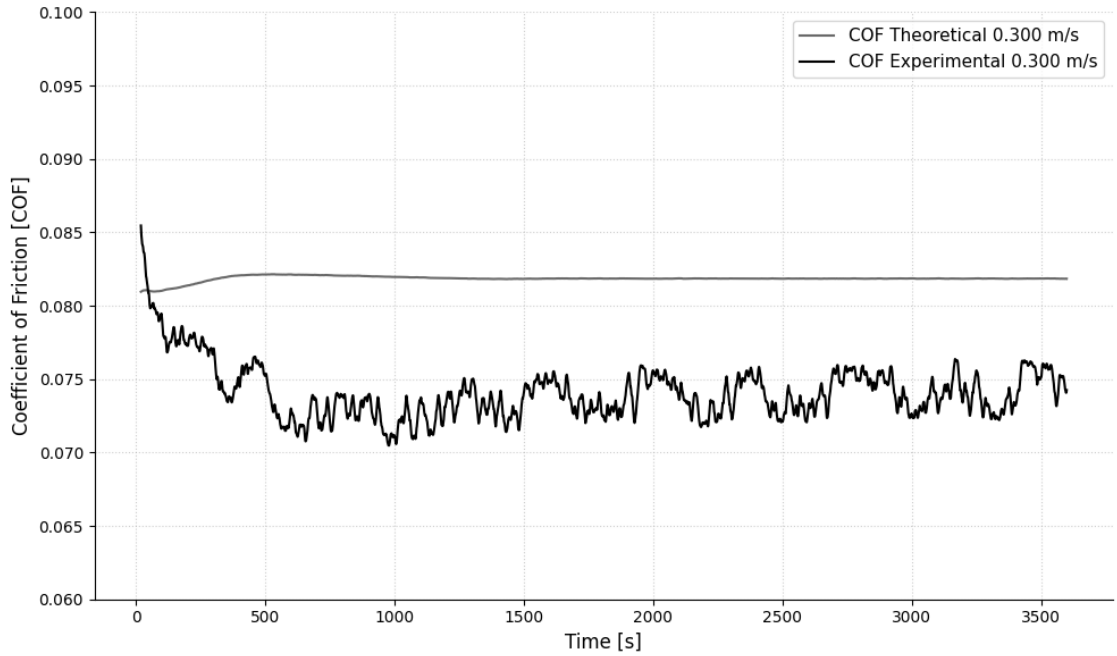


Figure 4.10: Evaluation of COF over time comparing theoretical and experimental results for the continuous test at $V_e = 0.300$ m/s.

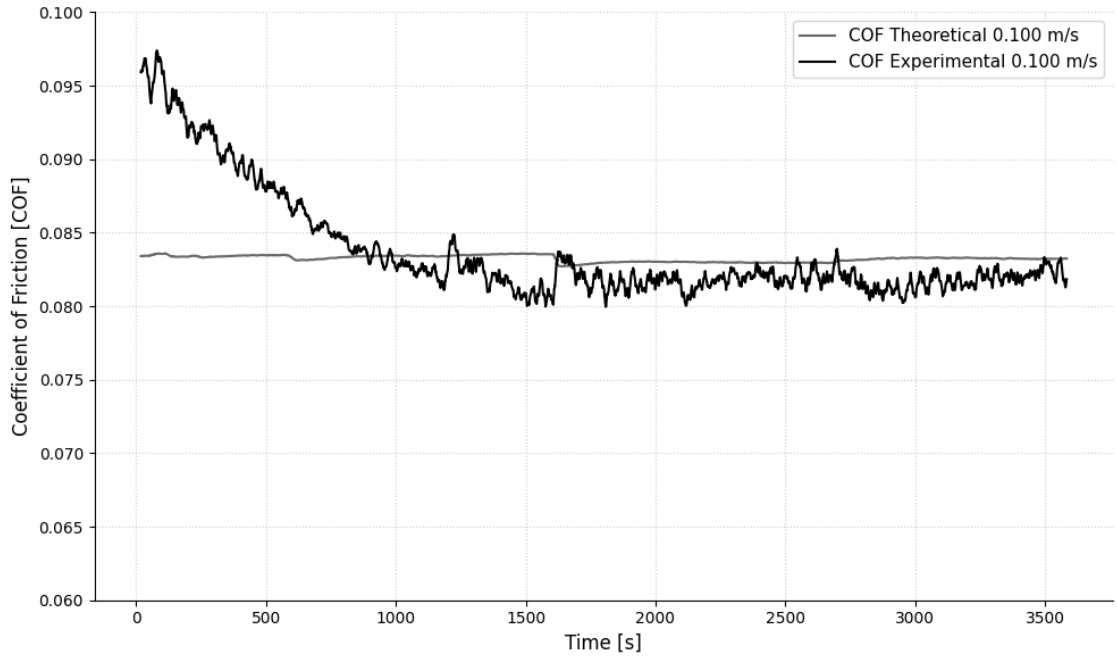


Figure 4.11: Evaluation of COF over time comparing theoretical and experimental results for the interrupted test at $V_e = 0.100$ m/s.

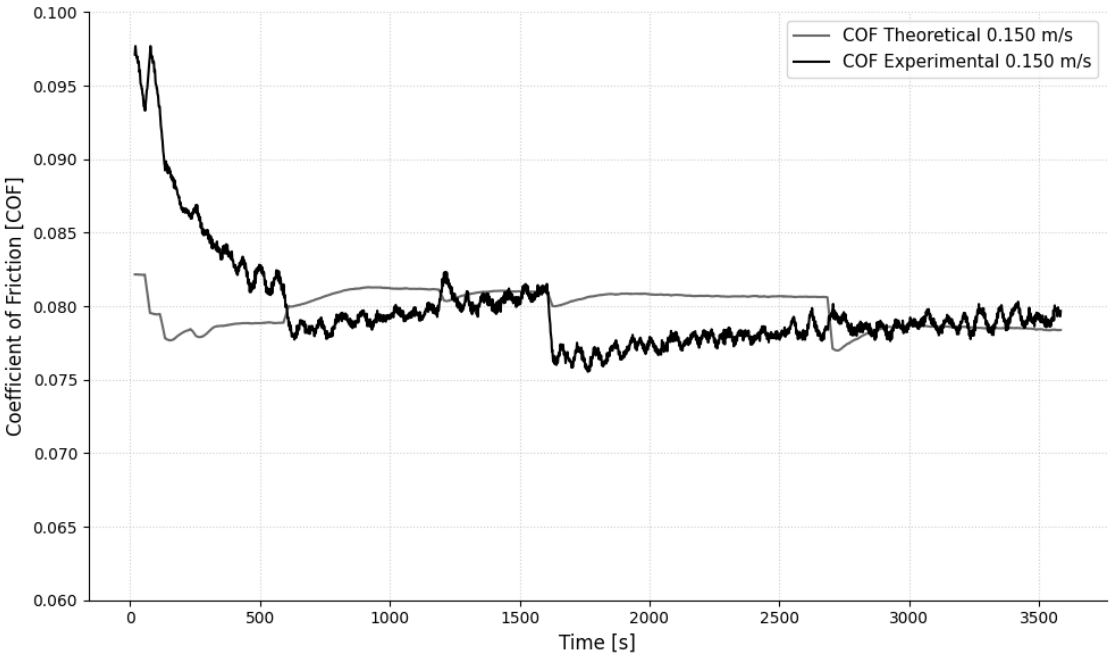


Figure 4.12: Evaluation of COF over time comparing theoretical and experimental results for the interrupted test at $V_e = 0.150$ m/s.

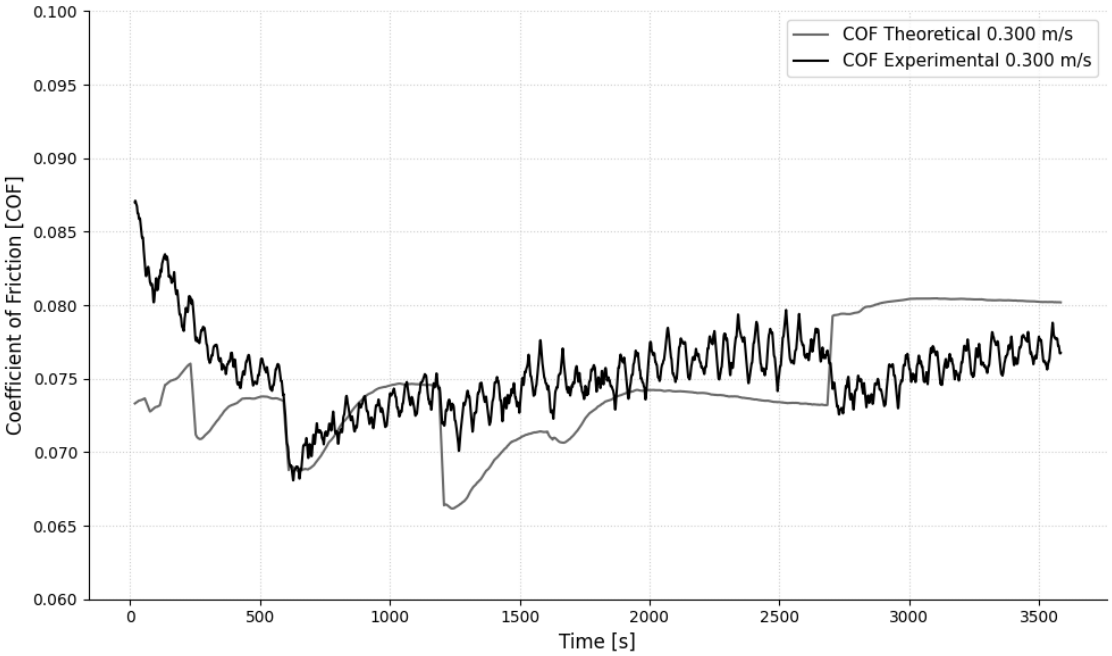


Figure 4.13: Evaluation of COF over time comparing theoretical and experimental results for the interrupted test at $V_e = 0.300$ m/s.

Figures 4.11 to 4.13 demonstrate that incorporating the summit parameters for each time leads to a higher accuracy of the developed Python model. Interestingly, the theoretical results exhibit complex behaviors, even showing increases similar to those observed in the experimental data.

While such increases are not entirely straightforward to explain from a practical standpoint, they may be attributed to temperature and load fluctuations occurring during the tests. Future work should ensure a longer lubricant preheating time to minimise these variations throughout the testing period. Consequently, because the code reads the actual temperature and load values at each time instant, this same behavior is successfully captured in the theoretical results. Regarding the overall trend of the curves over time, continuous tests exhibit a very smooth and steady friction behavior (Figures 4.8 to 4.10). Conversely, in the interrupted tests, the theoretical curves closely follow the behavior of the experimental curves, which further demonstrates the high accuracy of the developed model.

4.3 Stribeck Curve

Theoretical Stribeck curves were also obtained (Figures 4.14 to 4.16). Ideally, each test should have been repeated three times to better understand these differences. The theoretical model successfully captures the general downward trend characteristic of the transition towards full-film lubrication. It tends to predict a steeper drop in the coefficient of friction as speed increases compared to the experimental measurements. This discrepancy can be attributed to thermal effects, transient shear thinning phenomena in the lubricant, and minor local topographical variations not fully captured by the averaged statistical summit parameters.

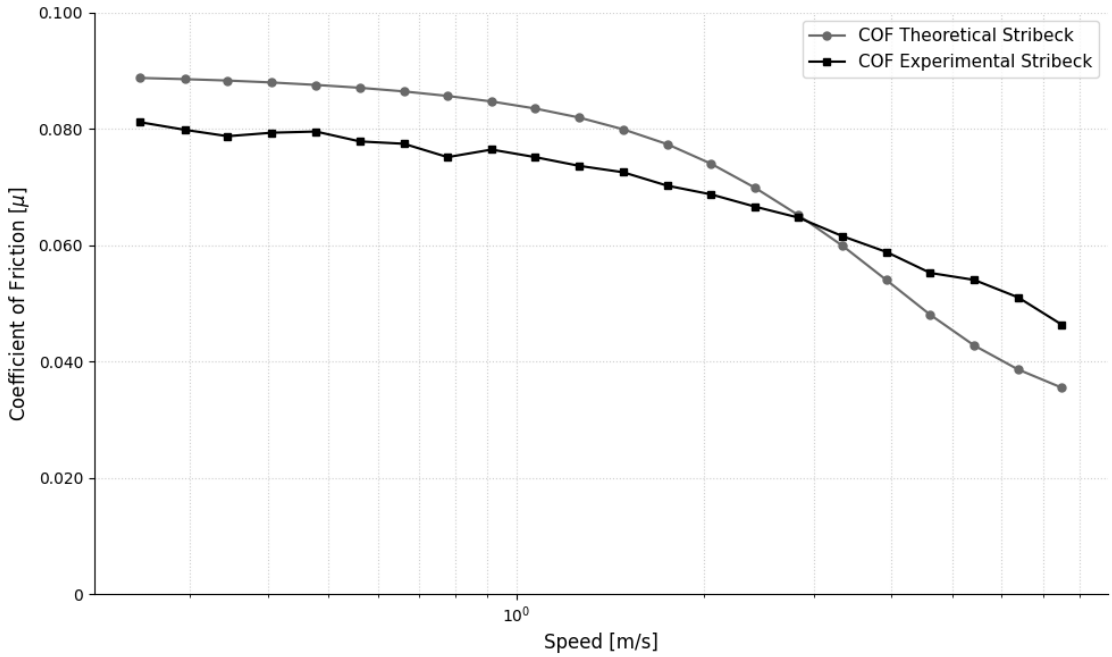


Figure 4.14: Comparison of Stribeck curves - $V_e = 0.100$ m/s.

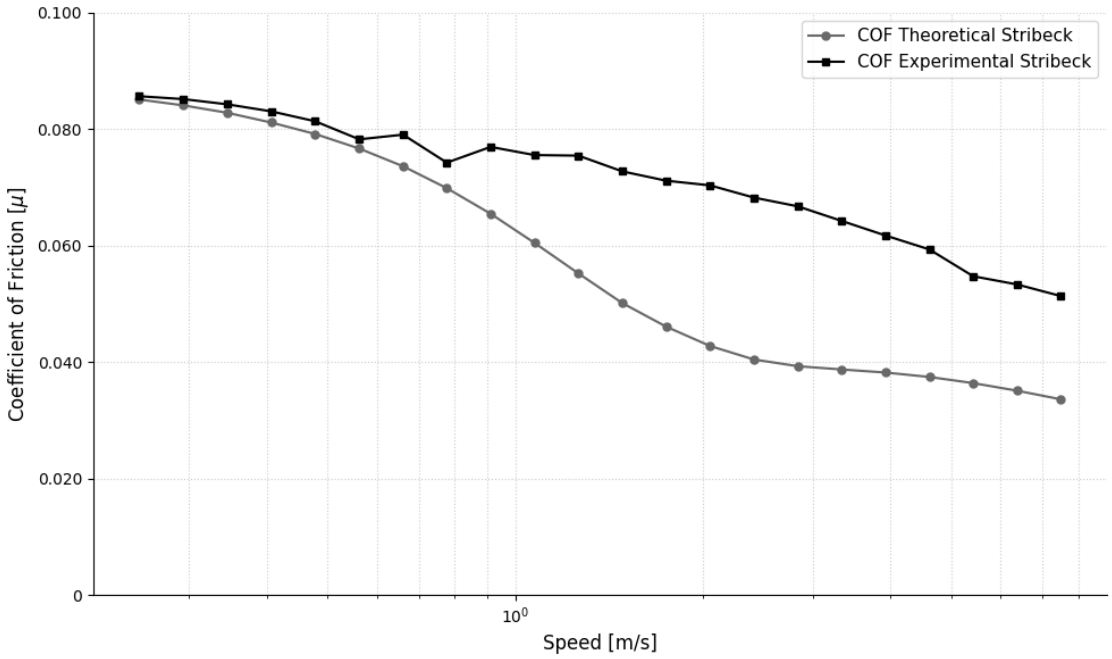


Figure 4.15: Comparison of Stribeck curves - $V_e = 0.150$ m/s.

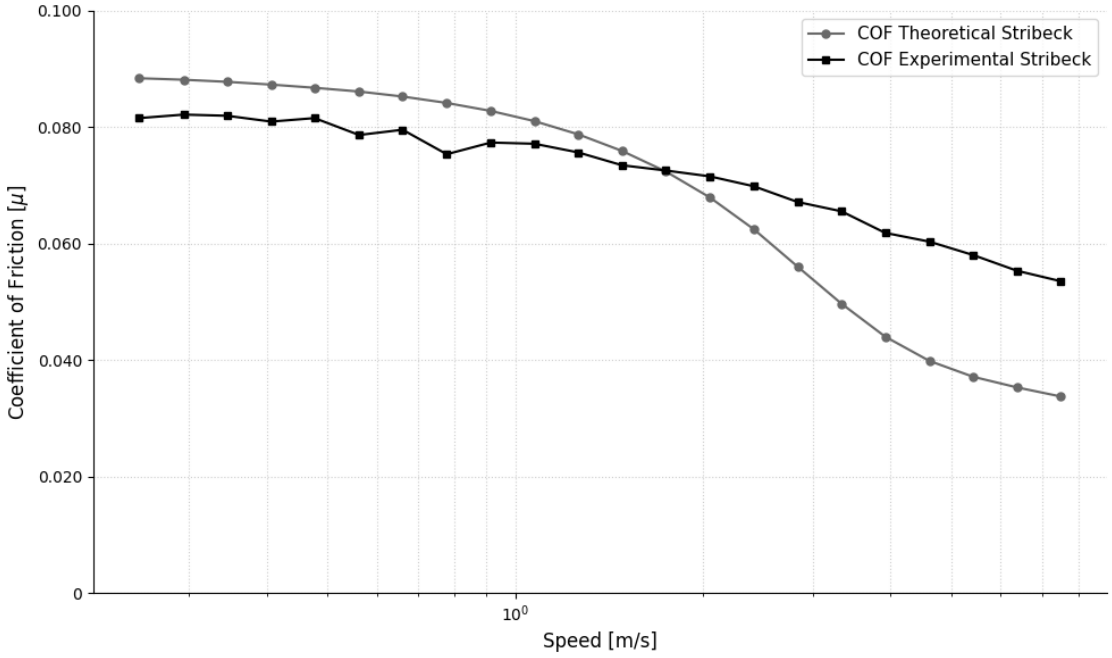


Figure 4.16: Comparison of Stribeck curves - $V_e = 0.300$ m/s.

To understand the lubrication regime that occurs for each test performed, the specific film thickness was calculated for each velocity and the results are presented in Figure 4.17. It reveals distinct operational regimes throughout all the tests. For the highest speed, the λ parameter consistently remains well above 1.5 (averaging between 1.5 and 2.0), denoting a mixed-to-EHL

transition regime where the lubricating fluid film effectively separates the interacting surfaces, minimizing direct asperity contact. Conversely, for the medium and lowest speeds, the λ values fluctuate predominantly within the 0.5 to 1.1 range, confirming a mixed lubrication regime.

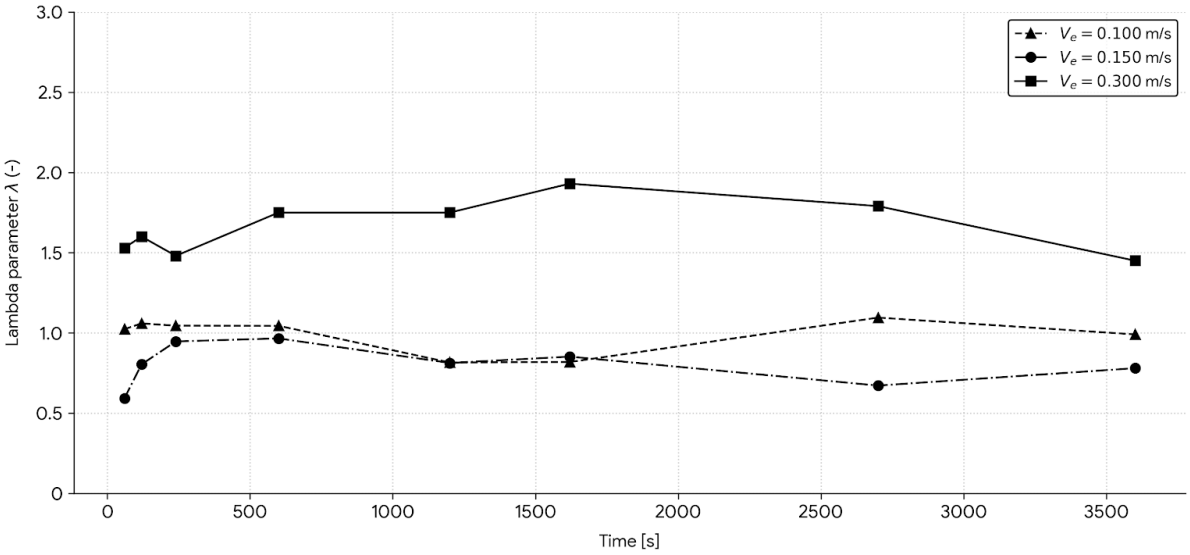


Figure 4.17: Evaluation of specific film thickness over time for all velocities.

Table 4.6: Relative differences of the specific film thickness for 0.100 m/s and 0.150 m/s relative to the 0.300 m/s reference curve.

Time [s]	**λ (Ref. 0.300 m/s)**	**Relative Difference [%]**	
		$v = 0.100$ **m/s**	$v = 0.150$ **m/s**
60	1.53	-32.9	-61.3
120	1.60	-33.9	-49.8
240	1.48	-29.2	-36.1
600	1.75	-40.4	-44.7
1200	1.75	-53.5	-53.7
1620	1.93	-57.6	-55.9
2700	1.79	-38.5	-62.5
3600	1.45	-31.7	-45.9

As detailed in Table 4.6, a direct proportionality is observed between the sliding speed and the specific film thickness, demonstrating that higher speeds systematically yield larger λ values. Furthermore, the analysis of the plasticity index presented in Table 4.5 shows that a lower plasticity index is achieved for the higher velocity, which is in full agreement with these higher λ values, confirming a reduced susceptibility to asperity deformation and a more effective hydrodynamic separation. As expected, the best results are achieved for the highest velocity.

The specific film thickness parameter was also correlated with the experimental coefficient of friction results across all tested velocities, as illustrated in Figure 4.18.

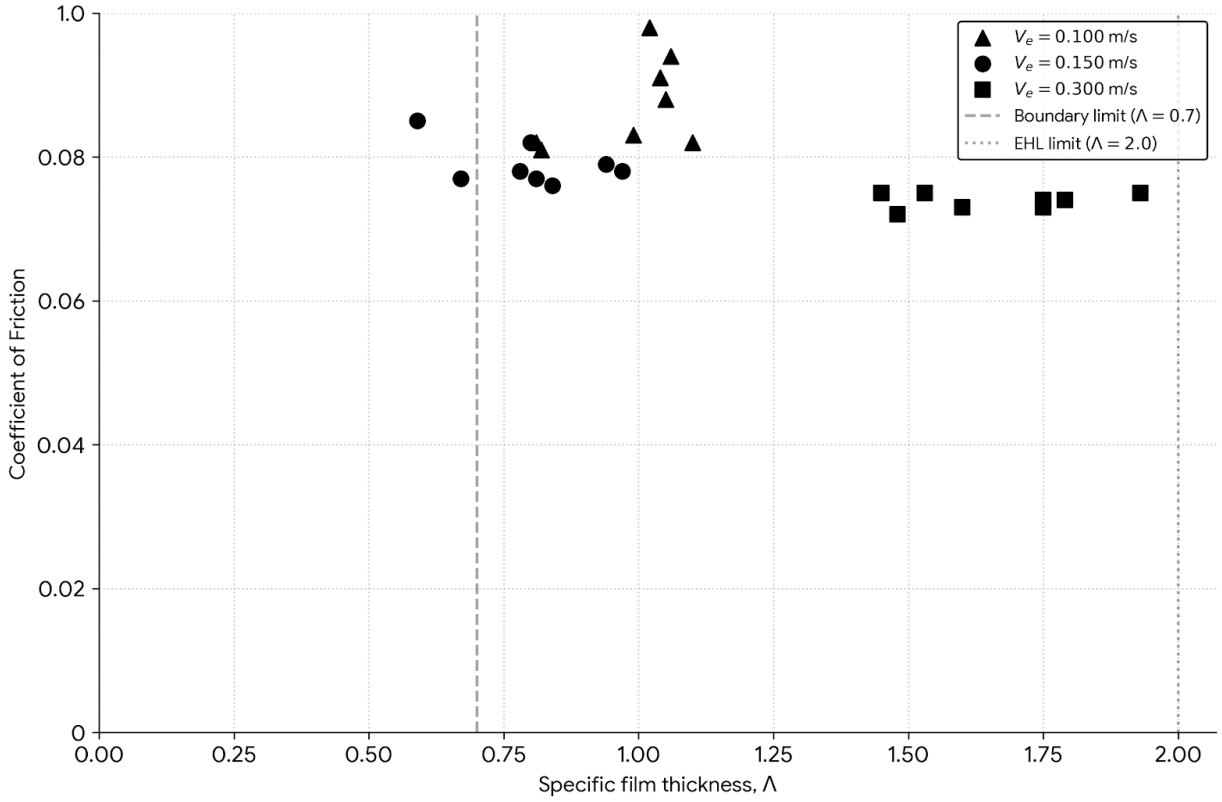


Figure 4.18: Coefficient of Friction versus specific film thickness for all velocities.

As shown in Figure 4.18, a clear relationship is observed between the specific film thickness and the experimental COF. The lower velocities (0.100 and 0.150 m/s) concentrate at lower λ values (below 1.1), remaining firmly within the mixed lubrication regime, where friction is higher due to direct asperity contact. In contrast, the highest velocity (0.300 m/s) shifts to the right (with λ ranging between 1.4 and 1.6), approaching the transition towards the EHL regime, which visibly reduces the friction coefficient. The plot demonstrates that as the entraining speed and the λ parameter increase, friction decreases consistently.

Chapter 5

Conclusions and Future Work

This chapter aims to summarise all the results obtained in this dissertation, as well as to provide a critical evaluation of the work carried out and potential directions for future research.

5.1 Conclusion

This dissertation provided a comprehensive investigation into the role of surface finishing and the transient running-in phase on the tribological performance of mechanical contacts.

Through a combination of experimental testing using an EHD2 ball-on-disc tribometer and numerical simulations, several key conclusions were established. It was concluded that precise procedural adjustments are vital, such as incorporating an extended lubricant preheating phase prior to testing to completely eliminate even minor thermal fluctuations, in order to maintain the temperature strictly at 70°C as stipulated in the study. Furthermore, data acquisition protocols during interrupted tests must account for hardware limitations, specifically programming an extra second per interval to ensure complete data recording.

The comparative evaluation between continuous and interrupted tests yielded valuable methodological conclusions. Continuous tests demonstrated a smooth, predictable friction evolution coupled with a more uniform and aggressive smoothing of the surface asperities. In contrast, interrupted tests revealed localized mechanical and thermal fluctuations at each resumption point, highlighting the sensitivity of the contact interface to repositioning variances and thermal dissipation cycles during stops. Despite these experimental challenges, both methodologies consistently pointed to the same underlying wear mechanisms, where the initial prominent peaks of the surface height distribution were preferentially flattened during the early stages of sliding.

The experimental findings confirmed that increasing the sliding speed effectively lowers the global coefficient of friction. This phenomenon is primarily governed by the enhancement of the

lubricant film thickness, which improves the separation of the interacting surfaces and progressively shields the asperities from severe plastic deformation. Specifically, while the lowest velocity ($V_e = 0.100$ m/s) operated predominantly within a mixed lubrication regime characterised by significant asperity interaction and higher initial friction, the highest velocity ($V_e = 0.300$ m/s) promoted superior surface protection.

Regarding the analysis of the Stribeck curves, both experimental and theoretical evaluations demonstrated a continuous decrease in the coefficient of friction with increasing entrainment speed, successfully mapping the transition trends toward elastohydrodynamic lubrication. The construction of Stribeck curves confirmed that the operating conditions reside predominantly within the mixed lubrication regime, where direct asperity interactions and boundary shear dictate the frictional response.

Optical profilometry analyses revealed that surface micro-geometry dynamically adapts during the initial contact cycles. The running-in process predominantly acts by smoothing out extreme asperity peaks while maintaining the macroscopic geometry of the components.

Regarding the topographical characterization, the matrix-size sensitivity study demonstrated that a 3×3 configuration yielded the most reliable summit parameters and friction predictions for the analyzed surfaces. Although previous studies achieved optimal results with a 7×7 matrix, this variation reinforces that the appropriate matrix size must be carefully evaluated and adapted depending on the specific surface finish and topographical features under investigation.

By implementing statistical summit parameters (σ_s, β, n) into the computational Python model, it was possible to capture the transient evolution of the friction coefficient with high fidelity. The theoretical results successfully mirrored experimental trends, demonstrating the robustness and accuracy of the stochastic contact model in predicting friction and surface adaptation. Characterizing the surface statistically through summit parameters at each time interval allows for a deeper and more detailed understanding of surface evolution over time. Nevertheless, it must be emphasized that equalizing this process across all stop intervals remains challenging. Therefore, great care must be taken to homogenize the topographical capture procedure and the specific analyzed area.

In conclusion, this dissertation provided a deeper insight into the characteristics of tribological components, such as surface topography and running-in phenomena. Above all, it enabled the acquisition of valuable practical knowledge and proficiency in operating two key machines essential for advanced tribological research.

5.2 Further Work

To improve the accuracy, reliability, and consistency of the results, the following recommendations are proposed for future work:

- **Test Replication:** Repeat each simulation test at least three times for every sliding velocity to ensure statistical significance and minimize experimental scatter.

- **Data Acquisition Correction:** Account for the data-logging limitation of the EHD2 machine, which omits the final second of each programmed time interval,ensuring proper synchronization and complete data collection during interrupted tests.
- **Positioning Precision:** Ensure consistent alignment by positioning the ball and disc at the exact same surface location for each test stop, thereby achieving higher measurement precision and reducing topographical variability.
- **Thermal Control and Preheating Optimization:** Implement a prolonged and strictly controlled lubricant preheating phase prior to testing to completely eliminate even minor thermal fluctuations, ensuring that the temperature remains perfectly constant at 70°C throughout the entire testing period.
- **Area Selection Consistency:** Be more precise regarding the selected area of the .ASC files when extracting summit parameters, ensuring consistency across all test stops.
- **Study Influence of Other Parameters:** Investigate different initial surface roughness values under the same sliding speed, and additionally vary the applied load and the slide-to-roll ratio.
- **Test in Gears:** Extend the application of this stochastic methodology to actual gear tooth contacts, validating the model's predictive capability under real industrial operating conditions and complex load-sharing dynamics.

Appendix A

Elliptical Contact

This appendix presents the mathematical framework and fundamental equations implemented in the numerical model to simulate elliptical contacts under lubricated conditions. The formulation is structured sequentially, beginning with Hertzian contact mechanics, advancing through elasto-hydrodynamic lubrication film thickness formulations, and concluding with the mixed lubrication and thermal models [16].

A.1 Hertzian Contact

Within any concentrated contact problem, establishing the initial elastic deformation and pressure distribution requires defining key Hertzian parameters. These include the reduced radius of curvature (R), the equivalent elastic modulus (E'), the maximum Hertzian contact pressure (p_h), the semi-axes of the resulting elliptical contact area (a and b), and the nominal contact area (A_c).

To compute these quantities, the effective radii of curvature in the entrainment (x) and transverse (y) directions are first evaluated using Equations A.1 and A.2, followed by the combined equivalent radius of curvature via Equation A.3:

$$R_x = \left(\frac{1}{R_{x1}} + \frac{1}{R_{x2}} \right)^{-1} \tag{A.1}$$

$$R_y = \left(\frac{1}{R_{y1}} + \frac{1}{R_{y2}} \right)^{-1} \tag{A.2}$$

$$R = \left(\frac{1}{R_x} + \frac{1}{R_y} \right)^{-1} \tag{A.3}$$

The elastic compliance of the interacting bodies is subsequently characterized by the equivalent elastic modulus (E'), formulated from the individual Young's moduli (E_i) and Poisson's ratios (ν_i) as shown in Equation A.4:

$$E' = \left[\frac{1}{2} \left(\frac{1-\nu_1^2}{E_1} + \frac{1-\nu_2^2}{E_2} \right) \right]^{-1} \tag{A.4}$$

Subject to a normal applied load (F_n), the contact geometry deforms into an elliptical footprint. The semi-major axis (a), semi-minor axis (b), nominal contact area (A_c), and maximum Hertzian pressure (p_h) are determined by Equations A.5 through A.8:

$$a = C_\alpha \left(\frac{2F_n R}{E'} \right)^{\frac{1}{3}} \tag{A.5}$$

$$b = C_\beta \left(\frac{2F_n R}{E'} \right)^{\frac{1}{3}} \tag{A.6}$$

$$A_c = \pi ab \tag{A.7}$$

$$p_h = \frac{3}{2} \frac{F_n}{\pi ab} \tag{A.8}$$

The dimensionless coefficients C_α and C_β, which govern the dimensions of the contact ellipse, depend on the ellipticity parameter (κ) and the complete elliptic integral of the second kind ($E(m)$). They are expressed through Equations A.9 and A.10:

$$C_\alpha = \kappa^{\frac{1}{3}} \left[\frac{2}{\pi} E(m) \right]^{\frac{1}{3}} \tag{A.9}$$

$$C_\beta = \kappa^{-\frac{2}{3}} \left[\frac{2}{\pi} E(m) \right]^{\frac{1}{3}} \tag{A.10}$$

To compute these coefficients, the auxiliary integral $E(m)$, the ellipticity parameter (κ), the auxiliary modulus (m), and the radius ratio (λ) are evaluated using Equations A.11 through A.14:

$$E(m) = \frac{\pi}{2}(1-m) \left[1 + \frac{2m}{\pi(1-m)} - \frac{1}{8} \ln(1-m) \right] \tag{A.11}$$

$$\kappa = \left[1 + \sqrt{\frac{\ln(16/\lambda)}{2\lambda}} - \sqrt{\ln(4)} + 0.16 \ln(\lambda) \right]^{-1} \tag{A.12}$$

$$m = 1 - \kappa^2 \tag{A.13}$$

$$\lambda = \frac{R_x}{R_y} \tag{A.14}$$

Where R_{xi} and R_{yi} represent the contact radii in the x and y directions, respectively, ν_i denotes the Poisson's ratio, E_i is the Young's modulus (all referring to body i), and b corresponds to the gear/disc width.

A.2 Elastohydrodynamic Lubrication

Following an approach analogous to line contact theory, the lubricant film thickness is evaluated using the dimensionless parameters proposed by Dowson and Higginson (Equations A.15 through A.18) and Moes (Equations A.19 through A.21):

$$G = \alpha E' \tag{A.15}$$

$$\bar{h} = \frac{h_c}{R_x} \tag{A.16}$$

$$U_\Sigma = \frac{\eta_0 (U_1 + U_2)}{E' R_x} \tag{A.17}$$

$$W = \frac{F_n}{E' R_x^2} \tag{A.18}$$

$$H = \bar{h} U_\Sigma^{-\frac{1}{2}} \tag{A.19}$$

$$M = W U_\Sigma^{-\frac{3}{4}} \tag{A.20}$$

$$L = G U_\Sigma^{-\frac{1}{4}} \tag{A.21}$$

To capture the elastohydrodynamic performance comprehensively across all lubrication regimes, Moes' universal dimensionless central film thickness (H_c) formulation is applied. This approach combines the individual asymptotic solutions for the rigid-isoviscous, elastic-isoviscous, rigid-piezoviscous, and elastic-piezoviscous regimes into a unified expression, defined by Equation A.22:

$$H_c = \left\{ \left[H_{RI}^{\frac{2}{3}} + \left(H_{EI}^{-4} + H_{00}^{-4} \right)^{-\frac{3}{8}} \right]^{\frac{2s}{3}} + \left(H_{RP}^{-8} + H_{EP}^{-8} \right)^{-\frac{s}{8}} \right\}^{\frac{1}{s}} \tag{A.22}$$

Where the ellipticity-dependent constant H_{00} and the weighting exponent s are determined via Equations A.23 and A.24, while the specific asymptotic film thickness components (H_{RI}, H_{EI}, H_{RP}, and H_{EP}) are given by Equations A.25 through A.28. The auxiliary parameter ϑ is defined in Equation A.29:

$$H_{00} = 1.8 \vartheta^{-1} \tag{A.23}$$

$$s = 1.5 \left[1 + \exp\left(-1.2 \frac{H_{EI}}{H_{RI}} \right) \right] \tag{A.24}$$

$$H_{RI} = 145\left(1+0.796\vartheta^{\frac{14}{15}}\right)^{-\frac{15}{7}}\vartheta^{-1}M^{-2} \tag{A.25}$$

$$H_{EI} = 3.18\left(1+0.006\ln\vartheta+0.63\vartheta^{\frac{4}{7}}\right)^{-\frac{25}{14}}\vartheta^{-\frac{1}{15}}M^{-\frac{2}{5}} \tag{A.26}$$

$$H_{RP} = 1.29\left(1+0.691\vartheta\right)^{-\frac{2}{3}}L^{\frac{2}{3}} \tag{A.27}$$

$$H_{EP} = 1.48\left(1+0.006\ln\vartheta+0.63\vartheta^{\frac{4}{7}}\right)^{-\frac{7}{20}}\vartheta^{-\frac{1}{24}}M^{-\frac{1}{12}}L^{\frac{3}{4}} \tag{A.28}$$

$$\vartheta = \frac{R_x}{R_y} \tag{A.29}$$

Where ϑ represents the ellipticity parameter, defined as the ratio of the effective radii of curvature in the rolling/sliding (x) and transverse (y) directions.

A.3 Mixed Lubrication Model

The modified dimensionless central film thickness (H_c) under mixed lubrication conditions is expressed by Equation A.30:

$$H_c = \gamma_1^{\frac{1}{2}}\left\{\left[\gamma_1^{\frac{9}{4}}H_{RI}^{\frac{2}{3}}+\left(\gamma_1^{-\frac{2}{5}}H_{EI}^{-4}+H_{00}^{-4}\right)^{-\frac{3}{8}}\right]^{\frac{2s}{3}}+\left[\gamma_1^{4}\left(H_{RP}^{-8}+H_{EP}^{-8}\right)\right]^{-\frac{s}{8}}\right\}^{\frac{1}{s}} \tag{A.30}$$

Since the mathematical formulations regarding the asperity contact mechanics (Greenwood and Williamson model) and lubricant rheological properties follow standard literature implementations, their detailed derivations are omitted from this appendix.

A.4 Thermal Model

Once the film thickness distribution is established, the numerical procedure mirrors that of linear contacts, with the exception of thermal feedback loops. While the influence of viscous heating and thermal shear reduction is governed by the thermal reduction factor ϕ_T, the flash temperature calculations are evaluated using Equations A.31 through A.37:

$$\dot{Q} = \mu F_n v_g \tag{A.31}$$

$$R_{cf} = \frac{h_c}{2kA_H} \tag{A.32}$$

$$R_{fi} = \frac{1.06}{A_H k_s}\sqrt{\frac{\chi_i a}{U_i}} \tag{A.33}$$

$$\varepsilon = \frac{R_{f2} + R_{cf}}{R_{f1} + R_{f2} + 2R_{cf}} \tag{A.34}$$

$$\Delta\bar{T}_{Fl} = R_{f1}\varepsilon\dot{q} \tag{A.35}$$

$$\Delta\bar{T}_{oil} = \frac{v_g \bar{\tau} h_c}{8k} \tag{A.36}$$

$$\Delta\bar{T}_f = T_0 + \Delta\bar{T}_{Fl} + \Delta\bar{T}_{oil} \tag{A.37}$$

Where R_{fi} represents the transient thermal resistance of body i, ε is the thermal partition factor, $\Delta\bar{T}_{Fl}$ accounts for the frictional flash temperature rise, $\Delta\bar{T}_{oil}$ denotes the localized lubricant temperature increase, and $\Delta\bar{T}_f$ evaluates the final operational contact temperature by incorporating the initial lubricant supply temperature T_0.

Appendix B

Techniques for measuring surface topography

Table B.1: Bandwidth limitations of various techniques for measuring surface topography.

Technique	**Approx. max. analysis size**	**Approx. lateral resolution limit**	**Frequency range (m^{-1})**	**Advantages**	**Limitations**
Stylus profilometry	50 mm (200 mm with stitching)	1 μm	10^2 (10^1)–10^7	Sub-nanometer height resolution. Unaffected by sample's optical properties	Contact method, can cause damage. Measurement is time-intensive. Tip shape can introduce artifacts
Optical profilometry (WLI, Confocal Microscopy and Chromatic, and Structural Light Projection)	5 mm (100 mm with stitching)	1 μm	10^3 (10^2)–10^7	Rapid, non-contact. Sub-nanometer height resolution	Diffraction-limited spatial information. Difficult to use on very rough surfaces. Artifacts from transparent thin films
Light and x-ray scattering	5 mm	10 nm	10^3–10^9	Rapid, non-contact. Insensitive to vibration	Relies on models and assumptions to relate scattered beam to surface spectrum. Does not recover real-space topography
Scanning probe microscopy	100 μm	1 Å	10^5–10^{11}	High-resolution	Small areas. Sensitive to vibration. Tip shape can introduce artifacts

Appendix C

Summary of Tests Performed

C.1 Total Sliding Distance

The total sliding distance (d) achieved during each test is determined by the linear velocity and the duration of the test:

$$d = v \times t_{\text{test}}$$

where:

- v represents the sliding velocity (m/s).
- t_{test} represents the test duration in seconds (1 hour = 3600 seconds).

C.2 Number of Cycles

The total number of contact cycles (N) completed along a circular wear track of radius R is calculated by dividing the total sliding distance by the circumference of the track:

$$N = \frac{d}{2\pi R}$$

where:

- d is the total sliding distance (m).
- R is the track radius (m).

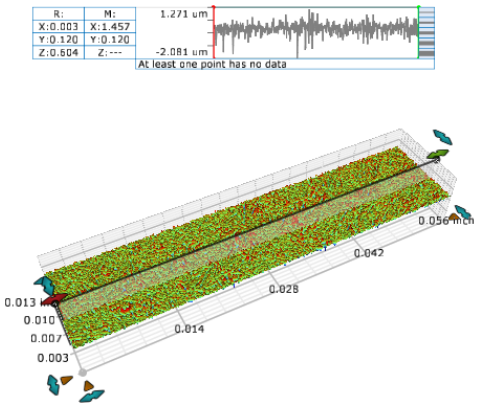
Table C.1: Summary of tests performed in the laboratory including roughness measurements.

Date	Test Information	Track Radius [mm]	Total Distance [m]	Cycles	Test Time [h]	Lab Time [h]
June 11, 2026	$v = 0.100$ m/s, $T = 70°$C, $F = 50$ N, SRR $= 50\%$ PAO 150	37.250	360	1538	1	3
June 11, 2026	$v = 0.150$ m/s, $T = 70°$C, $F = 50$ N, SRR $= 50\%$ PAO 150	37.000	540	2323	1	4
June 15, 2026	$v = 0.300$ m/s, $T = 70°$C, $F = 50$ N, SRR $= 50\%$ PAO 150	36.750	1080	4677	1	8
July 22, 2026	$v = 0.100$ m/s, $T = 70°$C, $F = 50$ N, SRR $= 50\%$ PAO 150	36.250	360	1581	1	12.5
July 29, 2026	$v = 0.150$ m/s, $T = 70°$C, $F = 50$ N, SRR $= 50\%$ PAO 150	36.000	540	2387	1	9
August 5, 2026	$v = 0.300$ m/s, $T = 70°$C, $F = 50$ N, SRR $= 50\%$ PAO 150	35.750	1080	4808	1	14
August 13, 2026	$v = 0.100$ m/s, $T = 70°$C, $F = 50$ N, SRR $= 50\%$ PAO 150	35.500	360	1614	1	8
August 17, 2026	$v = 0.100$ to 3.000 m/s, $T = 70°$C, $F = 50$ N, SRR $= 50\%$ PAO 150	36.250	–	–	1	1
August 17, 2026	$v = 0.100$ to 3.000 m/s, $T = 70°$C, $F = 50$ N, SRR $= 50\%$ PAO 150	36.000	–	–	1	1
August 17, 2026	$v = 0.100$ to 3.000 m/s, $T = 70°$C, $F = 50$ N, SRR $= 50\%$ PAO 150	35.750	–	–	1	1

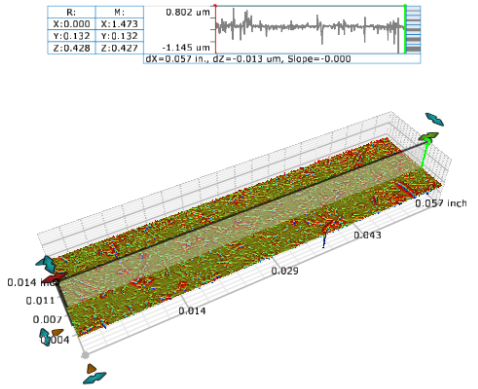
Appendix D

3D Surface Topography and Roughness Profiles

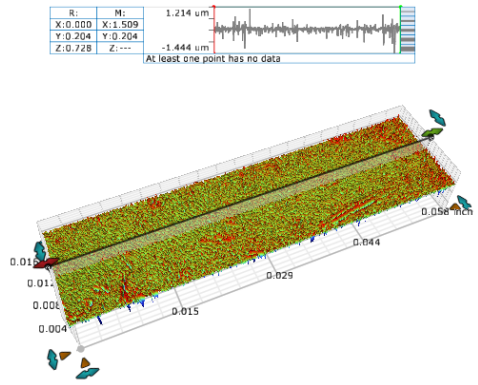
D.1 Surface Topography at $V_e = 0.100$ m/s



(a) 3D surface topography and roughness profile obtained via optical profilometry before the continuous test (70°C, 50 N, SRR = 50%, $V_e = 0.100$ m/s).



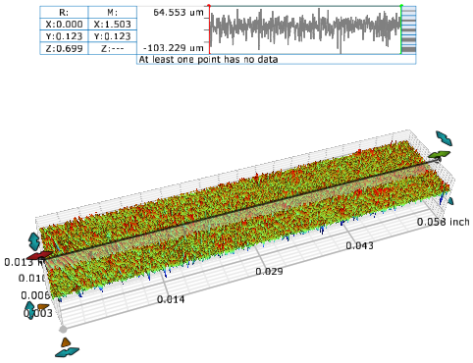
(b) 3D surface topography and roughness profile obtained via optical profilometry after the continuous test (70°C, 50 N, SRR = 50%, $V_e = 0.100$ m/s).



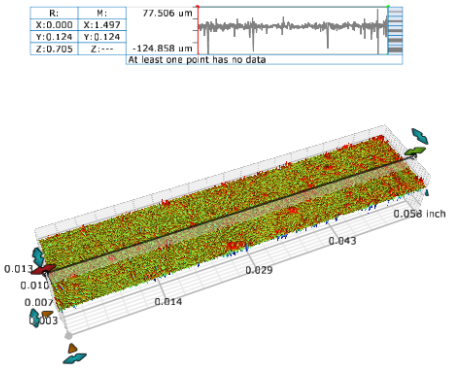
(c) 3D surface topography and roughness profile obtained via optical profilometry after the interrupted test (70°C, 50 N, SRR = 50%, $V_e = 0.100$ m/s).

Figure D.1: 3D surface topography and roughness profile obtained via optical profilometry for 0.100 m/s.

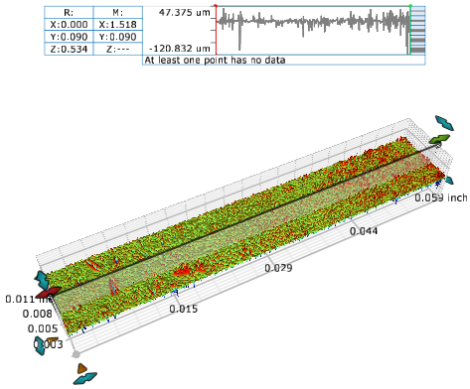
D.2 Surface Topography at $V_e = 0.150$ m/s



(a) 3D surface topography and roughness profile obtained via optical profilometry before the continuous test (70°C, 50 N, SRR = 50%, $V_e = 0.150$ m/s).



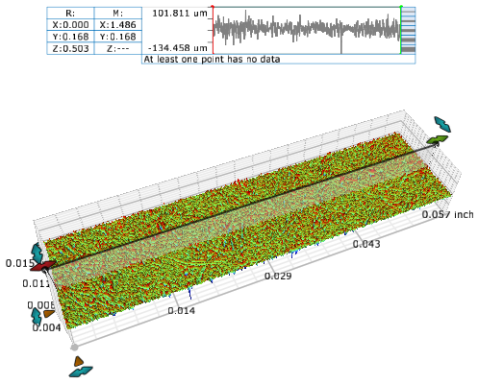
(b) 3D surface topography and roughness profile obtained via optical profilometry after the continuous test (70°C, 50 N, SRR = 50%, $V_e = 0.150$ m/s).



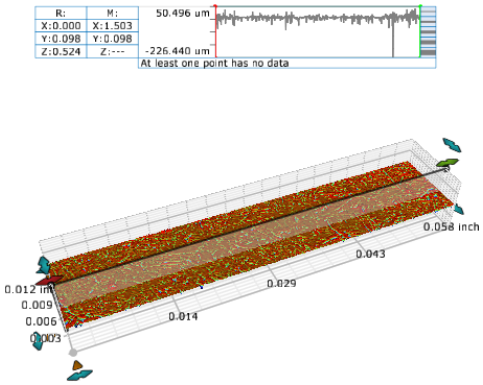
(c) 3D surface topography and roughness profile obtained via optical profilometry after the interrupted test (70°C, 50 N, SRR = 50%, $V_e = 0.150$ m/s).

Figure D.2: 3D surface topography and roughness profile obtained via optical profilometry for 0.150 m/s.

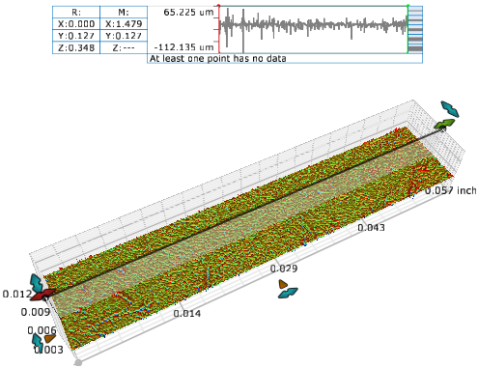
D.3 Surface Topography at $V_e = 0.300$ m/s



(a) 3D surface topography and roughness profile obtained via optical profilometry before the test (70°C, 50 N, SRR = 50%, $V_e = 0.300$ m/s).



(b) 3D surface topography and roughness profile obtained via optical profilometry after the continuous test (70°C, 50 N, SRR = 50%, $V_e = 0.300$ m/s).



(c) 3D surface topography and roughness profile obtained via optical profilometry after the interrupted test (70°C, 50 N, SRR = 50%, $V_e = 0.300$ m/s).

Figure D.3: 3D surface topography and roughness profile obtained via optical profilometry for 0.300 m/s.

Bibliography

[1] M. M. Khonsari, Sahar Ghatrehsamani, and Saleh Akbarzadeh. On the running-in nature of metallic tribo-components: A review. *Wear*, 474–475:203871, 2021.

[2] M. Sedlaček, B. Podgornik, and J. Vižintin. Influence of surface preparation on roughness parameters, friction and wear. *Wear*, 266(3):482–487, 2009. Tribology of Engineered Surfaces.

[3] Andrzej Dzierwa. Influence of surface preparation on surface topography and tribological behaviours. *Archives of Civil and Mechanical Engineering*, 17(3):502–510, 2017.

[4] Xin Li, Wen Shao, Jinyuan Tang, Ding Zhang, Jiling Chen, Jiuyue Zhao, and Yuqin Wen. Multi-physics field coupling interface lubrication contact analysis for gear transmission under various finishing processes. *Engineering Failure Analysis*, 165:108742, 2024.

[5] D. Mallipeddi, M. Norell, M. Sosa, and L. Nyborg. The effect of manufacturing method and running-in load on the surface integrity of efficiency tested ground, honed and superfinished gears. *Tribology International*, 131:277–287, 2019.

[6] Xinmin Li, Mario Sosa, Martin Andersson, and Ulf Olofsson. A study of the efficiency of spur gears made of powder metallurgy materials – ground versus super-finished surfaces. *Tribology International*, 95:211–220, 2016.

[7] Minghui Tu, Rikard Hjelm, Lucas Bard, Ellen Bergseth, Linus Everlid, and Ignacio Victoria Rodríguez. Efficiency and pitting resistance of mechanochemically finished gears. *Results in Engineering*, 28:107286, 2025.

[8] X. Tian, Y. Sun, W. Mu, et al. High-speed and low-noise gear finishing by gear grinding and honing: A review. *Chinese Journal of Mechanical Engineering*, 37(1):127, 2024.

[9] Anna Francès-Abellán, Juan Luis Fernández-Marchena, and Andreu Ollé. Cleaning your tools doesn't mean that the tools are clean. a qualitative and quantitative perspective using confocal microscopy. *Journal of Archaeological Science: Reports*, 64:105121, 2025.

[10] Tevis D. B. Jacobs, Till Junge, and Lars Pastewka. Quantitative characterization of surface topography using spectral analysis. *Surface Topography: Metrology and Properties*, 5(1):013001, 2017.

[11] M. Andersson, M. Sosa, and U. Olofsson. The effect of running-in on the efficiency of superfinished gears. *Tribology International*, 93:71–77, 2016.

[12] Xin Pei, Wei Pu, Ying Zhang, and Lu Huang. Surface topography and friction coefficient evolution during sliding wear in a mixed lubricated rolling-sliding contact. *Tribology International*, 137:303–312, 2019.

[13] Qi Wen, Mingming Liu, Zenglei Zhang, and Yunyun Sun. Experimental investigation into the friction coefficient of ball-on-disc in dry sliding contact considering the effects of surface roughness, low rotation speed, and light normal load. *Lubricants*, 10(10):256, 2022. License: CC BY 4.0.

[14] S. Akbarzadeh and M.M. Khonsari. On the optimization of running-in operating conditions in applications involving ehl line contact. *Wear*, 303(1):130–137, 2013.

[15] E.S. Gadelmawla, M.M. Koura, T.M.A. Maksoud, I.M. Elewa, and H.H. Soliman. Roughness parameters. *Journal of Materials Processing Technology*, 123(1):133–145, 2002.

[16] Miguel Dias. Modelling the gear coefficient of friction: Effects of surface finishing and running-in. Master's dissertation, Faculty of Engineering, University of Porto, Porto, Portugal, 2025.

[17] Richard Leach and Han Haitjema. Bandwidth characteristics and comparisons of surface texture measuring instruments. *Measurement Science and Technology*, 21(3):032001, 2010.

[18] ISO. Iso 3274:1996 - geometrical product specifications (gps) — surface texture: Profile method — nominal characteristics of contact (stylus) instruments. Standard 3274:1996, International Organization for Standardization, Geneva, Switzerland, 12 1996.

[19] Gaoliang Dai, Xiukun Hu, and Johannes Degenhardt. Bottom-up approach for traceable calibration of tip geometry of stylus profilometer. *Surface Topography: Metrology and Properties*, 10(1):015018, 2022.

[20] Wee Keat Chong, Xiang Li, and Yeng Chai Soh. Spectral effects of dual wavelength low coherence light source in white light interferometry. *Optics and Lasers in Engineering*, 51(6):651–655, 2013.

[21] Xuanzong Wu, Linlin Zhu, Fengzhou Fang, and Xiaodong Zhang. Research on the quality control technology of micro-topography machining based on in situ white light interferometry. *Measurement*, 220:113257, 2023.

[22] Hang Zhao, Yijun Xie, Renlong Zhu, Zhengqiong Dong, Xuanze Wang, Shiyuan Liu, and Jinlong Zhu. Robust vertical scanning interferometry at a long coherence length. *Optics and Lasers in Engineering*, 186:108769, 2025.

[23] Alberto Mínguez-Martínez, Piera Maresca, Jesús Caja, and Jesús de Vicente y Oliva. Results of a surface roughness comparison between stylus instruments and confocal microscopes. *Materials*, 15(16), 2022.

[24] D. A. Lange, H. M. Jennings, and S. P. Shah. Analysis of surface roughness using confocal microscopy. *Journal of Materials Science*, 28(14):3879–3884, 1993. Published: 01 January 1993.

[25] MARPOSS S.p.A., Italy. *Chromatic Confocal Reference Guide*, edition 07/2023 edition, 07 2023. Document code: ODN6S01EN00.

[26] Natalia Lishchenko, Garret E. O'Donnell, and Mark Culleton. Contactless method for measurement of surface roughness based on a chromatic confocal sensor. *Machines*, 11(8), 2023.

[27] Imre Forgács and Ákos Antal. Comparison of structured light projection-based surface reconstruction methods. *Periodica Polytechnica Mechanical Engineering*, 69(2):151–163, 2025.

[28] Timothy L. Krantz. On the correlation of specific film thickness and gear pitting life. AGMA Technical Paper 14FTM21, American Gear Manufacturers Association (AGMA), October 2014. NASA Technical Reports Server (NTRS).

[29] Ning Yu and Andreas A. Polycarpou. Extracting summit roughness parameters from random gaussian surfaces accounting for asymmetry of the summit heights. *Journal of Tribology*, 126(4):761–766, 11 2004.

[30] Marcia M Maru. Bridging surface metrology and function in orthopedic biomaterials: from quantitative standards to predictive design. *Surface Topography: Metrology and Properties*, 14(2):023001, apr 2026.

[31] Andrej Razumić, Zvonko Trzun, and Zdenka Keran. 3d roughness parameters in metal surface characterization. *Journal Metalurgija*, 65(1), 2026.

[32] I. G. Goryacheva and A. A. Yakovenko. The asperities density and height distribution combined effect on rough elastic bodies contact characteristics. *Lobachevskii Journal of Mathematics*, 45:2279–2292, August 2024.

[33] Q. Jane Wang and Yip-Wah Chung, editors. *Encyclopedia of Tribology*. Springer US, New York, NY, 2013.

[34] M.M. Khonsari, Sahar Ghatrehsamani, and Saleh Akbarzadeh. On the running-in nature of metallic tribo-components: A review. *Wear*, 474-475:203871, 2021.

[35] Qian Wang, Biao Ma, Liang Yu, Man Chen, Guoyu Wang, and Liangjie Zheng. Influence of applied pressure on the tribological behaviors of a wet multi-disc clutch during the running-in process. *Industrial Lubrication and Tribology*, 75(6):637–644, 07 2023.

[36] A. Clarke, I.J.J. Weeks, R.W. Snidle, and H.P. Evans. Running-in and micropitting behaviour of steel surfaces under mixed lubrication conditions. *Tribology International*, 101:59–68, 2016.

[37] Saleh Akbarzadeh and M.M. Khonsari. Experimental and theoretical investigation of running-in. *Tribology International*, 44(2):92–100, 2011.

[38] D. Mallipeddi, M. Norell, M. Sosa, and L. Nyborg. Influence of running-in on surface characteristics of efficiency tested ground gears. *Tribology International*, 115:45–58, 2017.

[39] T Lohner, J Mayer, K Michaelis, B-R Höhn, and K Stahl. On the running-in behavior of lubricated line contacts. *Proceedings of the Institution of Mechanical Engineers, Part J: Journal of Engineering Tribology*, 231(4):441–452, 2017.

[40] Xiaobin Lu, M. M. Khonsari, and E. R. M. Gelinck. The stribeck curve: Experimental results and theoretical prediction. *Journal of Tribology*, 128(4):789–794, 2006.

[41] Haijie Yu and Haijun Wei. The study of the vibration under different lubrication states based on stribeck curve. *Noise & Vibration Worldwide*, 53(6):322–329, 2022.

[42] R. I. Popovici and D. J. Schipper. Stribeck and traction curves for elliptical contacts: Isothermal friction model. *International Journal of Sustainable Construction & Design*, 4(2), 2014.

[43] Scott Bair. Chapter one - an introduction to elastohydrodynamic lubrication. In *High Pressure Rheology for Quantitative Elastohydrodynamics (Second Edition)*, pages 1–19. Elsevier, second edition edition, 2019.

[44] Miguel Damião. Modelling the tribo-dynamic behaviour of a gear test rig. Master's dissertation, Faculty of Engineering, University of Porto, Porto, Portugal, 2026.

[45] P. M. Lugt and G. E. Morales-Espejel. A review of elasto-hydrodynamic lubrication theory. *Tribology Transactions*, 54(3):470–496, 2011.

[46] Carlos M. C. G. Fernandes. Tribologia — Órgãos de máquinas (ano letivo 2023/2024). Course notes / technical report, Faculty of Engineering, University of Porto, Department of Mechanical Engineering, Porto, Portugal, 2024. Teaching material for the Bachelor in Mechanical Engineering; Online; accessed 2-Jun-2026.

[47] Dong Zhu, Jiaxu Wang, and Qian Wang. On the stribeck curves for lubricated counterformal contacts of rough surfaces. *Journal of Tribology*, 137(2), 2015.

[48] Dinesh Mallipeddi, Mats Norell, Mario Sosa, and Lars Nyborg. Effect of running-in (load and speed) on surface characteristics of honed gears. *Tribology Transactions*, 62(3):412–418, 2019.

[49] Axel Baumann and Bernd Bertsche. Coefficient of friction behavior of gear oils and significance for the meshing process of spur gears. *Forschung im Ingenieurwesen*, 86(4):795–805, 2022.

[50] A. Nakajima and T. Mawatari. Effects of surface topography and running-in upon rolling contact fatigue life -evaluation by plasticity index-. In D. Dowson, C.M. Taylor, T.H.C. Childs, G. Dalmaz, Y. Berthier, L. Flamand, J.-M. Georges, and A.A. Lubrecht, editors, *Tribology for Energy Conservation*, volume 34 of *Tribology Series*, pages 291–299. Elsevier, 1998.

[51] M. Ciavarella. A new plasticity index including size-effects in the contact of rough surfaces. *Lubricants*, 12(3), 2024.

[52] Xin Li, Wen Shao, Jinyuan Tang, Jiling Chen, and Jiuyue Zhao. Towards understanding the influencing mechanism of barrel finishing on tooth surface integrity and contact performance. *Wear*, 572-573:206020, 2025.

[53] Shubham Khatri, Jagjeet Singh, and Anant Kumar Singh. Design and analysis of a new magnetorheological worm gear type finishing process for improved productivity. *Journal of Materials Engineering and Performance*, 34(19):21505–21516, 2025.

[54] Mark Riggs, Nikhil Murthy, and Stephen Berkebile. Scuffing resistance and starved lubrication behavior in helicopter gear contacts: Dependence on material, surface finish, and novel lubricants. *Tribology Transactions*, 60(5):834–846, 2017.

[55] Carlos M.C.G. Fernandes, Pedro M.T. Marques, Ramiro C. Martins, and Jorge H.O. Seabra. Film thickness and traction curves of wind turbine gear oils. *Tribology International*, 86:1–9, 2015.

[56] Petro Technologies. *EHD Ultra Thin Film Measurement System — Product Documentation*. Petro Technologies, 2026. Accessed: August 23, 2026.

[57] Ellen Bergseth, Yi Zhu, and Anders Söderberg. Study of surface roughness on friction in rolling/sliding contacts: Ball-on-disc versus twin-disc. *Tribology Letters*, 68(2):69, 2020.

[58] Yasir Al-Jeboori, Shahriar Kosarieh, Ardian Morina, and Anne Neville. Investigation of pure sliding and sliding/rolling contacts in a dlc/cast iron system when lubricated in oils containing modtc-type friction modifier. *Tribology International*, 122:23–37, 2018.

[59] Yukio Tamura, Kazutaka Kobayashi, Kenichiro Aratani, Shinji Tanaka, Masao Kikuchi, Masabumi Masuko, and Naoto Ohtake. Influence of wear surface morphology and phosphorus-containing tribofilm on crack initiation of manganese phosphate coated steel under rolling–sliding contact. *Tribology Online*, 15(3):154–169, 2020.

[60] Xiong Liang, Ping Du, Shuangshou Li, and Chenhui Zhang. Tribological properties of additive manufactured ti6al4v against cemented carbide under dry sliding conditions. *Tribology International*, 167:107358, 2022.